

NEW ANALYSIS STRATEGIES FOR MICRO ASPHERIC LENS METROLOGY

by

Solomon Abebe Gugsu

A thesis submitted to the faculty of
The University of North Carolina at Charlotte
in partial fulfillment of the requirements
for the degree of Doctor of Philosophy in the
Department of Optical Science and Engineering

Charlotte

2006

Approved by:

Dr. Angela Davies

Dr. Faramarz Farahi

Dr. Michael A. Fiddy

Dr. Thomas J. Suleski

Dr. Kent Curran

ABSTRACT

SOLOMON ABEBE GUGSA. New Analysis Strategies for Micro Aspheric Lens Metrology. (Under the direction of Dr. ANGELA DAVIES)

Effective characterization of an aspheric micro lens is critical for understanding and improving processing in micro-optic manufacturing. Since most microlenses are plano-convex, where the convex geometry is a conic surface, current practice is often limited to obtaining an estimate of the lens conic constant, which average out the surface geometry that departs from an exact conic surface and any addition surface irregularities. We have developed a comprehensive approach of estimating the best fit conic and its uncertainty, and in addition propose an alternative analysis that focuses on surface errors rather than best-fit conic constant. We describe our new analysis strategy based on the two most dominant micro lens metrology methods in use today, namely, scanning white light interferometry (SWLI) and phase shifting interferometry (PSI). We estimate several parameters from the measurement. The major uncertainty contributors for SWLI are the estimates of base radius of curvature, the aperture of the lens, the sag of the lens, noise in the measurement, and the center of the lens. In the case of PSI the dominant uncertainty contributors are noise in the measurement, the radius of curvature, and the aperture. Our best-fit conic procedure uses least squares minimization to extract a best-fit conic value, which is then subjected to a Monte Carlo analysis to capture combined uncertainty. In our surface errors analysis procedure, we consider the surface errors as the difference between the measured geometry and the best-fit conic surface or as the difference between the measured geometry and the design specification for the lens. We focus on a

Zernike polynomial description of the surface error, and again a Monte Carlo analysis is used to estimate a combined uncertainty, which in this case is an uncertainty for each Zernike coefficient. Our approach also allows us to investigate the effect of individual uncertainty parameters and measurement noise on both the best-fit conic constant analysis and the surface errors analysis, and compare the individual contributions to the overall uncertainty.

ACKNOWLEDGEMENTS

I am grateful to many individuals who have contributions in various ways. First of all I would like to thank my thesis advisor Dr. Angela Davies for her inspirational guidance toward the advancement and completion of the research project. In addition I would like to thank Dr. Faramarz Farahi not only for his contribution as my co advisor and committee member but also for his unconditional assistance, and Dr. Michael A. Fiddy, Dr. Thomas J. Suleski, and Dr. Kent Curran for their thoughtful contributions.

I thank Dr. Terrill W. Mayes who provided me an opportunity to join UNCC and consistent help and encouragement during my stay at the university. Furthermore, I would like to express my gratitude towards Dr. M. Yasin Akhtar Raja, and Mr. Daniel Abebe (my brother) for their encouragement. Most important of all, I thank my wife, Kokebe Negash, and my children, Ruth, Nathnael, and Samuel for their constant smile, everlasting patience, and continuing encouragement.

Finally, I would like to thank the National Science Foundation (Grant # 0323505) for their financial support. I also would like to thank Erik Novak from Veeco Instruments and Chris Linnen from Digital Optics Corporation.

TABLE OF CONTENTS

1. INTRODUCTION	1
2. AN ASPHERIC SURFACE	8
2.1 The geometry of surfaces	8
2.1.1 Ellipsoid and ellipse	8
2.1.2 The hyperboloid of two sheets and hyperbola	9
2.1.3 Elliptic paraboloid and parabola	10
2.1.4 Tangential radius of curvature	11
2.2 A micro aspheric sag equation	12
3. APPROACHES TO MICRO ASPHERIC SURFACE PROFILE MEASUREMENTS	19
3.1 Phase Shifting Interferometry	20
3.1.1 Wave front phase detection and unwrapping	22
3.2 Scanning white light interferometry measurement	25
3.2.1 Frequency domain analysis	28
4. WAVE FRONT ABERRATION	31
4.1 Primary aberrations	32
4.2 Interferograms of primary aberrations	34
4.3 Power series expansion of wavefront aberrations	37
4.4 Zernike Polynomials	39
4.5 Relationship between Zernike Polynomials and wave front aberrations	40
5. INTERFEROMETRIC MICRO-ASPHERIC LENS MEASUREMENT SIMULATION	44
5.1 Interferometric simulation code	44
5.2 Simulation results for misalignment	47
5.3 Misalignment in experiment versus simulation	50
6. EXTRACTING THE ASPHERIC MICRO LENS SURFACE PROFILE FROM THE MEASUREMENT	53
6.1 SWLI measurement data and determination of uncertainty parameters	54
6.1.1 Estimating the conic surface parameters	56
6.2 Phase shifting interferometry measurement	60
6.2.1 Extracting surface profile from OPD map	61
6.2.2 Estimating the conic surface parameters and uncertainty	62
7. EXTRACTING BEST FIT CONIC CONSTANT	69
7.1 Chi-square minimization based on SWLI measurement	69
7.2 Chi square minimization based on PSI measurement	72
7.2.1 Radius and lens aperture distributions	73

7.2.3	OPD map due to misalignment.....	75
7.2.4	Surface profile generation and extracting the best fit conic constant	77
7.3	Monte Carlo for best-fit conic constant	80
7.4	Uncertainty parameters effect on the best-fit conic constant.....	83
8	SUBTRACTING INTENDED SHAPE.....	88
8.1	Subtracting intended shape from the surface profile measurement	89
8.2	Subtracting intended shape from the OPD measurement	91
9.	RESIDUAL ERROR ANALYSIS.....	94
9.1	Surface error analysis based on SWLI measurement	94
9.2	Surface error analysis based on PSI measurement	99
10.	CONCLUSIONS.....	103
	REFERENCES	106
	APPENDIX A: A LEAST-SQUARES MINIMIZATION AND MONTE CARLO APPROACH TO ESTIMATING THE CONIC CONSTANT AND UNCERTAINTY FOR MICROLENS MEASUREMENTS	110
	APPENDIX B: A MONTE CARLO ANALYSIS OF SURFACE ERRORS FOR ASPHERIC MICROLENS MANUFACTURING.....	119
	APPENDIX C: MISALIGNMENT SIMUATION CODE.....	129
	APPENDIX D: MONTE CARLO SIMULATION CODE	133
	APPENDIX E: PSI MEASUREMENT ANALYSIS CODE	137
	APPENDIX F: SURFACE PROFILE MEASUREMENT SIMULATION.....	149
	APPENDIX G: OPD MEASUREMENT SIMULATION	151
	APPENDIX H: ZERNIKES FROM RESIDUAL ERRORS BASED ON SWLI.....	153
	APPENDIX I: ZERNIKES FROM RESIDUAL ERRORS BASED ON PSI.....	155

1. INTRODUCTION

Micro-lenses have become important components in many technologies such as optical switches, optical data storage, and detector arrays. Basically, micro lenses are classified as refractive, diffractive and hybrid (refractive/diffractive) elements. Refractive elements have high efficiency and the performance is nearly independent of wavelength. On the other hand, diffractive elements are very versatile but can have limited diffraction efficiency and large wavelength-dependent aberrations. Refractive elements consist of continuous surface relief geometries and are designed with the laws of geometrical optics. Since refractive elements depend relatively weakly on wavelength, the eikonal equation [1] can be used for the basis of a geometrical optics analysis. The design of refractive optics has been extensively discussed in the literature [2], and the design of diffractive optics is discussed in reference 3. Refractive elements are produced using different techniques and described in reference 4. For example, combining a thermal flow technique with lithography, refractive lens arrays containing millions of lenses can be produced at a time [5].

Micro lenses are commonly used to couple light into and out of fibers and this is achieved with a plano-convex geometry with a single conic refracting surface. For example, a hyperboloid whose conic constant depends on the refractive index corrects spherical aberration and images collimated light perfectly on axis [6]. Thus, most design specifications call for a conic surface geometry with a specific conic constant. Conic tolerances vary with application, but approach ± 0.3 in demanding applications [7]. New or improved applications will drive tolerances lower, particularly as manufacturers move to passive rather active alignment to reduce cost. Ideally in-house metrology provides

conic estimates with measurement uncertainties an order of magnitude lower than the tolerance. The conic often is the key parameter considered, the lens however, is not likely to be a perfect conic. Therefore, the challenge is not only driving the tolerance of the conic constant down, but characterizing all the surface errors of the aspheric micro lens itself. This is needed to meet the metrology demand of the future and keep the metrology becoming a bottleneck in the manufacturing process.

There are two interferometry-based measurements are commonly used to characterize micro lens geometry, namely phase shifting interferometry [8,9] (PSI) and scanning white light interferometry [10,12] (SWLI). In some cases instrumentation software extracts the best fit conic constant, but the analysis is usually proprietary and it can be difficult for the lens manufacturer to estimate measurement uncertainty. A method of extracting the conic value is discussed in the literature [13] but this method assumes the surface is an exact conic, therefore surface error contribution to the conic uncertainty and lens performance is not easily assessed. Also the measurement methods proposed are not applicable to micro lenses and the analysis method not directly applicable to interferometric measurement techniques. Often manufacturers develop their own in-house (and proprietary) data analysis methods. The current practice of estimating the best-fit conic constant of the manufactured lens does not reflect the surface errors in the manufactured part either compared to the best-fit conic surface or compared to the design specifications (design shape) and estimating a combined uncertainty for the measurement is not done to our knowledge.

In our new analysis strategy, we present a non-proprietary, comprehensive, method of estimating the best fit conic and its uncertainty for micro lens measurements,

and propose a analysis of surface errors and an uncertainty for aspheric micro lens using a Zernike polynomial description for both analysis methods, the uncertainty is estimated by estimating input measurement uncertainties and folding this information into a Monte Carlo simulation to look at statistical variation of the output. Both methods are applicable to PSI and SWLI measurements and provide a non-proprietary comprehensive approach that both micro lens suppliers and customers can follow. The analysis is somewhat time-consuming and therefore not recommended for high-volume routine inspection, but rather for less frequent more detailed assessments. The analysis yields a realistic and comprehensive evaluation of measurement uncertainty and will validate in-house high-speed/high-volume measurements. Availability of such an approach will facilitate industry growth and the drive to improve device performance.

Our proposed method of extracting the best fit conic constant is an integration of a traditional least squares minimization with a Monte Carlo simulation [14]. The least-squares minimization is used to extract a best-fit conic value and the minimization is folded into a Monte Carlo simulation to allow the user to assess a final conic uncertainty. The analysis begins with the surface height profile extracted from a SWLI or PSI measurement. The SWLI data directly reflects the height profile (although residual tip/tilt misalignment must be removed and the lens sag estimated), and a height profile can be generated for PSI measurements by combining the optical path difference PSI data with a radius of curvature measurement. Next, a model of a conic surface is generated by estimating key parameters from the measurement, leaving only the conic constant as an unknown fit parameter. The key model parameters required are the base radius of curvature, the lens aperture, and the lens center. A final uncertainty in the conic value

must reflect all uncertainty contributions. For most measurements the dominant contributions will be noise in the measurement (reflected in repeatability and reproducibility) and the uncertainties of the three model parameters. The conic is a nonlinear function of these parameters and in such cases a Monte Carlo simulation is the best approach. Therefore we integrate the chi-square minimization process with a Monte Carlo simulation where probability distributions are used to iterate with different model parameters (estimated from measurement uncertainty) and data is randomly sampled from a measurement set to capture the impact of measurement repeatability. The result is a distribution of conic constants where the mean is an estimate of the best-fit conic and the width an estimate of the combined uncertainty. The approach allows uncertainty contributors (e.g. base radius of curvature and lens aperture) to be varied one at a time to provide insight into conic sensitivity. Because the conic is a nonlinear function of the measurement inputs, the sensitivity can be difficult to assess otherwise. This allows the user to determine which measurement input uncertainties dominate the output conic uncertainty, thus providing guidance on aspects of the measurement to improve.

Our proposal of describing the surface error of the micro lens uncertainty assessment is comprehensive, covering the major uncertainty contributors such as measurement noise (repeatability and reproducibility) and best-fit model uncertainty (when considering the surface error compared to a best-fit conic). We describe the approach for both scanning white light interferometry (SWLI) and phase shifting interferometry (PSI) measurements. A surface profile is first generated, and then the intended shape or the best-fit conic surface is subtracted, resulting in a residual surface error map. We fit the error map to a set of Zernike polynomials and iterate this process

through a Monte Carlo simulation to capture variation caused by measurement uncertainty. The result are distributions of Zernike coefficients describing the surface error, the means of which are estimates of the Zernike polynomial fit to the surface error and the distribution widths are estimates of the combined uncertainty. Individual uncertainty contributions can be varied one at a time to provide insight into measurement aspects that dominate the combined uncertainty and help establish a correlation with the manufacturing process and lens performance.

Part characterization during the manufacturing process is certainly necessary to validate part performance and tolerance conformity. Ideally it also provides information about the manufacturing process and can be used to monitor process variability and provide feedback to attain high yields. Our analysis yields parameters that capture only the errors in the part (particularly where the intended shape is removed from the measurement) and the error is a more direct reflection of the manufacturing process than the best-fit conic value. The surface error, combined with the best-fit conic surface or the intended shape, certainly can be used to assess part performance and validate tolerance conformity. Our approach strengthens the connection between the measurement output and the manufacturing process and is important to consider in the context of increasing yield.

The background and details of the two approaches are described in the subsequent eight chapters. It starts with mathematical expressions of geometrical models to describe the general aspheric micro lenses shape. Then the existing and predominantly used measurement techniques (SWLI and PSI) for surface profile measurement analysis are discussed in Chapter 3. We introduce the measurement set-ups, namely the Twyman-

Green interferometer and the scanning white light interferometer, from which we get an optical path difference (OPD) map and a surface height profile, respectively. As is well known, an asphere is needed to eliminate the traditional monochromatic aberrations. Chapter 4 describes the fundamental aberrations: spherical, coma, astigmatism, and distortion. The description of aberrations in terms of Zernike polynomials is also discussed.

Our new analysis strategy is based on both SWLI and PSI measurement techniques, and the main focus is to estimate the best-fit conic constant and surface error (the best-fit or the intended surface as subtracted from the measured surface). Since PSI measurements are strongly affected by misalignment, we investigate the misalignment sensitivity through simulation and experiment, and this is discussed in Chapter 5. In order to subtract the design shape from the measurement, the data is first converted into a surface profile for both SWLI and PSI. In order to assess a final uncertainty, certain parameters must be estimated from the measurement and the uncertainties in these parameters must be estimated. The task of generating the surface profile and estimating the uncertainty parameters is discussed in Chapter 6. Determining the best-fit conic surface by utilizing a chi-square minimization to optimize the best fit conic constant for both SWLI and PSI measurement techniques are rigorously described in Chapter 7. The Monte Carlo approach to find the overall distribution of the best fit conic constant caused by the individual and combined uncertainty parameters are also described in Chapter 7. The process of subtracting the intended (design) surface profile from the measurement is discussed in Chapter 8.

Two types of residual error surfaces are defined. The first is found by subtracting the intended shape from the profile generated from the measurement. The second is found by subtracting the intended shape from the best-fit surface as determined through the chi-square minimization process. This is done for both the PSI and the SWLI measurements. The residual surface error analysis and the estimation of the uncertainties based on Monte Carlo analysis using Zernike polynomials are discussed in Chapter 9. A summary on the comparison of the results of the two techniques is also given in the same chapter. Finally, conclusions and comments on the new analysis strategy are discussed.

We use a representative micro lens provided by Digital Optics Corporation (DOC) to demonstrate our analysis approach. The SWLI measurements were taken on a NewView™ 5000 and the PSI measurements on FISBA OPTIK μ phase® interferometer. The detailed description of our analysis is summarized in two papers at the end of this dissertation (APPENDIX A and APPENDIX B), namely “A Least-Squares Minimization and Monte Carlo Approach to Estimating the Conic Constant and Uncertainty for Microlens Measurements” and “A Monte Carlo analysis of Surface Errors for Aspheric Micro lens Manufacturing”. These will be submitted for publication to applied optics, optical technologies.

2. AN ASPHERIC SURFACE

Optical surfaces can be regarded as spherical or aspherical. Unlike aspherical surface, a spherical surface has a constant rate of change of slope (curvature). Since the rate of change of an aspheric surface slope varies over the surface, an asphere has the ability to correct aberrations (Chapter 4). For example, unavoidable spherical aberration (with a spherical lens) can be corrected using an aspheric lens. This will be discussed as a result of the basic geometry of optical surfaces in a later chapter. The following sections provide a basic understanding of the geometry relevant to our research and the new analysis strategy based on aspheric micro lens surface characterization.

2.1 The geometry of surfaces

Surfaces of the second order (quadrics) [15] for most applications are elliptical, hyperbolic or parabolic. The cross sections of these quadrics are second order [16].

2.1.1 Ellipsoid and ellipse

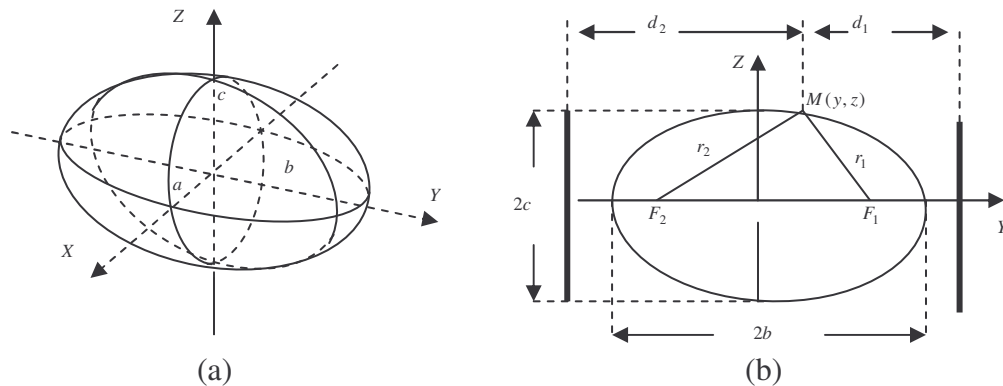


Figure 2.1: (a) Ellipsoid. (b) Ellipse (cross section of ellipsoid) with its directrices at distances d_1 and d_2 .

The ellipsoid equation is given by Equation 2.1,

$$\frac{x^2}{a^2} + \frac{y^2}{b^2} + \frac{z^2}{c^2} = 1 \quad (2.1)$$

where a , b , and c are semi-axes along x , y , and z , respectively. Three special cases can be derived from the ellipsoid. If $a=b > c$ we have an oblate ellipsoid of rotation, which is obtained by rotating the ellipse $x^2/b^2 + z^2/c^2 = 1$ with $a > c$. If $a=b < c$, we have a prolate ellipsoid of rotation, which is obtained by rotating the ellipse $x^2/b^2 + z^2/c^2 = 1$ with $a < c$. If $a=b=c$, we have a sphere $x^2+y^2+z^2=a^2$. Figure 2.1(b) is an ellipse (the cross section of the ellipsoid), defined as the set of all points $M(y, z)$ for which the sum of the distances from two fixed foci (F_1 and F_2) is constant (equal to $2b$). For any point M of the ellipse $r_1/d_1 = r_2/d_2 = e$, the eccentricity. Based on Figure 2.1(b), the distance between two foci of the ellipse is $\overline{F_1F_2} = f = \sqrt{b^2 - c^2}$ and consequently the eccentricity of an ellipse is $e = f/b$ ($e < 1$).

2.1.2 The hyperboloid of two sheets and hyperbola

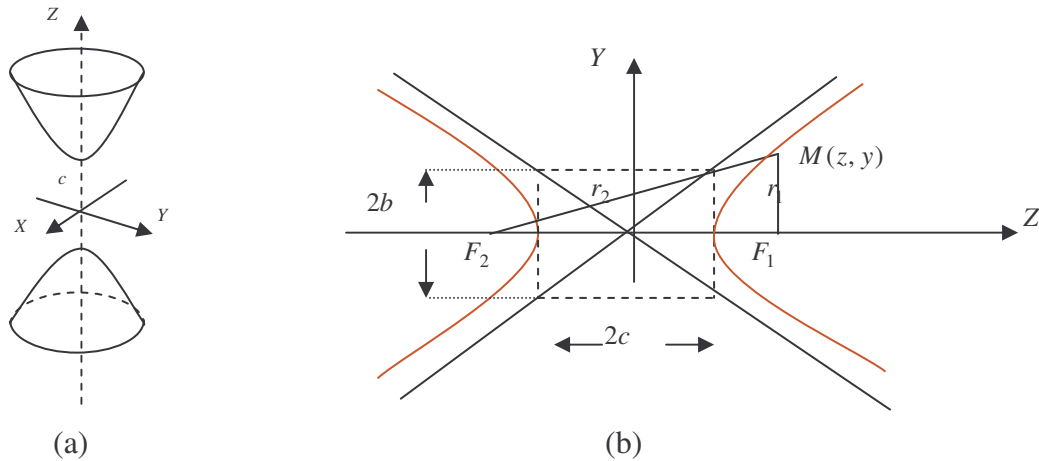


Figure 2.2: (a) Hyperboloid of two sheets. (b) A hyperbola (cross section of hyperboloid).

The ellipsoid equation is given by Equation 2.2,

$$\frac{x^2}{a^2} + \frac{y^2}{b^2} - \frac{z^2}{c^2} = -1 \quad (2.2)$$

where a , b , and c are semi-axes along x , y , and z respectively. If $a=b$, the hyperboloid can be obtained by rotating a hyperbola with semi-axes a and c about the axis $2c$, which is the real axis along z . Figure 2.2(b) is a hyperbola (the cross section of the hyperboloid), the set of all points $M(z, y)$ for which the difference of the distances from two fixed foci (F_1 and F_2) is constant (equal to $2c$). The imaginary axis is $2\sqrt{f^2 - c^2}$ and consequently the eccentricity of an ellipse is $e = f/c$ ($e > 1$). Therefore the normal form of the hyperbola is $z^2/c^2 - y^2/b^2 = 1$.

2.1.3 Elliptic paraboloid and parabola

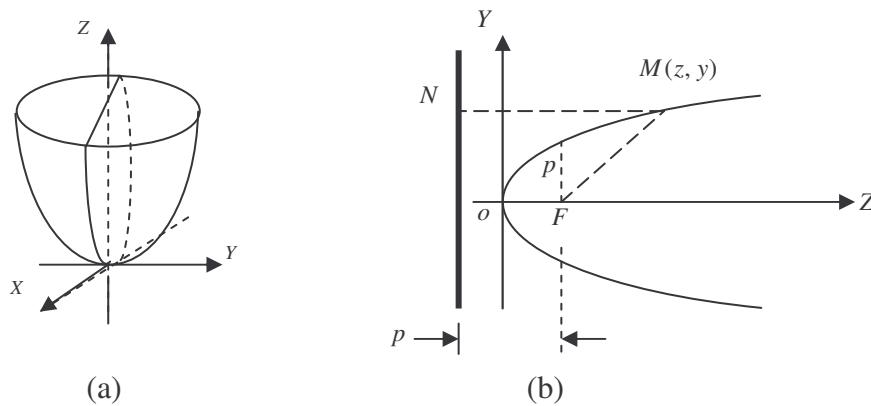


Figure 2.3: (a) Paraboloid. (b) Parabola (cross section of paraboloid).

The elliptic paraboloid equation is given by Equation 2.3

$$\frac{x^2}{a^2} + \frac{y^2}{b^2} = z \quad (2.3)$$

where a and b are semi-axes along x and y , respectively. The cross sections parallel to the z -axis are parabolas, and those parallel to the $x y$ plane are ellipses. If $a=b$ we have a paraboloid of rotation formed by rotating the parabola $z=x^2/a^2$ about its axis. A parabola is the set of all points M that are equally distant from a fixed point $F = (p/2, 0)$ and a

fixed line (the directrix). Since $\overline{MF} = \overline{MN} = x + p/2$, the eccentricity of a parabola is one.

The normal form of the parabola equation is $y^2 = 2pz$.

2.1.4 Tangential radius of curvature

The curvature of a line is the reciprocal of its radius. The curvature of a circle is constant because the radius is constant. The radius of curvature of curves other than circles changes from point to point. The curvature of a curve is defined as the rate at which the tangent changes with respect to the arc length, s . starting from this basic definition, based on Figure 2.4, differentiating $\tan \theta$ with respect to s and applying trigonometric relationships, the radius of curvature can be obtained as follows.

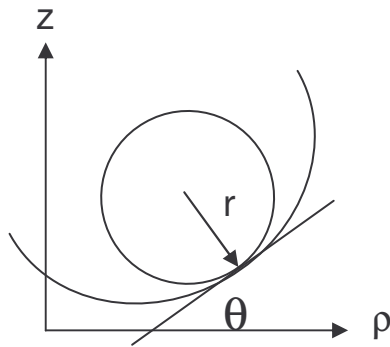


Figure 2.4: a curvature of Z as function of ρ

$$r = \frac{ds}{d\theta}, \quad \tan \theta = \frac{dz}{d\rho}$$

$$\sin \theta = \frac{(dz/d\rho)}{\sqrt{1+(dz/d\rho)^2}}$$

$$\cos \theta = \frac{1}{\sqrt{1+(dz/d\rho)^2}}$$

$$\frac{d}{ds}(\tan \theta) = \sec^2 \theta \frac{d\theta}{ds} = \frac{d}{ds} \left(\frac{dz}{d\rho} \right)$$

$$= \frac{d}{d\rho} \left(\frac{dz}{d\rho} \right) \frac{d\rho}{ds}$$

$$\sec^2 \theta \frac{1}{r} = \frac{d^2 z}{d\rho^2} \frac{d\rho}{ds}$$

but $\frac{d\rho}{ds} = \cos \theta$ and $\sec^2 \theta = (1 - \tan^2 \theta)$

$$(1 - \tan^2 \theta) \frac{1}{r} = \frac{d^2 z}{d\rho^2} \cos \theta$$

$$1 - \left(\frac{dz}{d\rho}\right)^2 = r \frac{d^2z}{d\rho^2} \frac{1}{\sqrt{1 + (dz/d\rho)^2}}$$

$$r = \frac{1 - \left(\frac{dz}{d\rho}\right)^2}{\frac{d^2z}{d\rho^2} \frac{1}{\sqrt{1 + (dz/d\rho)^2}}}$$

Therefore, the radius of curvature r is given by

$$r = \frac{\left\{1 + \left(\frac{dz}{d\rho}\right)^2\right\}^{3/2}}{\frac{d^2z}{d\rho^2}} \quad (2.4)$$

Note that r is positive for a concave and negative for a convex.

2.2 A micro aspheric sag equation

Aspheric surfaces cannot be described with only one radius of curvature. Instead, additional parameters like eccentricity are needed. The well-known sag equation can be derived as follows based on the prolate ellipsoid shown in Figure 2.5. The equation of this prolate ellipsoid is given by

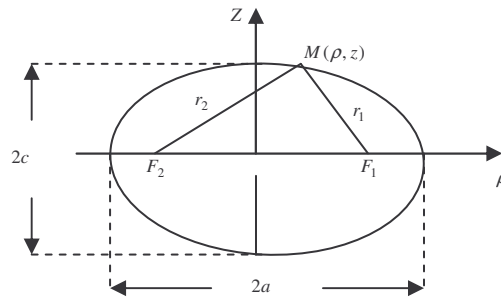


Figure 2.5: Prolate ellipsoid

$$\frac{\rho^2}{a^2} + \frac{(z-c)^2}{c^2} = 1, \text{ where } \rho^2 = x^2 + y^2 \quad (2.5)$$

$$\text{Using Equation 2.4, } r = \frac{\left\{1 + \left(\frac{dz}{d\rho}\right)^2\right\}^{3/2}}{\frac{d^2z}{d\rho^2}} = -\frac{a^2}{c} \quad (2.6)$$

and the definition of eccentricity (section 2.1.1),

$$e^2 = 1 - \frac{c^2}{a^2} \quad (2.7)$$

After factorizing Equation 2.5 and using Equations 2.6 and 2.7, we get a quadratic equation for z ,

$$(1 - e^2)z^2 + 2rz + \rho^2 = 0 \quad (2.8)$$

Solving the quadratic equation for z , we have

$$\begin{aligned} z &= \frac{-2r \pm \sqrt{4r^2 - 4(1 - e^2)\rho^2}}{2(1 - e^2)} = \frac{-2r \pm \sqrt{4r^2 \left[1 - (1 - e^2) \frac{\rho^2}{r^2}\right]}}{2(1 - e^2)} = \frac{-2r \pm 2r \sqrt{1 - (1 - e^2) \frac{\rho^2}{r^2}}}{2(1 - e^2)} \\ \Rightarrow z &= -\frac{r}{(1 - e^2)} \left(1 \mp \sqrt{1 - (1 - e^2) \frac{\rho^2}{r^2}}\right) \\ \text{or } z &= \frac{\frac{r}{(1 - e^2)} \left(1 - \left[1 - (1 - e^2) \frac{\rho^2}{r^2}\right]\right)}{1 \pm \sqrt{1 - (1 - e^2) \frac{\rho^2}{r^2}}} = \frac{-\frac{\rho^2}{r}}{1 \pm \sqrt{1 - (1 - e^2) \frac{\rho^2}{r^2}}} = \frac{-\frac{\rho^2}{r}}{1 \pm \sqrt{1 - (1 + k) \frac{\rho^2}{r^2}}} \end{aligned}$$

Rotationally symmetric general aspheric surfaces have additional terms and can be defined by the following more general form:

$$z = \frac{-\frac{\rho^2}{r}}{1 + \sqrt{1 - (1 + k) \frac{\rho^2}{r^2}}} - A_1 \rho^4 - A_2 \rho^6 - A_3 \rho^8 - A_4 \rho^{10} \dots \quad (2.9)$$

where $k = -e^2$ and the A_i s are referred to as the deformation constants.

Equating the A_i s to zero leads us to the sag equation of conic convex surfaces. The type of conic is determined by the value of conic constant k . The description of a general

convex aspheric lens (defined by Equation (2.9)) depends on the base conic surface. For example, the general aspheric deviation from a parabola is shown in Figure 2.6. Mathematically the deviation can be expressed as $z(k, A_i, \rho) - z(-1, 0, \rho)$. Furthermore, the

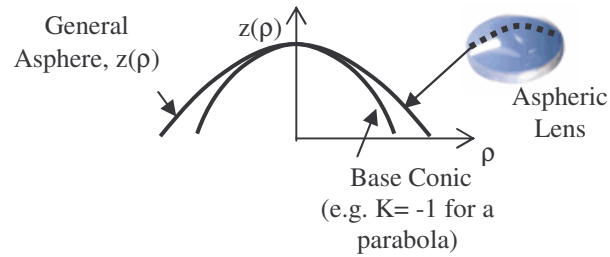


Figure 2.6 A general asphere with its base conic surface.

tangential radius of curvature given by Equation 2.4 can be simplified to give us its dependence on the radius of curvature of a sphere, the aperture radius ρ of the lens, and the conic constant K . This can be shown by substituting the first and second derivatives of z into Equation 2.9 (with the deformation constants set to zero). Hence, the tangential radius of curvature of a conic surface is given by Equation 2.10. The reciprocal of the

$$r = \frac{(1 - cK\rho^2)^{3/2}}{-c} \quad (2.10)$$

radius of curvature of a sphere is c . Based on this tangential radius of curvature equation, different conic surfaces can be appreciated. Figure 2.7(a) shows the profile of the tangential radius of curvature as the conic constant varies. The straight line shows the radius of curvature of a sphere (with $k=0$), which is constant for a sphere. As the conic

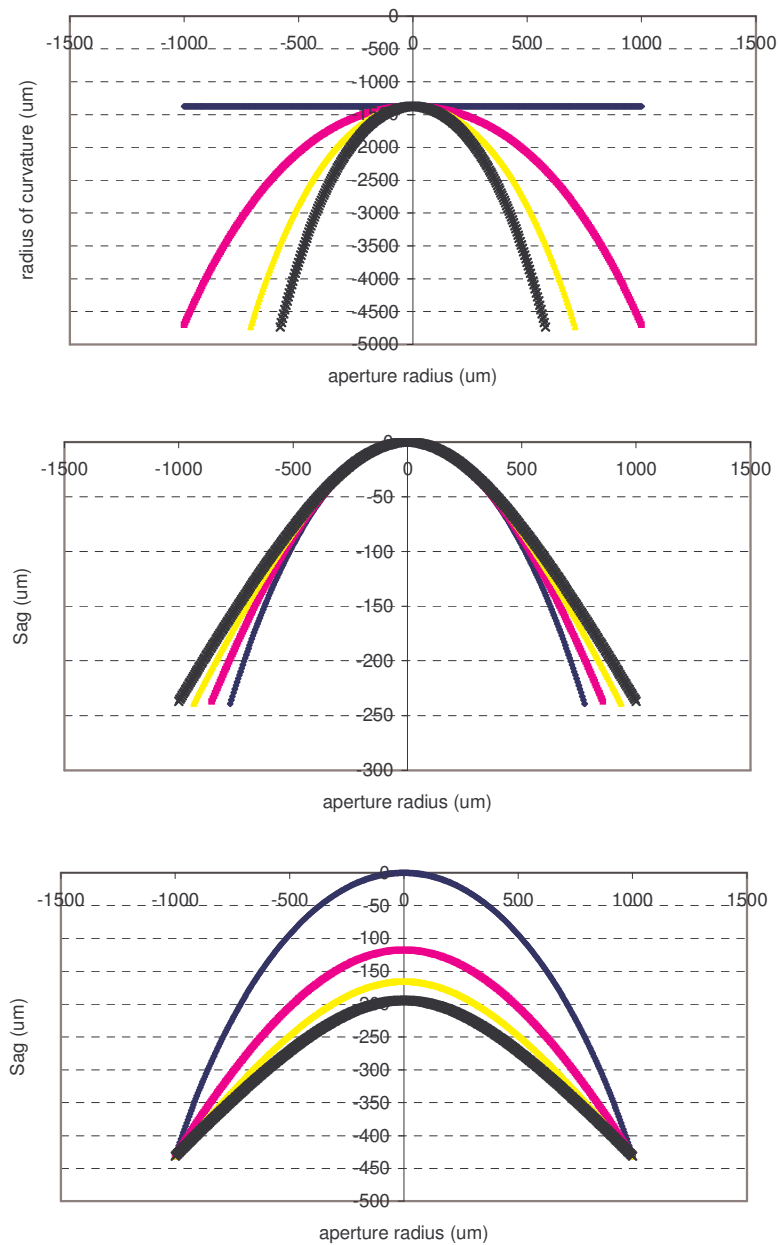


Figure 2.7: (a) Sag versus Radius of curvature dependence on conic constant. (b) Sag (based on aspheric equation with zero deformations) versus aperture coordinate, ρ , with fixed sag. (c) Sag versus aperture coordinate, ρ , with a fixed aperture radius. In all plots $R=1375\mu\text{m}$, $\rho_0 = 1000\mu\text{m}$, and $K=0, -2.4, -4.8, -7.2$. These values are from bottom to top for (b), and from top to bottom for (a) and (c).

constant increases, the curvature increases as well. Therefore, the curvature at the apex ($\rho=0$) is independent of the conic constant. In the same way the sag for the different conic surfaces can be compared, as shown in Figure 2.7 (b) and (c). It is shown in two ways, with a fixed aperture radius and with fixed sag. This visual observation tells us how all the parameters (aperture radius, radius of curvature and sag) are dependent on one another. Later in our analysis of the best-fit conic constant, we discuss the variation in aperture radius, sag, and radius of curvature in the optimization process.

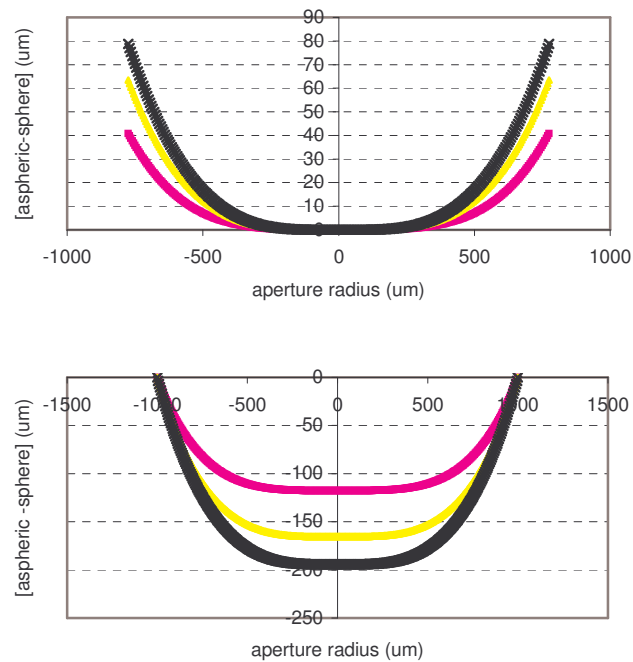


Figure 2.8: The deviation of aspheres from the sphere of radius 1375μm. the conic constants are -2.4, -4.8, and -7.2 from top to bottom for the top figure and from bottom to up for the bottom figure.

As described in Chapter 5, in a PSI measurement, the deviation of a general asphere from the best-fit sphere over the aperture is optical path difference (OPD). This

can be appreciated in Figure 2.8, which shows the deviation of aspheres from a sphere.

The base sphere is subtracted from all other aspheres shown in Figure 2.7.

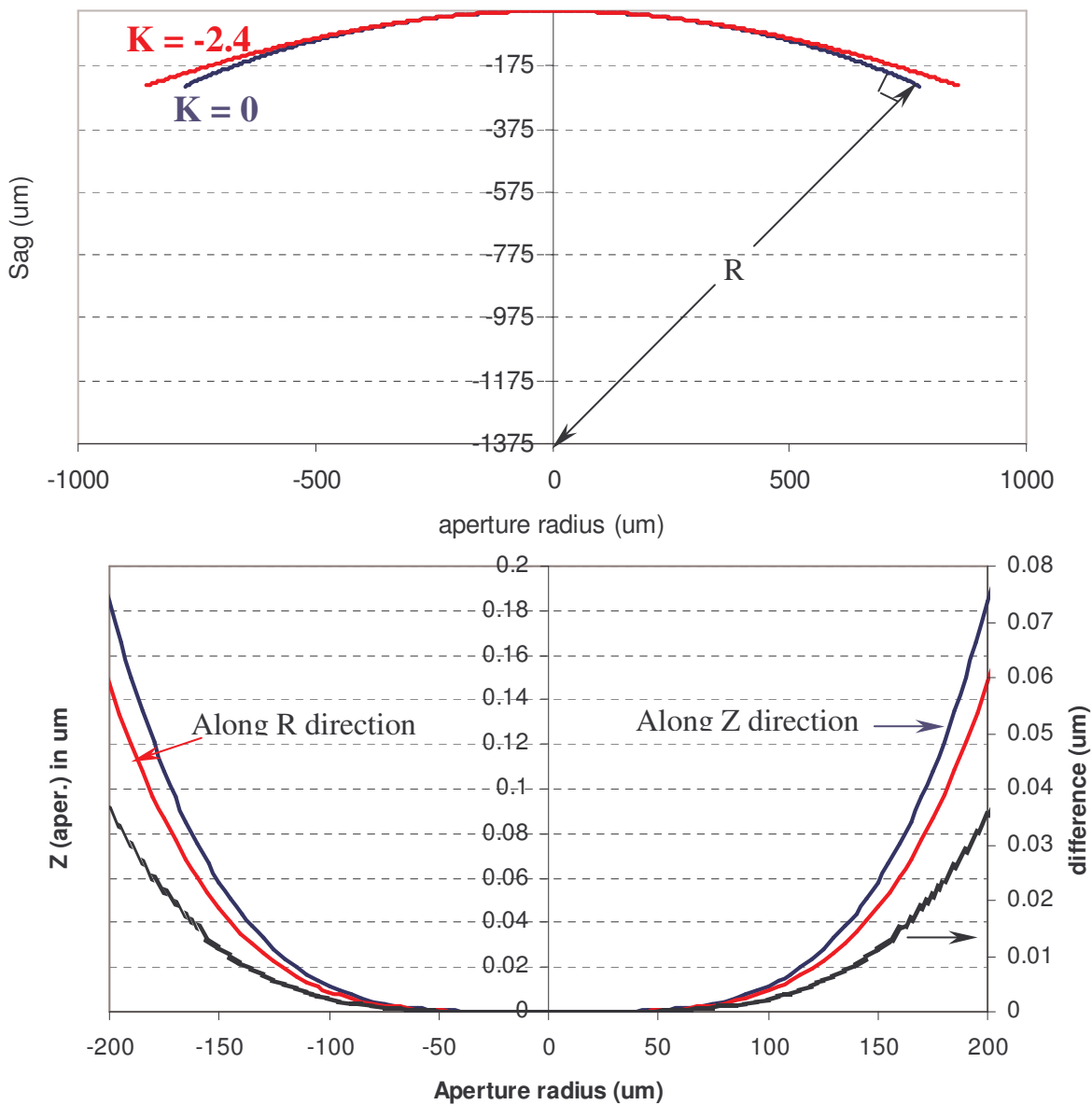


Figure 2.9: Subtracting the sphere from an asphere of $K=-2.4$. (a) The base radius of the asphere is the same as the radius ($R=1375\mu\text{m}$) of the sphere ($K=0$). (b) Plots namely, the difference between the two surfaces shown in (a) along Z direction versus the R direction, and the difference of these differences.

Subtracting the two surfaces along the z-direction is actually an approximation to the OPD. More rigorously, the OPD is the difference of these surfaces along the radial direction (Figure 2.9 (a)). Figure 2.9 (b) illustrates the OPD calculated the two ways and the difference between them (using $k = -2.4$ and $k = 0$ shown in Figure 2.9 (a)). A line passing through two points S and A is approximately perpendicular to the tangent of the sphere. Therefore, its slope is negative of the slope of the tangent using this approximation; the aperture radius of the asphere can be described by

$$\rho_A = \rho_S + \frac{Z_A - Z_S}{\left(-\frac{\partial Z_S}{\partial \rho_S}\right)} \quad (2.11)$$

The new Z_A using ρ_A is the surface of the asphere along the radial direction. Therefore in addition to the difference in the Z direction the difference in the R direction is the difference of the asphere with new Z_A and the sphere. As shown in the figure, the difference between the two OPD calculation methods approaches zero as the aperture coordinate approaches zero. For example (as shown in Figure 2.9), the error introduced by this approximation is less than 35 nm for an aperture of 200 μm . Therefore this kind of illustration can help us to see how much additional error can be introduced due to approximations related to aperture size considered.

3. APPROACHES TO MICRO ASPHERIC SURFACE PROFILE MEASUREMENTS

To describe interferometry measurements, one can revise the interference effect of light. The phenomenon where the intensity variation (maxima and minima) observed due to superposition of two-beams or more is known as interference. In general, beams can be obtained from a single source based on two methods, division of wave front and division of amplitude [17]. In the case of division of amplitude, a beam left a source is divided by a beam splitter in to two segments, which travels different paths before interfering. The general theory of interference helps us to describe these types of interferometers and their applications. Figure 3.1 which can be considered as division of wave front type shows a schematic interference experiment with polychromatic light from an extended source. Coherence theory describes the correlation between the two pinholes P1 and P2 at point Q using the analysis of the two-beam interference. The intensity at point Q is given by equation 3.1 [18].

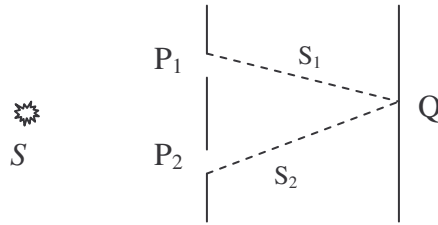


Figure 3.1: An interference experiment with Polychromatic light from an extended source S

$$I = I_1 + I_2 + 2\sqrt{I_1 I_2} |\gamma_{12}(\tau)| \cos[\alpha_{12}(\tau) - \delta] \quad (3.1)$$

Where the parameter τ and the phase difference δ have the values

$$\tau = \frac{s_2 - s_1}{c}, \quad \delta = 2\pi\nu\tau = \frac{2\pi}{\lambda}(s_2 - s_1)$$

and $|\gamma_{12}(\tau)|$ is known as complex degree of coherence.

The visibility of fringes at Q is given by

$$V = \frac{I_{\max} - I_{\min}}{I_{\max} + I_{\min}} = \frac{2\sqrt{I_1 I_2}}{I_1 + I_2} |\gamma_{12}(\tau)| \quad (3.2)$$

with the assumption of monochromatic light (if it ever existed), $|\gamma_{12}(\tau)|=1$, we will get the maximum visibility of fringes. Furthermore, the phase shift occurs faster than the changes that are being monitored, for monochromatic waves we can ignore $\alpha_{12}(\tau)$ and the expression of equation 3.1 is reduced to the simplified well-known interference equation for interferometers given by

$$I = I_1 + I_2 + 2\sqrt{I_1 I_2} \cos(\delta) \quad (3.3)$$

$$\text{where } \delta = \frac{2\pi}{\lambda} \Delta\varphi \quad (3.4)$$

$\Delta\varphi$ is the difference between the optical paths of the two waves

In this chapter, we described how to measure the surface profile of a micro lens based on two techniques, PSI and SWLI.

3.1 Phase Shifting Interferometry

Phase shifting interferometry (PSI) is a data collection and analysis method that can be applied to different types of interferometry setups used for optical testing. Here we are going to focus on a Twyman-Green setup. In this dissertation PSI will refer to phase shifting methods implemented with a Twyman-Green interferometer. Figure 3.2 shows Twyman-Green configuration as it is used to measure spherical or flat surfaces, depending on the wave front configured to reflect from the test surface. If the surface under test is flat a collimated beam exits the interfereometer to reflect from the ideally flat test surface. If the surface is spherical, a focusing element is used, such as an

objective. For example, in the case of a convex surface test, an objective is used that has a focal length larger than the radius of curvature of the convex surface. The numerical aperture must also be large enough to the entire surface of the lens is measured. A “null” fringe condition is used to measure surfaces, which leads to the lowest measurement uncertainty. But perfect alignment that leads to a null condition is never possible. When measuring aspheric surfaces, a spherical wavefront is usually reflected from the aspheric test surface, in which case even optimal alignment will not lead to a null condition. This necessarily compromises measurement uncertainty.

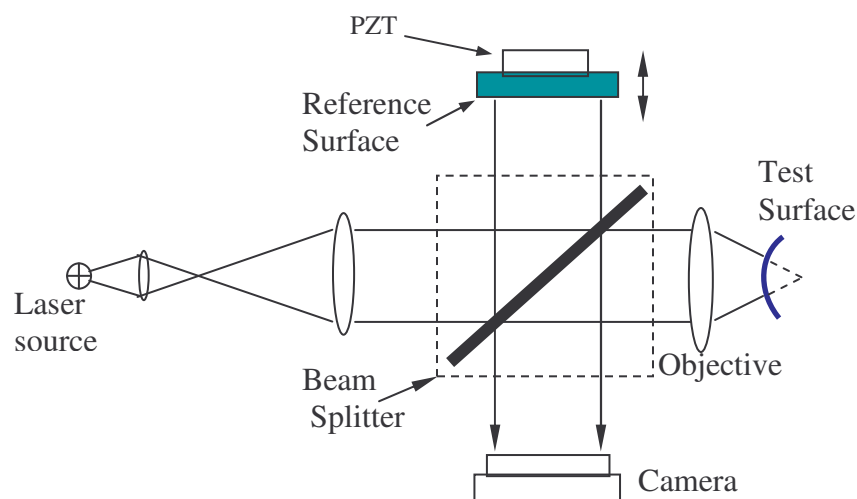


Figure 3.2 Twyman Green Interferometer setup

The PSI technique introduces a time varying phase shift to the reference beam, usually by moving the mirror at which this beam reflects using a piezoelectric transducer (lead-zinc-titanate (PZT)). The PZT expands or contracts with an externally applied voltage. The induced phase shift varies through a series of steps. Interferograms are collected at each step and analyzed using PSI algorithms [19] to find the phase difference between the two interfering beams. Assuming the reference beam is perfect, the measured phase difference between the two beams can be attributed to the test beam and therefore

form errors on the test surface. Based on wavefront phase analysis, the optical path difference (OPD) is related to the phase by Equation 3.4. If the surface is tested in reflection (Twyman Green setup) it is going to be

$$\delta = \frac{2\pi}{\lambda} (2h(x, y)) = \frac{4\pi}{\lambda} h(x, y) \quad (3.5)$$

The OPD in the expression represents the difference between surface profile under test and reference surface profile. Therefore, the phase measurement using PSI technique leads us to find out the OPD at each point from which the surface profile of our micro aspheric lens can be extracted. Note that phase unwrapping [20] must be performed to correct for phase discontinuity to the calculated phase.

3.1.1 Wave front phase detection and unwrapping

The phase can be calculated from the intensity distribution of Equation 3.6, which is derived by combining Equations 3.2 and 3.3 for a monochromatic wave. Where $I_0(x, y)$

$$I = I_0(x, y)[1 + V(x, y) \cos(\delta - \phi)] \quad (3.6)$$

is the background intensity given by $I_1 + I_2$, V is the fringe visibility and ϕ is the reference phase (zero in equation 3.3). PSI detection schemes are different in the way the reference phase is varied and the number of times and the rate at which the interference pattern is measured. Among the different PSI algorithms, the four-step algorithm and the fifth-step (extended four-step) algorithms are most frequently used.

The four-step algorithm calculates the phase distribution from four separate interferograms with reference phase values of $\phi = 0, \pi/2, \pi, 3\pi/2$. This is done by solving four equations from equation 3.6 at each reference phase values and solve for δ .

$$\delta = \tan^{-1} \left(\frac{I_2 - I_4}{I_1 - I_3} \right) \quad (3.7)$$

The fifth-step algorithm is an extended four-step algorithm. In addition we need the fifth measurement at $\phi = 2\pi$. The value of δ in this case is given by

$$\delta = \tan^{-1} \left(\frac{2(I_2 - I_4)}{I_1 - 2I_3 + I_5} \right) \quad (3.8)$$

Furthermore, the phase is not immune from errors in the phase step calibration. Hariharan showed that the 5-step algorithm, using a phase step of $\pi/2$ minimizes the sensitivity to calibration errors [21]. He solved for the phase difference using a general phase step, α (i.e. $\phi = -2\alpha, -\alpha, 0, \alpha, 2\alpha$) between frames. The same mathematical derivation shows that

$$\frac{\tan[\delta(x, y)]}{2 \sin(\alpha)} = \frac{I_2 - I_4}{2I_3 - I_5 - I_1} \quad (3.9)$$

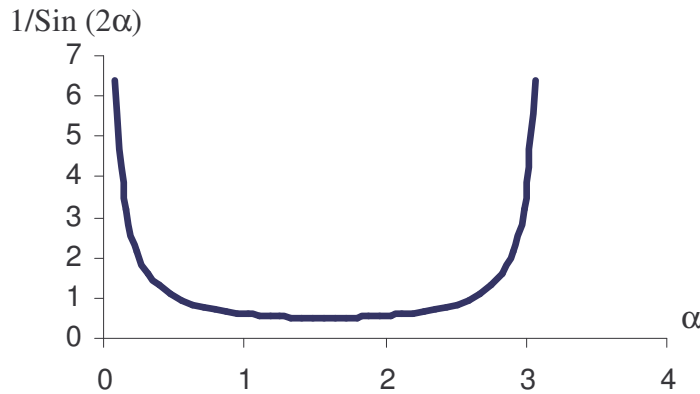


Figure 3.3: A plot of Equation 3.9 as a function of phase shift [21]

If we choose $\alpha = \pi/2$ we will get back to the five-step algorithm. Nevertheless, the actual phase shift may be $\pi/2 + \varepsilon$ instead. Then the corresponding measured phase will

be $\phi' = \phi + \Delta\phi$. Therefore, the new phase ϕ' and $\Delta\phi$ can be approximated as follows.

Assuming ε is small can be approximated using equation 3.9.

$$\tan \phi' = \frac{\tan \phi}{2\text{Sin}\left(\frac{\pi}{2} + \varepsilon\right)} \cong \frac{\tan \phi}{\left(1 - \varepsilon^2/2\right)} \quad (3.10)$$

$$\Delta\phi = \frac{\phi}{\left(1 - \varepsilon^2/2\right)} - \phi \cong \left(\varepsilon^2/4\right)\sin(2\phi) \quad (3.11)$$

For example, the maximum error is about 0.04° for a maximum of 3.1° change in the phase shift. To have a good picture of how this method tolerates relatively large calibration errors, consider the plot of $1/\sin(2\alpha)$ versus α , shown in Figure 3.3. The plot shows a broad minimum centered at $\pi/2$.

One more correction has to be considered before the phase determination is complete. Based on the PSI algorithms, the phase calculations are sufficient for modulo π calculation only. In other words, phase discontinuity occurs because of the limited range of angles ($-\pi/2$ to $\pi/2$) where arctangent is defined. To correct this and produce the wavefront phase modulo 2π , we can extend the calculated phase range from 0 to 2π . Returning the calculated phase to 0 whenever the actual phase is a multiple of 2π gives us the raw phase data. Then the wavefront reconstruction process is carried on by removing the 2π discontinuity introduced in the raw phase data. This can be done by adding multiples of 2π to the adjacent regions, which is known as phase unwrapping. From the point of view of spatial sampling, the phase unwrapping is straight forward as long as the recorded interferograms satisfy the Nyquist criteria (at least two pixels per fringe) and the phase map can be assumed to be smooth. In other words, fringe density larger than the Nyquist frequency (half the sample frequency) can not be resolved to reconstruct the

wave front phase. One can find extensive and rigorous discussions on phase measurements and phase unwrapping in references 22 and 23.

3.2 Scanning white light interferometry measurement

Scanning white light interferometry (SWLI) is a powerful technique to estimate surface profiles without the ambiguity in the fringe order number. The method is also referred to as optical interferometric profilometry. Since the coherence length of white light is short, good contrast fringes are achieved only when the two paths of an interferometer are equal. Therefore, an object's height information can be retrieved by having one beam reflect from the surface and detecting a coherence peak.

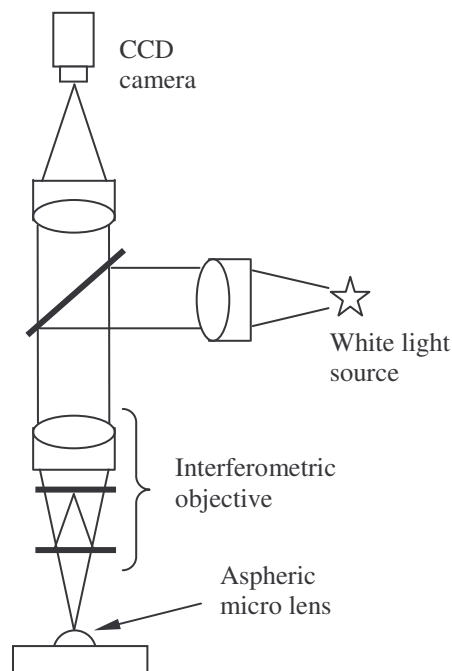


Figure 3.4: Optical schematics of SWLI

One of the optical interferometric profiling instruments is the traditional Mirau interferometer shown in Figure 3.4. It is based on standard microscope where the objective has been replaced by an interferometric objective (Mirau). Since extended

source is used; it can be referred as SWLI microscope. Mirau interferometers contain two small plates between the objective and the test surface. One of the two plates contains a small reflective spot that acts as the reference surface, and the other plate is coated on one side to act as a beam splitter.

Light from the illuminator is incident on the microscope objective. Part of the light goes to the test surface and the rest of the light is reflected by the reference surface. The beams combined again at the beam splitter. The two light beams interfere and are recorded on the CCD array. The Mirau interferometer is mounted on a piezoelectric transducer (PZT). During vertical motion of the interferometer relative to the test surface a phase shift is introduced only in one arm because the distance from the lens to the reference surface is fixed. Since a phase shift is introduced while interference fringes are recorded, it is possible to perform either phase shifting interferometry or vertical scanning coherence peak sensing interferometry [24].

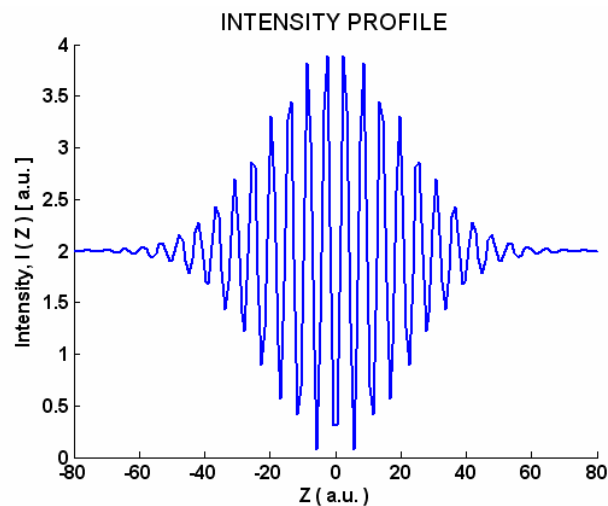


Figure 3.5: Intensity profile as a function of position

The intensity recorded for a single point on the surface as the surface is translated through focus looks like the plot shown in Figure 3.5. The plot shows light intensity as a

function of the test surface position. Such a plot is called a correlogram [25].

According to the Wiener-Khintchine theorem [26], the correlogram width is proportional to the coherence length and inversely proportional to the spectral width of the source. The relationship between correlogram length and the spectral width can be understood as follows. Based on the Wiener-Khintchine theorem, the normalized coherence function is the Fourier transform of the power spectral density of the source,

$$\gamma(\tau) = \int g(\nu) e^{-i2\pi\nu\tau} d\nu \quad (3.12)$$

If we assume the power spectral density ($g(\nu)$) of the source by Gaussian distribution, the normalized spectral density has the form

$$g(\nu) = \frac{1}{2\sqrt{\pi}\Delta\nu} \exp\left[-\left(\frac{\nu-\nu_0}{2\Delta\nu}\right)^2\right] \quad (3.13)$$

Therefore, the normalized coherence function with this spectral density becomes

$$\gamma(\tau) = \exp(-4\pi^2\tau^2\Delta\nu^2) \exp(-i2\pi\nu_0\tau) \quad (3.14)$$

where $\tau = \frac{2(z-z_0)}{c}$, (c is the speed of light). Assuming the intensity in both arms of the

interferometer is about the same, Equation 3.1 can be rewritten as

$$\begin{aligned} I(z) &= I_0 \operatorname{Re}\{1 + \gamma(\tau)\} \\ &= I_0 \left\{ 1 + \exp\left[-\left(4\pi \frac{z-z_0}{c} \Delta\nu\right)^2\right] \cos\left(4\pi \frac{z-z_0}{c} \Delta\nu\right) \right\} \end{aligned}$$

substituting the effective bandwidth $\Delta\nu$ by $c/4\pi L$ (where L is the coherence length) the intensity recorded is given by

$$I(z) = I_0 \left\{ 1 + \exp\left[-\left(\frac{z-z_0}{L}\right)^2\right] \cos\left(4\pi \frac{z-z_0}{\lambda_0}\right) \right\} \quad (3.15)$$

Therefore, the correlogram width is directly proportional to the source coherence length and therefore inversely proportional to the spectral bandwidth.

Once we understand the characteristics of intensity recorded using white light as our source we need to be able to transform this information to our surface under test surface profile. As in reference 27, two families of white light profilometry methods are described. One family is based on the detection of the peak of the coherence envelope, which modulates the interference fringes [28-31]. The second family is based on the analysis of the white light interference phase [32-35]. Since we used New ViewTM5000, scanning white light interferometry instrument, its data processing is accomplished by frequency domain analysis (FDA) [34].

3.2.1 Frequency domain analysis

Frequency domain analysis (FDA) is a method of processing interferograms to extract surface profiles. FDA can be visualized as shown in Figure 3.6 [36]. The transformation

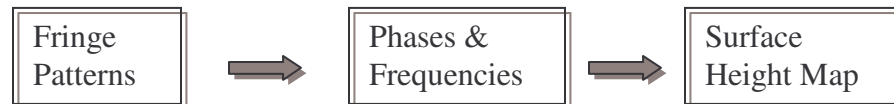


Figure 3.6: FDA methodology. Data are transformed to the frequency domain to calculate surface height.

from fringes to phases is accomplished with an algorithm such as the five-bucket algorithm discussed in Section 3.1.1. In an ideal dispersion-corrected interferometer with a monochromatic source, the phase is related to height as described by Equation 3.5. The phase can be redefined as $\delta = kz$ by defining k as the wave number of the source light (equal to $2\pi/\lambda$). The variable z is the round trip ($2h$) optical path difference. Defining the

rate of change of wave number by Equation 3.16 has some advantages over conventional phase shifting interferometry such as the reduction or elimination of 2π phase ambiguities,

$$\frac{d\delta}{dk} = z \quad (3.16)$$

Therefore, this equation tells us the familiar linear equation, which can be given by

$$\delta = z.k + \delta_0 \quad (3.17)$$

The graphical representation of single wavelength interference in the spatial frequency (wave number) domain using Equation 3.17 leads us directly to the test surface height from the slope. As discussed in Section 3.1.1, the result still suffers from phase ambiguity as long as we use only a single wavelength (laser source). To use Equation 3.17 to our advantage, we have to change our source to white light. In a simplified way, each frequency of a broadband source is governed by Equation 3.17. Therefore, the single wavelength FDA can be extended to white light FDA. Individual frequencies contributing to the interference pattern (Figure 3.5) have their own phase information to estimate the height at each point. The phase information from individual contributors can be found by

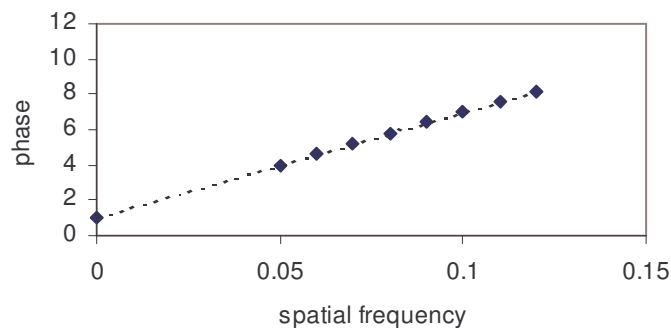


Figure 3.7: An example of phase information for a range of frequencies k

a Fourier transform. The phase information in the Fourier-transformed data can be plotted as shown in Figure 3.7. This is the principle of FDA in the New ViewTM5000. The data consists of an array of correlograms, one for each pixel, representing the variation in intensity as a function of position. With the FDA, individual correlograms are processed and the final surface profile is generated. Extensive discussions on FDA in relation to scanning position can be found in reference 37.

4. WAVE FRONT ABERRATION

The form error on micro-lense degrades the optical performance. The reflected wave from the lens or transmitted wave through the lens altered due to this form error. Hence the wavefront has errors known as the wavefront aberrations. A wave front can be conveniently described as a linear combination of Zernike polynomials, which separate out the primary aberrations. Geometric form errors in the lens are the primary cause of these aberrations. One can also describe the geometric form errors in terms of aberrations and a Zernike polynomial description. For example, an astigmatic form error on a lens will lead to astigmatism in the transmitted wave front. These two perspectives come together in an interferometric measurement where the geometric form error on a lens surface is directly imprinted into the reflected wave front used to test the lens. The aberrations in this wave front are measured and used to infer the lens geometry. This chapter provides a review of low-order aberration theory to provide the necessary background.

There are different approaches to studying aberrations. Ideal image formation, based on Gaussian optics, requires that all rays from each object point (field point) pass through the paraxial conjugate image point, with all rays having the same optical path length. Deviations from this perfect condition coincide with errors or deviations in the spherical wave front exiting the optical system. These deviations are known as wave front aberrations. The phenomenon can be studied using ray tracing or algebraic analysis [38]. As an introduction, this chapter reviews the well-known primary aberrations and their interferometric patterns as observed in an interferometer (interferograms).

There are five primary monochromatic aberrations that deteriorate the image, spherical aberration, coma, astigmatism, field curvature, and distortion. Field curvature and distortion do not affect the definition of the image but rather its location. Here we describe the first three that actually affecting the sharpness of the image.

4.1 Primary aberrations

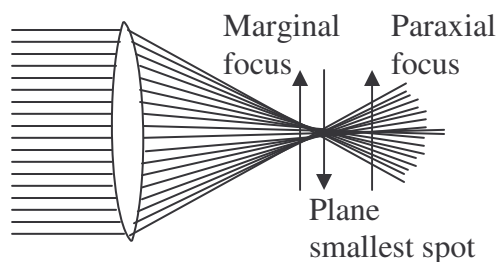


Figure 4.1: Spherical aberration at the paraxial focus.

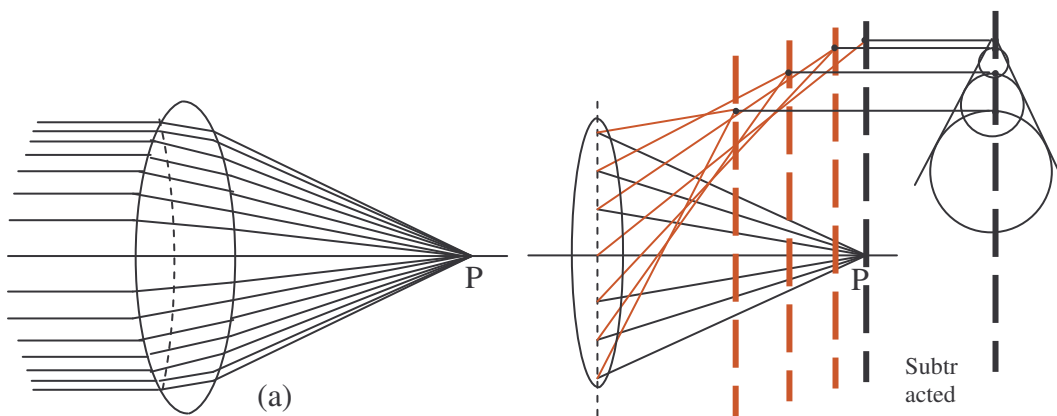


Figure 9.6: (a) Bias corrected OPD measurement (b) reproduced OPD map from Zernikes (c) randomly subtracted

Figure 4.1 shows refraction of parallel rays as they travel through a spherical lens toward the paraxial focal plane. The paraxial rays meet as expected at the paraxial focus. The rays farther from the optical axis cross the axis to the left of the paraxial focus, and the marginal rays cross the axis the farthest to the left. Rotating this diagram about the

optical axis produces a blurry circular image in the paraxial plane. This kind of blurring is caused by spherical aberration.

An aberration due to skew rays is coma. In a very simplified picture, assume Figure 4.2(a) shows a set of rays on a cylinder that is centered about the axis of a lens so that all the rays are meridional. Now tilt this cylinder of rays a displacement an angle to the optical axis while holding fixed the intersection point of each ray with the dotted circle on the front of the lens. Let the top and bottom meridional rays meet at a point P in image space and consider it to define the location of the image plane (see Figure 4.2(b)). The skew ray just below the uppermost ray will pass through this plane very close to the point P and let's say to the right. In the same way the lower rays pass through the plane close to the point P and to the left. Rays in between form a series of points that are close the curve giving the circle of coma. In the same way, a series of image planes are created by meridional rays and a series of circles by the skew rays to create a complex structure which is called just coma.

When an object point lies an appreciable distance from the optical axis, the incident cone of rays will strike the lens asymmetrically, giving rise to astigmatism. In other words, the failure of sagittal and tangential rays to produce a single image in a lens corrected for both spherical aberration and coma is known as astigmatism. As it is shown in Figure 4.3, sagittal line and tangential line due to the tangential fan and sagittal fan are on two different image planes. If we consider an image plane half way between the two, we will get an ideal case of a circle. Other positions produce ellipses.

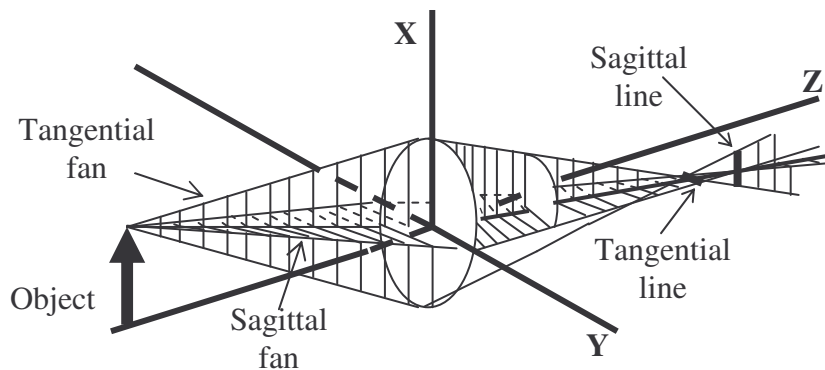


Figure 4.3: Astigmatism: a failure of sagittal and tangential to produce single image in a lens corrected for both spherical al aberration and coma

4.2 Interferograms of primary aberrations

Ideally as parallel rays passing through a lens (Figure 4.4) should meet at the Petzval surface. Instead, they meet at different surfaces such as point P due to the optical path difference. The optical path difference (path via O – path via Q) is given

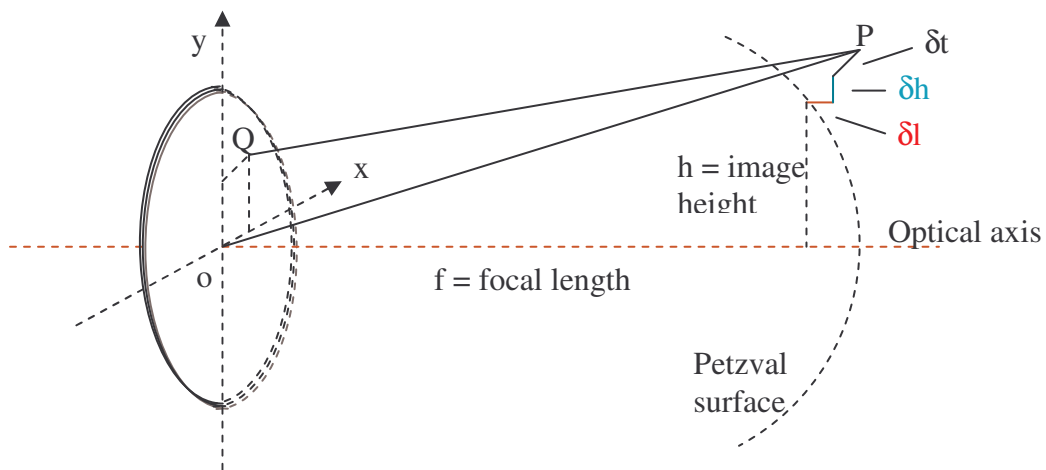


Figure 4.4: A plane wave falling on the front surface of a lens and arriving at point P [39]

by [39] where g_1 is a measure of spherical aberration, g_2 is of coma, and g_3 is for

$$\begin{aligned}
 OPD = & \frac{g_1}{4}(x^2 + y^2)^2 + \left(\frac{h}{l}\right)g_2y(x^2 + y^2) + \frac{1}{2}\left(\frac{h}{l}\right)^2 g_3(x^2 + 3y^2) + \\
 & + \frac{1}{2}\frac{\delta l}{l^2}(x^2 + y^2) + \frac{\delta h}{l}y + \frac{\delta x}{l}x
 \end{aligned}
 \tag{4.1}$$

astigmatism and l is the distance of the image from the back surface of the lens. The other two aberrations, curvature and distortion are related to δl and δh of equation 4.1. In most literatures equation 4.1 is rewritten as equation 4.2 for convenience. Where A, B, C, D, E,

$$OPD = A(x^2 + y^2)^2 + B(x^2 + y^2) + C(x^2 + 3y^2) + D(x^2 + y^2) + Ey + Fx
 \tag{4.2}$$

and F are respectively measures spherical aberration, coma, astigmatism, longitudinal, vertical, and lateral displacements of the center of curvature of the convex lens from the ideal paraxial image-point.

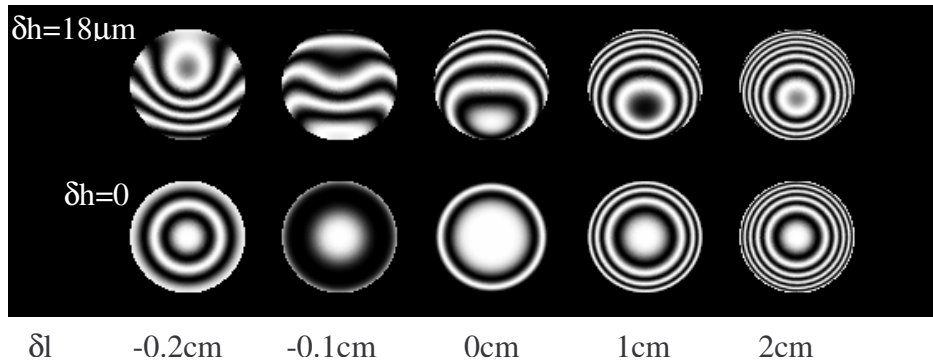


Figure 4.5: Spherical aberration with and without vertical displacement of $18\mu\text{m}$ in relation to longitudinal displacement

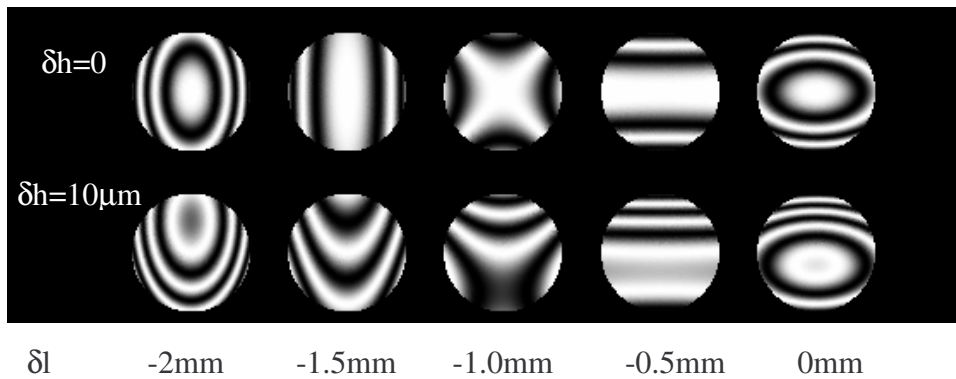


Figure 4.6: Astigmatism with out and with vertical displacement of $10\mu\text{m}$ in relation to longitudinal displacement

The characteristic patterns of primary aberrations are very helpful in optical testing. To illustrate this patterns let's assume a lens with 30cm focal length supposed to be viewed with He Ne laser ($\lambda=0.6328\mu\text{m}$), the direction of the incident beam being inclined at 5° to the axis of the lens. We also assuming the lens have $g_1=2\mu\text{m}$, $g_2=25\mu\text{m}$, and $g_3=70\mu\text{m}$. Based on these assumptions we relate Equation 4.1 and Equation 4.2 to find the coefficients A, B, and C related to spherical, coma, and astigmatism respectively. it can easily be found that $0.5\mu\text{m}$, $2.2\mu\text{m}$, and $3\mu\text{m}$ are the values of A, B, and C.

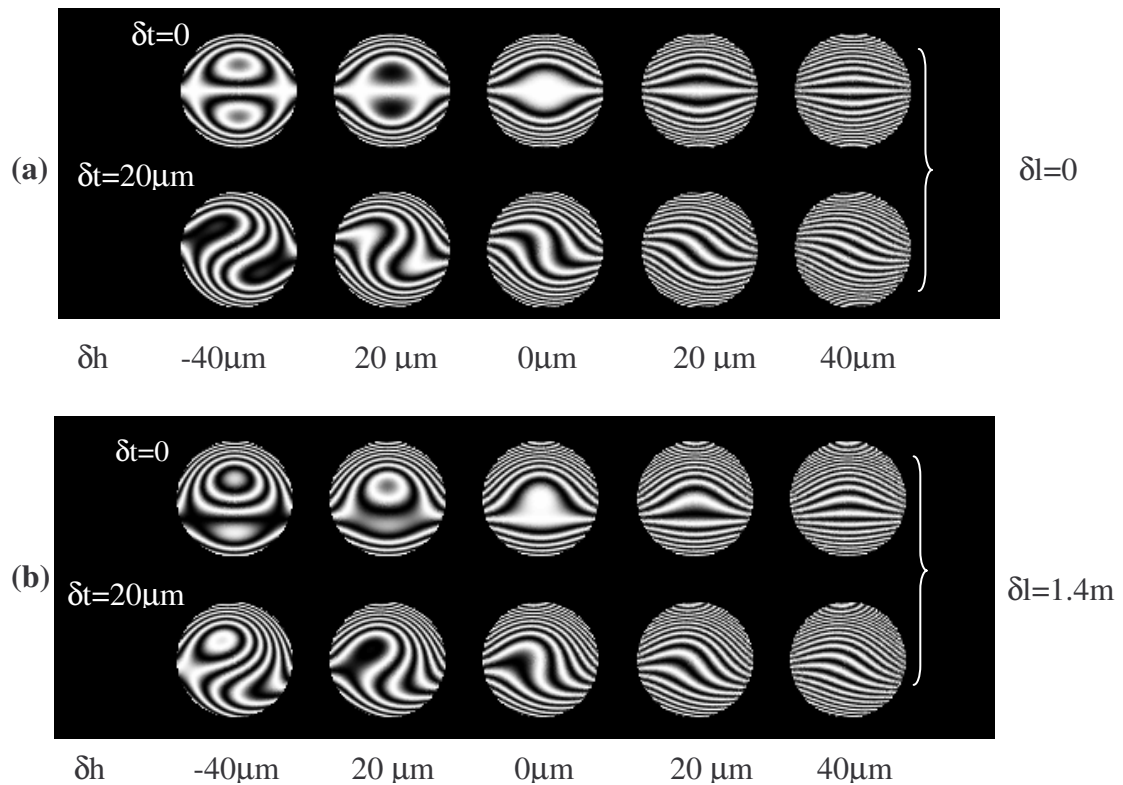


Figure 4.7: (a) Coma with out longitudinal displacement: with out and with $20\mu\text{m}$ lateral displacement. (b) Coma with 1.4m longitudinal displacement: with out and with $20\mu\text{m}$ lateral displacement

respectively. Once we know these values others (longitudinal, vertical, and lateral) can be varied to see the effects of aberrations. Therefore, those calculated values are at about the

best focus of the lens. The effect of pure spherical, pure astigmatism, and pure coma as a function of longitudinal, vertical, and lateral displacements are shown in Figures 4.5, 4.6, and 4.7. As it is shown in all Figures, each pure aberration of the lens is distorted as the displacement values vary. Even though the discussion here is based on the lens under test through transmission, it helps us to enhance our visual perception of interferograms representations of wave front aberrations.

4.3 Power series expansion of wavefront aberrations

Here we present a theoretical treatment of geometric aberrations based on the wave phenomenon of light. Consider a collimated wave striking a perfect lens (Fig. 4.8 (a)). The wave front perpendicular to the emerging ray can be considered a reference wave front, which is a subaperture of a sphere. If the lens has aberrations, the emerging wave front is not perfectly spherical (Fig. 4.8 (b)). The deviation of the wave front from the reference is known as wave front aberration. As an example, we can derive the first

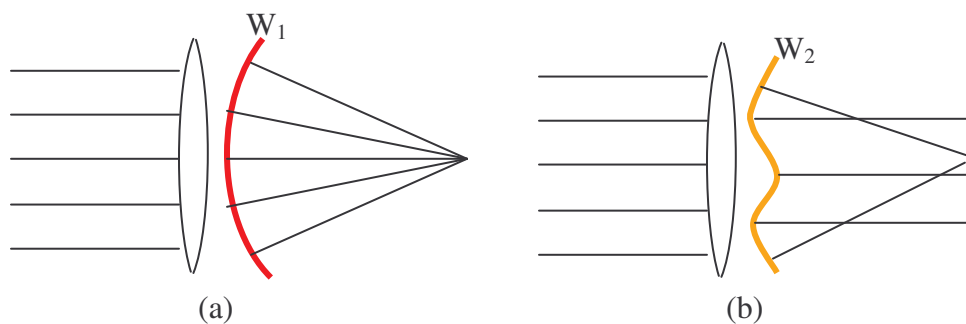


Figure 4.8: (a) Perfect spherical wave front (W_1) is perpendicular to the emerging rays. (b) Distorted wave front (W_2)

order aberrations as follows, based on the reference 40. As shown in Figure 4.9, a reference sphere of radius R ($P'O'$) is centered at P' . Consider the point P in line with O' . In the x y plane the wave front error W is given by

$$\begin{aligned}
 W = R - \overline{P'P} &= \sqrt{x'^2 + y'^2 + z'^2} - \sqrt{(x'-x)^2 + (y'-y)^2 + z^2} \\
 &= z' \left[\sqrt{1 + \frac{x'^2 + y'^2}{z'^2}} - \sqrt{1 + \frac{(x'-x)^2 + (y'-y)^2}{z'^2}} \right]
 \end{aligned} \tag{4.3}$$

Assuming that z' is much larger than x' and y' , the equation can be expanded by the binomial theorem of the form

$$(1+b)^{1/2} = 1 + \frac{b}{2} - \frac{b^2}{8} + \frac{3b^3}{48} - \frac{5b^5}{128} + \dots \tag{4.4}$$

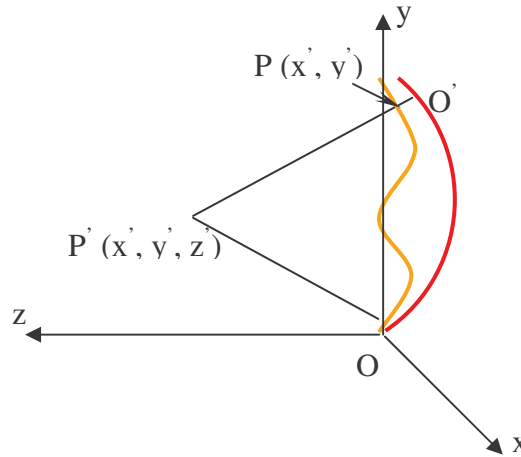


Figure 4.9 Wave aberration (O'P): Radius of a sphere R minus PP'

To derive the first order, consider the first two terms of the binomial expansion and apply it to Equation 4.3. Setting $x' = 0$, letting the image height $y' = h$, and changing to polar coordinates ($y = \rho \cos \varphi$, $x = \rho \sin \varphi$) the wave front error becomes

$$W = \frac{2h\rho \cos \varphi - \rho^2}{2z^2} \tag{4.5}$$

In power series form it can be rewritten as

$$W(h, \rho, \varphi) = w_{020}\rho^2 + w_{111}h\rho \cos \varphi \tag{4.6}$$

In the same way we can derive the third order aberration in power expansion form if we consider the first three terms of Equation 4.4, and so on for the fourth, the fifth, etc. A few terms of the power expansion form of the wave aberration are given in Table I [41]. In general, with l , m , and n as positive integers or zero, the power series expansion has the form $w_{l+m,n+m,m} h^{l+m} \rho^{n+m} \cos^m \varphi$ provided that $n = m = 0$ or $l = m = 0$ and $n = 2$, or $l = n = 0$ and $m = 1$ is omitted.

4.4 Zernike Polynomials

Wave front aberrations can be represented by the well-known Zernike polynomial set. The set is orthogonal and defined on a unit circle [42-45]. The Zernike polynomials of the form

$$Z_n^l(x, y) = Z_n^l(\rho \sin \theta, \rho \cos \theta) = R_n^l(\rho) e^{il\theta} \quad (4.7)$$

where $l \geq 0$, $l < 0$, $n \geq 0$ are integers, and $n \geq |l|$ is even. Based on the orthogonality normalizing properties, the radial component of the Zernike polynomial is given by [46]

$$R_n^{\pm m}(\rho) = \sum_{s=0}^{\frac{n-m}{2}} (-1)^s \frac{(n-s)!}{s! \left(\frac{n+m}{2} - s\right)! \left(\frac{n-m}{2} - s\right)!} \rho^{n-2s} \quad (4.8)$$

$$R_n^{\pm m}(1) = 1, \quad \text{where } m = |l|.$$

Instead of the complex representation of Equation 4.7, the real Zernike polynomials can be written as

$$\begin{aligned} Z_n^m &= R_n^m(\rho) \cos m\theta \\ Z_n^{-m} &= R_n^m(\rho) \sin m\theta \end{aligned} \quad (4.9)$$

Therefore, the wave front function $W(\rho, \theta)$ of degree g can be expressed as a linear combination of Zernike polynomials as

$$W(\rho, \theta) = \sum_{n=0}^g \sum_{m=0}^n R_n^m (a_{nm} \cos m\theta + a_{nm} \sin \theta) \quad (4.10)$$

where m takes only values with the same parity as n .

The ordering of the polynomials is not universally agreed upon, and therefore varies in literature. Two ordering schemes are common, the ISO nomenclature [47] and another one described in references 46 and 48. Both ordering can be visualized (based on equation 4.10) as in Figure 4.11. The ISO nomenclature follows V shaped dotted lines and Born and Wolf and others kind of nomenclature is the one with black arrow indicated. Table II summarizes the two ways orderingschemes For example, order 4 (No. 8) of ISO representation and order 5 (No. 12) of Born & Wolf representation are the same spherical aberration polynomial (with $\theta = 0$ from the graphical representation of Figure 4.10).

4.5 Relationship between Zernike Polynomials and wave front aberrations

The wave front aberration as any function can be expressed in terms of the combination of Polynomials (Zernikes). This is indicated in equation 4.11. For example, the third order aberrations can be related to Zernikes as described in reference 47. Here we are extending this to the fifth order aberrations.

Table I: Power series expansion of wavefront aberration [41]

n	m=0	m=1	m=2	m=3	m=4	m=5
Third order aberrations						
0		$w_{311}h^3\rho \cos \varphi$	$w_{222}h^2\rho^2 \cos^2 \varphi$			
2	$w_{220}h^2\rho^2$	$w_{131}h\rho^3 \cos \varphi$				
4	$w_{040}\rho^4$					
Fifth-Order aberrations						
0		$w_{511}h^5\rho \cos \varphi$	$w_{422}h^4\rho^2 \cos^2 \varphi$	$w_{333}h^3\rho^3 \cos^3 \varphi$		
2	$w_{420}h^4\rho^2$	$w_{331}h^3\rho^3 \cos \varphi$	$w_{242}h^2\rho^4 \cos^2 \varphi$			
4	$w_{240}h^2\rho^4$	$w_{151}h\rho^5 \cos \varphi$				
6	$w_{060}\rho^6$					
Seventh-Order aberrations						
0		$w_{711}h^7\rho \cos \varphi$	$w_{622}h^6\rho^2 \cos^2 \varphi$	$w_{533}h^5\rho^3 \cos^3 \varphi$	$w_{444}h^4\rho^4 \cos^4 \varphi$	
2	$w_{620}h^6\rho^2$	$w_{531}h^5\rho^3 \cos \varphi$	$w_{442}h^4\rho^4 \cos^2 \varphi$	$w_{353}h^3\rho^5 \cos^3 \varphi$		
4	$w_{440}h^4\rho^4$	$w_{351}h^3\rho^5 \cos \varphi$	$w_{262}h^2\rho^6 \cos^2 \varphi$			
6	$w_{260}h^2\rho^6$	$w_{171}h\rho^7 \cos \varphi$				
8	$w_{080}\rho^8$					
Ninth-Order aberrations						
0		$w_{911}h^9\rho \cos \varphi$	$w_{822}h^8\rho^2 \cos^2 \varphi$	$w_{733}h^7\rho^3 \cos^3 \varphi$	$w_{644}h^6\rho^4 \cos^4 \varphi$	$w_{555}h^5\rho^5 \cos^5 \varphi$
2	$w_{820}h^8\rho^2$	$w_{731}h^7\rho^3 \cos \varphi$	$w_{642}h^6\rho^4 \cos^2 \varphi$	$w_{553}h^5\rho^5 \cos^3 \varphi$	$w_{464}h^4\rho^6 \cos^4 \varphi$	
4	$w_{640}h^6\rho^4$	$w_{551}h^5\rho^5 \cos \varphi$	$w_{462}h^4\rho^6 \cos^2 \varphi$	$w_{373}h^3\rho^7 \cos^3 \varphi$		
6	$w_{460}h^4\rho^6$	$w_{371}h^3\rho^7 \cos \varphi$	$w_{282}h^2\rho^8 \cos^2 \varphi$			
8	$w_{280}h^2\rho^8$	$w_{191}h\rho^9 \cos \varphi$				
10	$w_{0100}\rho^{10}$					

Table II: ISO versus Born & Wolf nomenclature

No.	ORDER		Zernikes	
	Born & Wolf	ISO	Born & Wolf	ISO
0	0	0	Z_0^0	Z_0^0
1	1	2	Z_1^{-1}	Z_1^1
2	1	2	Z_1^1	Z_1^{-1}
3	2	2	Z_2^{-2}	Z_2^0
4	2	4	Z_2^0	Z_2^2
5	2	4	Z_2^2	Z_2^{-2}
6	3	4	Z_3^{-3}	Z_3^1
7	3	4	Z_3^{-1}	Z_3^{-1}
8	3	4	Z_3^1	Z_4^0
...	3	...	Z_3^3	...
	

Grouping like terms of Zernikes, which are contributing, for the tilt can be equated to the fifth order field independent wave aberration is given by Equation 4.11. Using the trigonometric relation given by equation 4.12, we can rewrite

$$W_{511}\rho \cos \varphi = [Z_1 - 2Z_6 + 3Z_{13}] \rho \cos \theta + [Z_2 - 2Z_7 + 3Z_{14}] \rho \sin \theta \quad (4.11)$$

$$a \cos \beta + b \sin \beta = \sqrt{a^2 + b^2} \cos \left[\beta - \tan^{-1} \left(\frac{b}{a} \right) \right] \quad (4.12)$$

Equation 4.11 as

$$W_{511}\rho \cos \varphi = \rho \sqrt{(Z_1 - 2Z_6 + 3Z_{13})^2 + (Z_2 - 2Z_7 + 3Z_{14})^2} \cos \left[\theta - \tan^{-1} \left(\frac{Z_2 - 2Z_7 + 3Z_{14}}{Z_1 - 2Z_6 + 3Z_{13}} \right) \right] \quad (4.13)$$

Furthermore, the relation between Zernike aberration coefficients to power series aberration coefficients is discussed in reference 49.

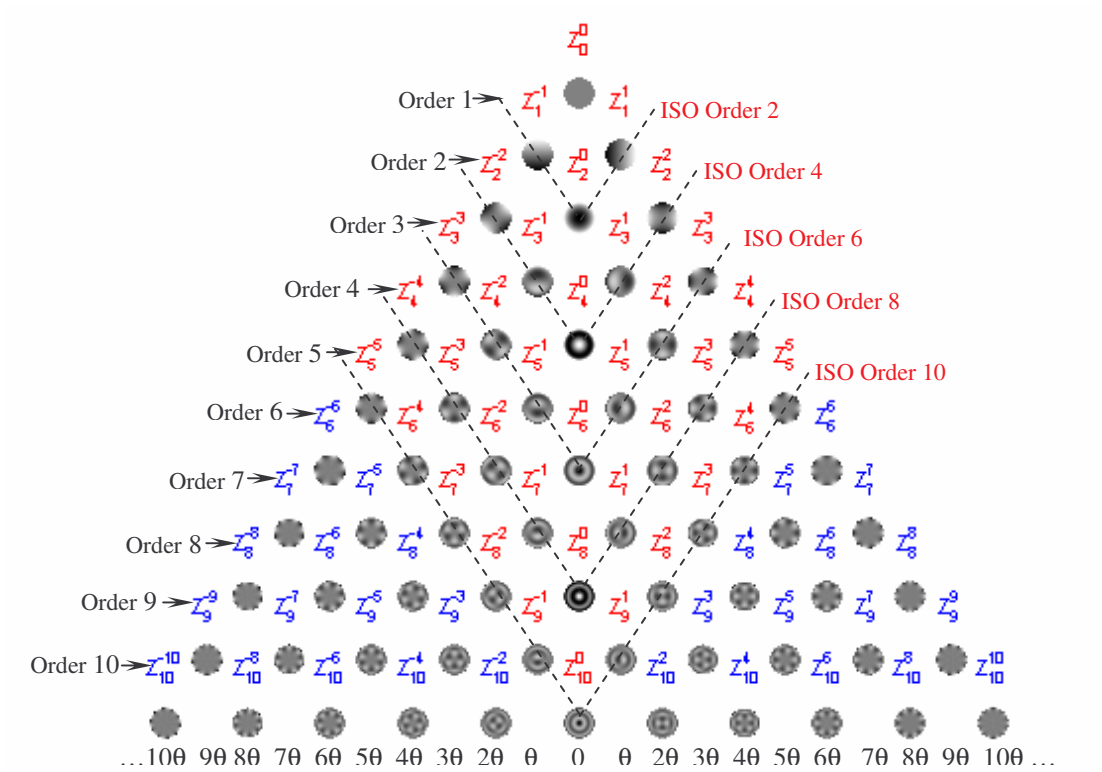


Figure 4.10 The Zernike polynomials. ISO represents the V shaped dotted line. Born & wolf represents the horizontal as indicated by an arrow. Numbering follows Table II

5. INTERFEROMETRIC MICRO-ASPHERIC LENS MEASUREMENT SIMULATION

In order to subtract the intended shape from a micro-lens measurement and assess the uncertainty, we have to understand the consequences of misalignment during the measurement. Misalignment errors can be significant and difficult to assess in an interferometric PSI measurement of a micro aspheric surface. We have developed a simulation package [50] in Matlab® which allows us to input an arbitrary surface, misalign the surface relative to a fixed coordinate system, and then calculate the optical path difference (OPD) that results. The OPD is the wavefront distortion (section 4.3) that results when a spherical optical wave reflects from the surface. The simulation shows that aberrations appear in the measurement that does not capture the shape of the lens surface if the part is misaligned. Thus, these are a systematic bias in the measurement. Further, these aberrations depend significantly on the aspheric details of the surface.

We have compared our simulation with experiment. Systematic misalignment biases are clearly present in the measurement, but in this case, misalignment also leads to retrace errors, which add additional biases to the measurement [51, 52]. The return beams passing through the optical system do not follow the same path leads to the retrace errors. Therefore, retrace errors are specific to an instrument's optical design (much of which is proprietary) and are not easily incorporated into simulation.

5.1 Interferometric simulation code

An interferometric measurement of a spherical test lens consists of focusing a coherent spherical wavefront toward the center of curvature of the test lens. If the test lens is perfect and its center coincides with the focus of the beam, the wavefront reflects

back on itself, interferes with an internal reference wavefront, and is said to be ‘null’. ‘Null’ means that the detector array will record a uniform intensity over the aperture of the test lens. The map of the phase difference between the reflected wave and the reference wave is called the OPD map. If the test lens is imperfect, the reflected wavefront will be advanced or delayed in different regions and the resulting OPD map will not be constant and will capture the test lens errors. If the test lens is intentionally aspheric (nonspherical), then it is not possible to ‘null’ the cavity.

The simulation code (APPENDIX C) we have developed models the generation of an optical path difference as twice the difference between a spherical reference surface and the test lens surface. The basic geometry is shown in Figure 5.1. The OPD is always calculated as the radial difference between a reference sphere and the surface of

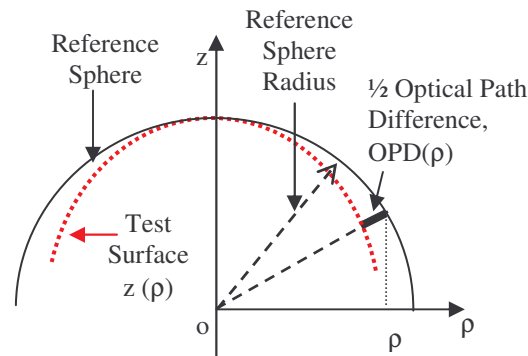


Figure 5.1: Schematic of the geometry used to simulate the calculation of the OPD (ρ). See text for details.

the test lens. The reference sphere is chosen to have a radius such that the apex of the test lens is tangent to the reference sphere on axis without misalignments. No misalignment means that the reference sphere radius matches the base radius of curvature of the test lens. The reference sphere defines the global coordinate system. For every coordinate ρ , the OPD (ρ) is taken to be two times the distance between the reference sphere and the

test surface along the reference sphere radius at the coordinate ρ , as shown. Rather than consider the detailed OPD resulting from specular reflection, we use the approximation that a ray in the wavefront will reflect exactly back on itself after reflecting from the surface. This approximation is valid for mild aspheric surfaces and small misalignments. Our simulation is very general and allows us to input an arbitrary shape for the test lens. We start with the well-known rotationally symmetric equation for a general convex lens, which is defined by equation 2.9. This equation is commonly used to define aspheric lenses, because pure conic surfaces are easily described (defined by a particular conic value, K , with all A_i terms set to zero), or arbitrary aspheres can be defined by using the A_i terms. Additionally, we can add arbitrary surface errors to a nominal starting surface.

Misalignment means that the test lens center of curvature does not coincide with the center of the reference sphere. In a realistic interferometric test it is mechanically impossible to perfectly position the test lens and perfectly ‘null’ the cavity, therefore misalignment is always present. This is particularly the case in high-speed automated testing of micro-lenses, where time spent repositioning the test lens to improve the cavity null can be a significant contribution to the test time of an entire wafer which can consist of thousands of micro-aspheric lenses.

The OPD map in the presence of misalignment is calculated by first determining the appropriate reference sphere. The misalignment along the z -axis is added first, and a new reference sphere is chosen to maintain the condition that the test lens surface and reference sphere are tangent on axis. Next, a general three dimension coordinate transformation is performed to simulate an arbitrary x/y translation and/or rotation. In

practice, only translation misalignment is significant in an interferometer therefore we have accordingly restricted our analysis. The geometry used to calculate the OPD with misalignment is illustrating in Figure 5.2.

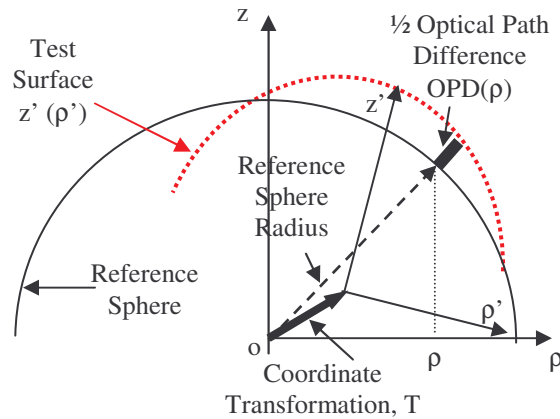


Figure 5.2: Schematic of the geometry used to simulate the calculation of the $OPD(\rho)$ when the test lens is allowed to be misaligned.

5.2 Simulation results for misalignment

Simulation results for an interferometric measurement of a micro-aspheric lens are shown in Figure 5.3. The OPD maps have been converted to interferograms, so the fringe pattern can be appreciated. The series of interferograms shows the results for various translation misalignment conditions. The micro-lens was taken to have a base radius of curvature of $650\ \mu\text{m}$, a geometric numerical aperture of 0.707, a conic constant of zero, and an aspheric deformation constant, A_1 , of $-3 \times 10^{-9}\ \text{m}$. Each OPD map is also fit the set of Zernike polynomials shown in Figure 4.10. Misalignment primarily leads to tip, tilt and defocus in the OPD map (Z_1^{-1} , Z_1^1 and the Z_2^0), and these terms can be easily removed from the OPD map. Because the exact misalignment cannot be known from the experiment, these low order Zernike coefficients are the only thing that can be used to

assess the degree of misalignment. These terms are responsible for the prominent straight fringes and bulls-eye fringes observed in the interferograms in Figure 5.3.

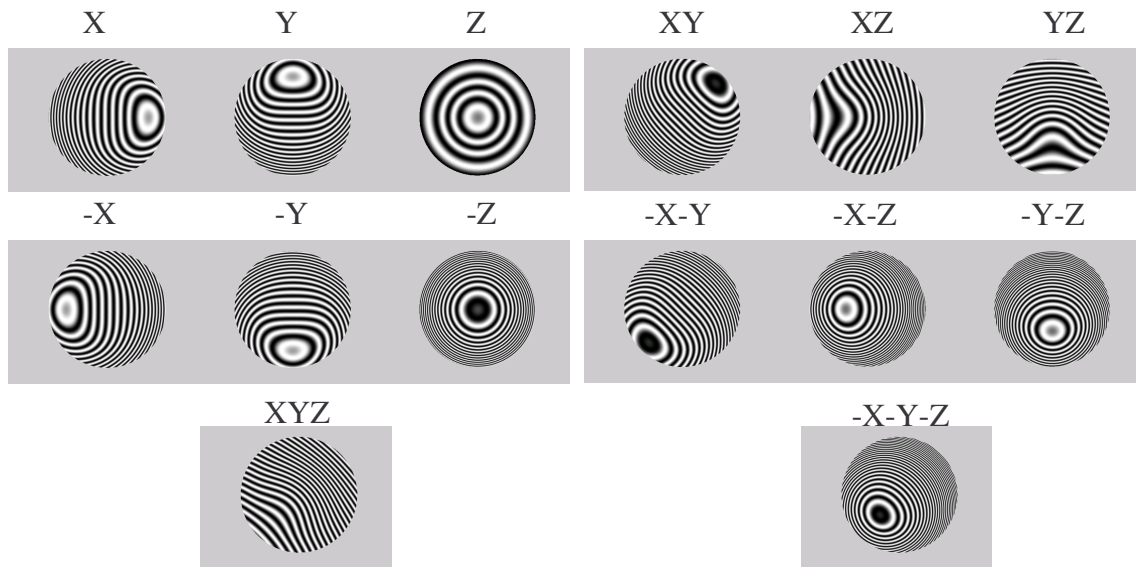


Figure 5.3: Simulated interferograms of an interferometric measurement of a $480\mu\text{m}$ diameter and $650\mu\text{m}$ radius of curvature micro-lens. Various XYZ misalignment conditions are shown.

Beyond these first order effects however, misalignment also impacts the higher order aberrations. This means that when the measurement result is fit with the set of Zernike polynomials (see Figure 4.10), the Zernike coefficients of the higher order polynomials change with misalignment. This is a pure geometric effect – the simple consequence of subtracting an aspheric surface from a spherical surface with misalignment. For a rotationally symmetric aspheric lens, the dominant misalignment aberrations are coma with XY translation and spherical aberration with Z translation.

As the part is misaligned, these aberrations increase approximately linearly with misalignment, and the slope is sensitive to the aspheric nature of the lens. Simulated misalignment sensitivity data is shown in Figure 5.4. The part is misaligned independently in the X , Y , and Z directions to avoid cross-correlations. Part (a) shows

the dependence of coma with X-axis misalignment, and part (b) shows the dependence of low-order spherical aberration with Z-axis misalignment. The offset for these curves has been set to zero so the slopes can be easily compared. In general the offset is very

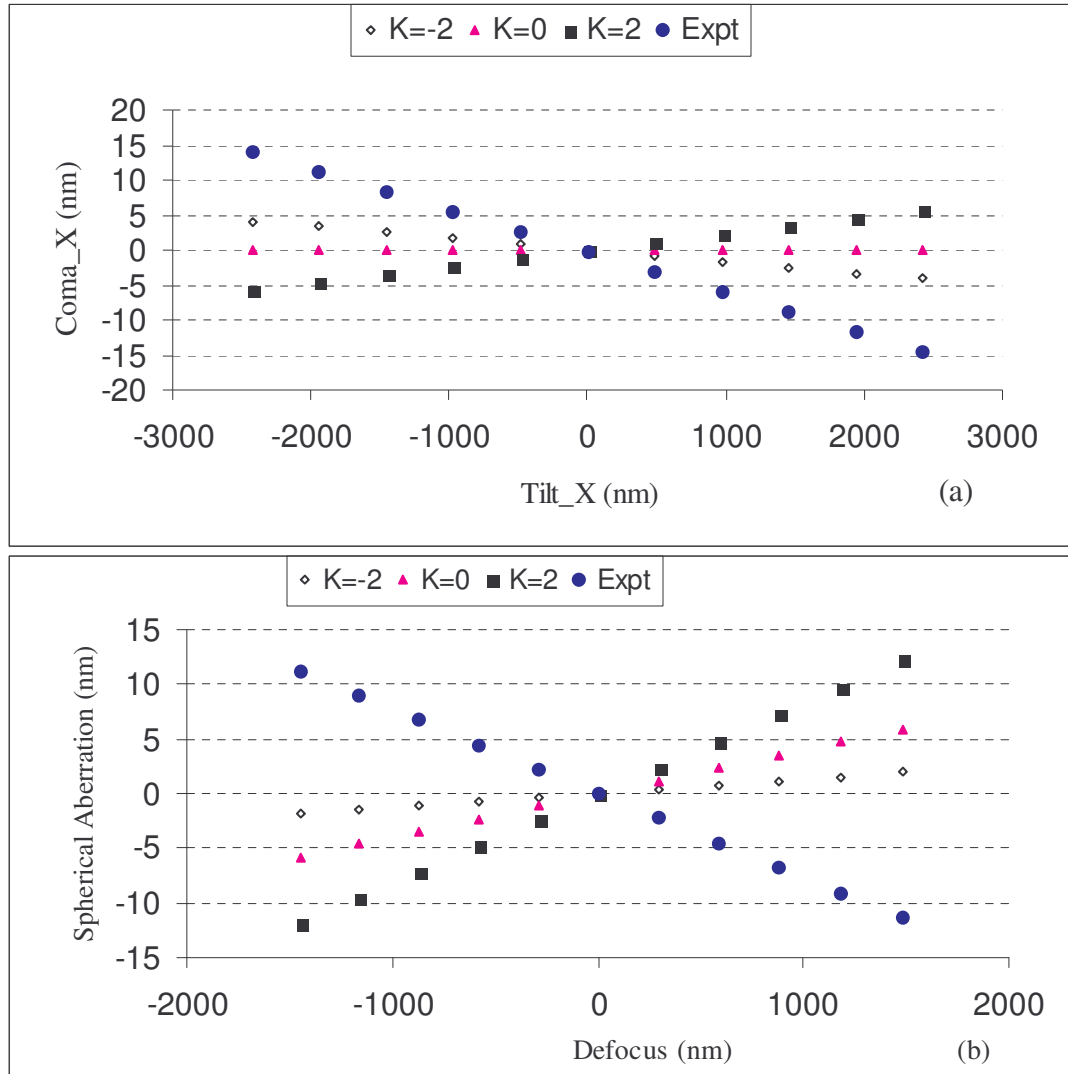


Figure 5.4: (a) Coma dependence on X misalignment. (b) Spherical aberration dependence on Z misalignment. Misalignment sensitivity simulations were run for the XZ misalignment of a micro lens with a $480\mu\text{m}$ diameter and $650\mu\text{m}$ radius of curvature. The X and Z positions of the test lens are systematically and independently varied, and the Zernike coefficients correlating the misalignment coefficients to the low order aberration coefficients are plotted. Similar experimental misalignment data was taken on a FISBA μ phase interferometer on a lens with a similar geometry and this is shown in the plots.

sensitive to imperfections in the interferometer and will not be zero. The offset for spherical aberration vs. Z-misalignment will certainly be non-zero for an aspheric test lens. As shown in both plots of Figure 5.4, the slope is very sensitive to the value of the conic constant. The misalignment for a spherical part is shown in both plots. To the level of approximation in our simulation, the coma dependence of XY translation misalignment for a sphere has a slope of zero, but the slope is non-zero for any aspheric surface. All surfaces (spheres and aspheric) show a misalignment sensitivity of spherical aberration with defocus misalignment (Z-axis misalignment). Since it is not possible to completely null an interferometer, the misalignment will add errors to the measurement. It may be possible to correct these errors in the experiment with knowledge of the alignment sensitivity characteristics of the interferometer. The deviation of spherical aberration of aspheric from the sphere is the actual spherical aberration contributed by asphericity of the lens. At the very least, the simulation shows that the misalignment will certainly impact the uncertainty of the measurement.

5.3 Misalignment in experiment versus simulation

We performed an alignment sensitivity test on a commercial micro-interferometer to compare to our simulation results. In an alignment sensitivity test, we acquire a series of interferometric measurements as we systematically misalign the test lens in the X, Y, and Z directions. The interferometer has the ability to measure the radius of curvature of the lens and this was found to be 650 μm . The numerical aperture condition of the measurement, once a software mask had been defined was 0.707. Note that these parameters match the parameters used for the simulation. However, the aspheric details of the test lens are unknown; therefore a deformation constant, A_1 , of $-3 \times 10^{-9} \text{m}$ was

chosen for the simulation as an illustration. Sample interferograms from the measurements are shown in Figure 5.5. As is done in the simulation, the part is misaligned independently in the X, Y, and Z directions to avoid cross-correlations.

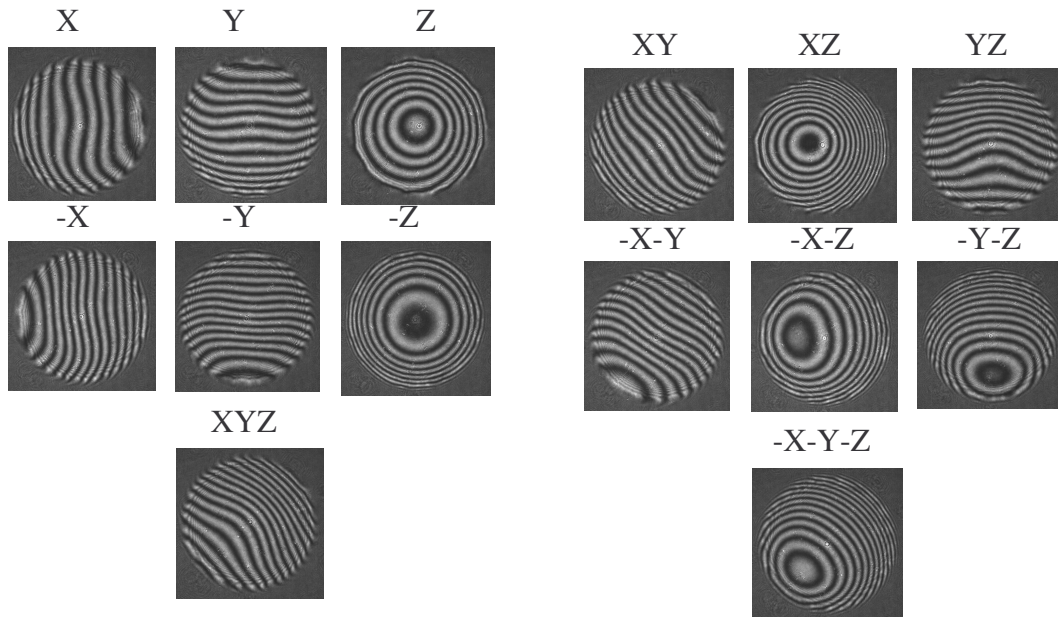


Figure 5.5: Measured interferograms of an interferometric measurement of a 480 μm diameter and 650 μm radius of curvature micro-lens. Various XYZ misalignment conditions are shown.

We have generated alignment sensitivity curves similar to the curves in Figure 5.4 by fitting the experimental measurements to the set of Zernike polynomials. This data is plotted in Figure 5.4, as well. Since we focus on the slope comparison, we subtracted the offset from the experimental curves.

The experiment shows a very strong increase in aberration with misalignment a dependence that is quite different from the simulation. Similar effects have been observed in misalignment studies of a spherical part measured in a large aperture commercial interferometer [51]. In this case, the departure from the expected dependence was attributed to retrace errors in the optics in the imaging path of the interferometer.

These authors found that the experimental slope of spherical aberration versus defocus curve was more than 100 times greater than predicted by a simple calculation (similar to our simulation).

In our experiment, the difference between experimental slope and simulation slope is significant, but much less than the factor of 100 previously reported. Undoubtedly retrace errors are contributing to our measurement and impacting the slope of the alignment sensitivity curves, as well, but our simulation shows that the asphericity has a comparable contribution.

In a real measurement, the asphericity is not known, therefore one does not rigorously know which slope to use to correct for the misalignment and estimate a measurement uncertainty. As a part of our new analysis strategy, we developed an approximate way of solving this, which will be described in the next three chapters.

6. EXTRACTING THE ASPHERIC MICRO LENS SURFACE PROFILE FROM THE MEASUREMENT

In order to extract the best-fit conic constant (Chapter 7) or analyze the surface errors (Chapter 9), we need to generate the surface profile from the measurement data. The first task is to obtain as much information as we can to generate the “actual” surface profile of a micro lens from our measurement. The techniques we applied are the phase shifting interferometry (PSI) technique, and the scanning white light interferometry (SWLI) technique. These techniques are described in Chapter 3. We are going to start with SWLI technique to describe how to get the surface measurement data and the determination of uncertainty parameters. Then we will describe how to obtain surface measurement data based on PSI technique and its uncertainty parameter determination. We also describe the basic idea to generate surface profiles from OPD measurements. All we discussed in this chapter is a base for subsequent chapters that deals with extracting best fits, subtracting design shapes and residual analysis. In revisiting section 2.2, we relate the parameters of a general aspheric to our aspheric micro lens measurement. Equation 6.1 describes a rotationally symmetric convex aspheric lens [53]. Where Z is the surface height, ρ is the aperture radius, the A_i s are deformation constants, R is the base radius of curvature, and K is the conic constant. The conic constant determines the base conic surface of the aspheric surface. For example, if $K=0$ the base conic surface is a sphere (see Figure 6.1). Most micro lenses are designed to be exact conic surfaces, where the A_i deformation constants are zero. This is because perfect collimating functionality is possible with a single refractive surface that is a conic of revolution with a conic constant that is equal to the difference in the refractive index on either side of the interface. In a SWLI measurement, Z represents the measured surface height profile, and in PSI measurement,

it represents extracted surface profile. Based on Equation 6.1, the origin of the xyz coordinate is at the apex of the lens. We translate this point in z down to the substrate of a lens to define it as the center of the lens (see Figure 6.1). Therefore, we define sag as the distance measured from the origin (center) along the z -axis as a function of ρ where

$$\rho = \sqrt{x^2 + y^2}$$

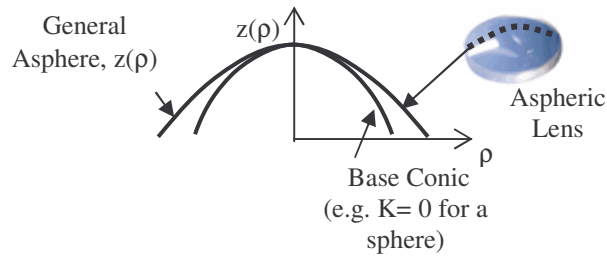


Figure 6.1: A general aspheric surface with its base conic.

$$Z(K, \rho, R, A_i) = \frac{-\frac{\rho^2}{R}}{1 + \sqrt{1 - (1+K)\frac{\rho^2}{R^2}}} - A_1\rho^4 - A_2\rho^6 - \dots \quad (6.1)$$

6.1 SWLI measurement data and determination of uncertainty parameters

Data is taken in two ways, a single measurement at the apex of the lens and a measurement using the stitching capability of the instrument. A SWLI instrument is limited in the surface slopes that can be measured. If the slope is too high, light does not reflect back into the objective. A stitching procedure is usually available on the instrument whereby a higher NA objective can be used which captures steeper slopes, and smaller area images are then taken as the lens is translated under the objective. The sub-images are stitched together, resulting in the measurement of a larger fraction of the lens surface. We refer to the measurements as not stitched and stitched data. In our case,

we used the same objective for both the stitched and not stitched measurements to avoid additional bias differences between the two from the aberrations introduced by the objective. We took eleven measurement of each type. We place the lens at different

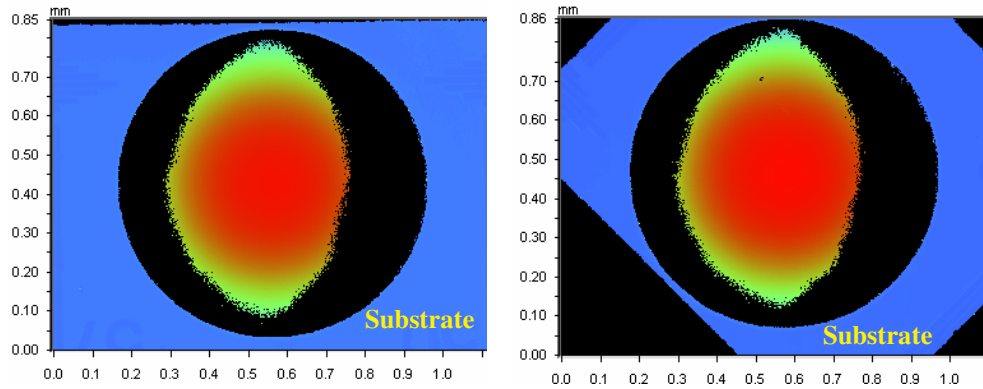


Figure 6.2: Stitched data at different orientations of the aspheric micro-refractive lens.

orientations during measurements. An example of two different orientations of the stitched data is shown in Figure 6.2. Orientation change between measurements will introduce reproducibility errors and allow this contribution to the uncertainty to be assessed. At the beginning of each measurement, we “null” the substrate to align the optical axis of the lens (defined as the normal to the plane of the substrate) to the axis of the SWLI. We further correct for the residual tip and tilt using Vision[®] 32. First, we open the measurement data in Vision, and then mask it so that we can only see the substrate data. Fitting the substrate data to Zernike polynomials, we get the tip and tilt Zernike coefficients. Then we generate an OPD map from the tip and tilt information. Finally, subtract the generated map from the raw data to get the final corrected measurement data used for analysis. This general procedure of correcting the measurement data is shown in Figure 6.3.

The lens is measured with a NewView™ 5000 (Zygo Corporation) using a 10x Mirau interferometric objective. We used a spatial sampling of $2.2\ \mu\text{m}$ (320x240) for stitched measurement, and a spatial sampling of $1.1\ \mu\text{m}$ (640x480) for not stitched

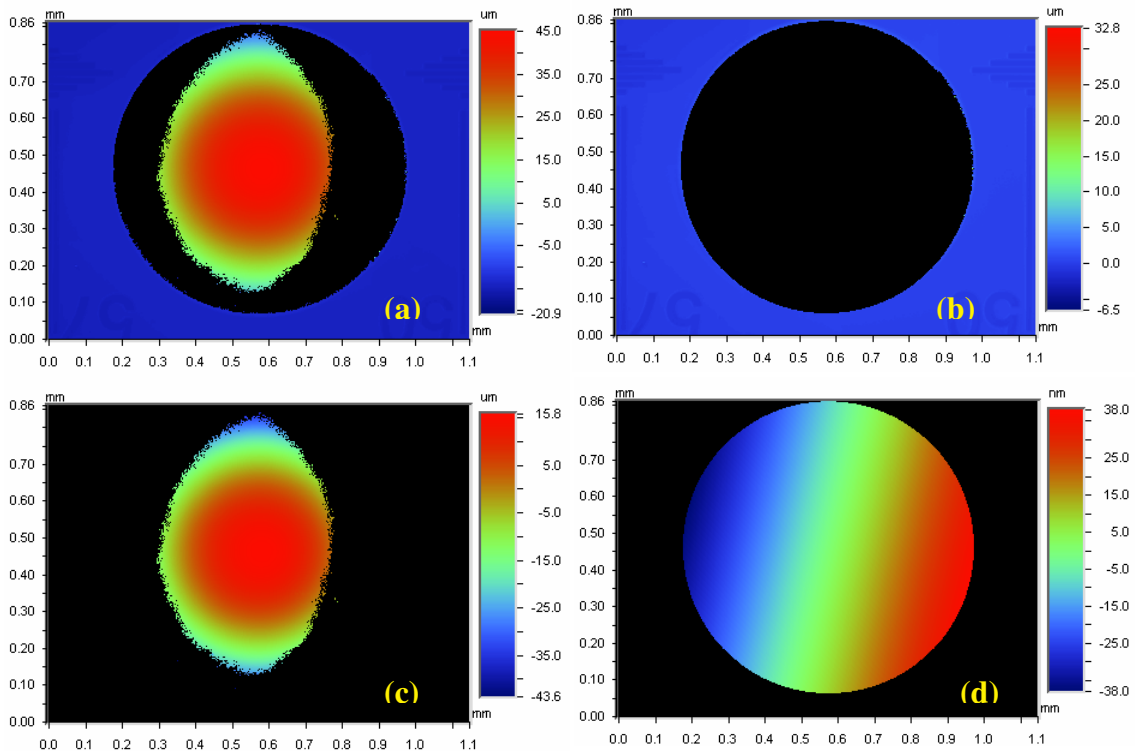


Figure 6.3: Preparing the data for analysis: (a) raw data (b) substrate data only (c) corrected map from tip/tilt information of substrate (d) data

measurement. We used a system magnification of two for both stitched and not stitched measurements. Since the spatial sampling is related to the camera resolution, the apparent pixel size of the measurements as read from the calibrated instrument, are $1.103\ \mu\text{m}$ and $0.551\ \mu\text{m}$ for stitched and not stitched, respectively.

6.1.1 Estimating the conic surface parameters

In order to carry out the least-square minimization process to determine the best-fit conic value, we estimate four parameters from the measurement. These parameters,

along with a conic value, uniquely define a conic surface. The four parameters are a base radius of curvature, the sag of the lens, the lens aperture, and the lens center position. Only the conic value is varied in the chi-square minimization. The uncertainty for each of the four parameters is also estimated so that the Monte Carlo analysis can be carried out to assess a combined uncertainty for the best-fit conic value. The values of these parameters and their uncertainties are estimated as follows.

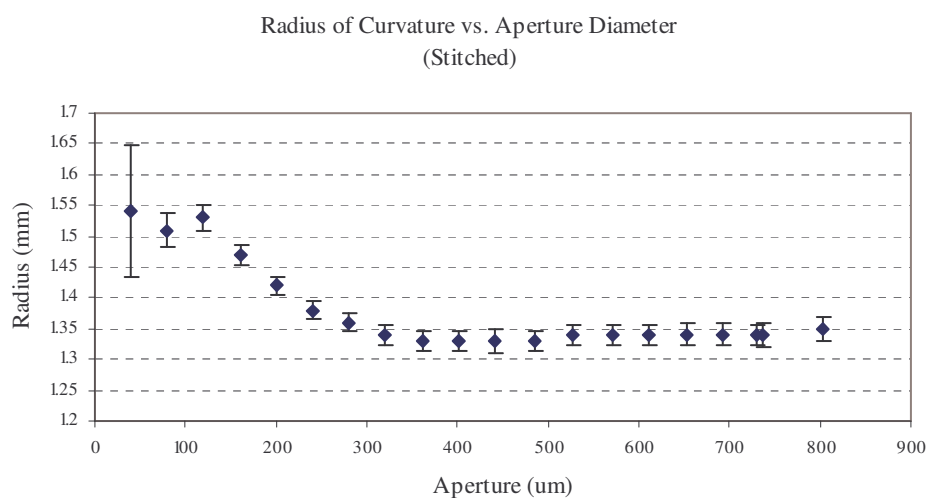


Figure 6.4: Best sphere fit radius versus aperture (unmasked data).

The first value to be determined is the base radius of curvature of the lens. Mathematically, the base radius of the conic surface is the same as the radius of curvature at the vertex of the lens (this is the sphere for $K=0$). To translate this definition to our case, we masked down our corrected measurement data incrementally to a level of 5% of the lens surface about the apex. For example, the stitched data was masked down starting from 100% to 5% at a step of 5%. Each of the masked images is fit to the best-fit sphere using Vision[®] 32 to get the radius. The base radius should be the radius fit to the

data, in the limit that aperture size goes to zero. The masking and fitting procedure was done for all eleven measurements. The mean and standard deviation (one sigma) of all the measurements at each masked condition is also calculated. By doing this we can see the spread in the radius values. This is summarized in the radius versus aperture graph shown in Figure 6.4. The analysis shows that the radius increases below an aperture size of approximately $300\ \mu\text{m}$. The definition of the base radius would lead one to estimate a base radius of perhaps $1.5\ \text{mm}$ from this analysis. However, by generating simulated measurement data and carrying out the same procedure, we found that the radius values for small apertures are extremely sensitive to noise in the data. From this analysis, we determined that radius values below an aperture size of approximately $300\ \mu\text{m}$ are suspect. Therefore, we took the base radius values at an aperture of $300\ \mu\text{m}$, giving us a radius of $1.36\ \text{mm}$ for the stitched measurements and $1.37\ \text{mm}$ for the not stitched measurements. We estimate an uncertainty in the base radius of approximately $20\ \mu\text{m}$, which is the standard deviation value from the group of eleven measurements. Likely the uncertainty should be larger than this to include the uncertainty in our choice of the appropriate aperture size to use for the estimate. This will be considered in future work.

The second step is to determine the sag from the measurement. We take only the data from the lens part of the image to generate our height profile. Because the SWLI cannot measure the steepest part of the lens surface, the data is not continuous from the apex to the aperture edge (see Figure 6.2). We therefore must estimate the height of the lens above the substrate. This is the sag of the lens. This height is directly estimated from the measurement data. Variations in sag are due to noise in the measurement and the choice of the number of data points at the lens apex used for the estimation. We estimate an

average value of $57.7 \mu\text{m}$ for both the stitched and the not stitched, and an uncertainty of $0.7\mu\text{m}$ for stitched and $0.6\mu\text{m}$ for not stitched.

The aperture of the micro lens is the third parameter to be estimated. This is also estimated directly from the measurements. Because data is not present around the edge of the lens, we cannot directly see the lens aperture. We must therefore make an assumption about the lens edge location. We assume that the lens surface meets the substrate plane where the data drop out occurs in the measurements (see Figure 6.3). We choose a circular mask to fit the aperture and use the diameter of this mask as our estimate. In doing this for all measurements, we find a mean aperture diameter value of $800\mu\text{m}$ for both stitched and not stitched and uncertainties of $2.42 \mu\text{m}$ and $2.86 \mu\text{m}$ for stitched and not stitched data, respectively.

The fourth parameter is the x/y location of the lens, which we define as the lens center. This depends directly on the method we choose to find the aperture diameter. We define the center as the mid point of the circular mask used to estimate the aperture diameter. Since we assign the center of the circular aperture to be zero, the mean value of the center from the measurement data is zero with uncertainty estimates of $0.63 \mu\text{m}$ and $0.59 \mu\text{m}$ for stitched and not stitched data, respectively. Uncertainties in the aperture diameter and the center location are dominated by the discreteness from the finite pixel size.

The instrument calibration for the x, y (in the plane of the lens' substrate), and z coordinates (normal to the lens' substrate) is also a potential source of uncertainty. The calibration uncertainties however are a small contribution to those that we consider. For example, the calibration uncertainty for the z values is $\pm 0.26\%$. Therefore, for an

estimated 57.7 μm sag value, the uncertainty due to calibration is 0.1 μm . We estimate an uncertainty in the sag due to the noise in the measurements of 0.7 μm . Therefore, the calibration uncertainty can be ignored.

6.2 Phase shifting interferometry measurement

The second approach to get the surface profile of aspheric micro-refractive lens is based on OPD measurement of the phase shifting interferometry (PSI) technique, which is explained in section 3.2. We used FISBA OPTIK $\mu\text{phase}^{\text{®}}$ interferometer shown in

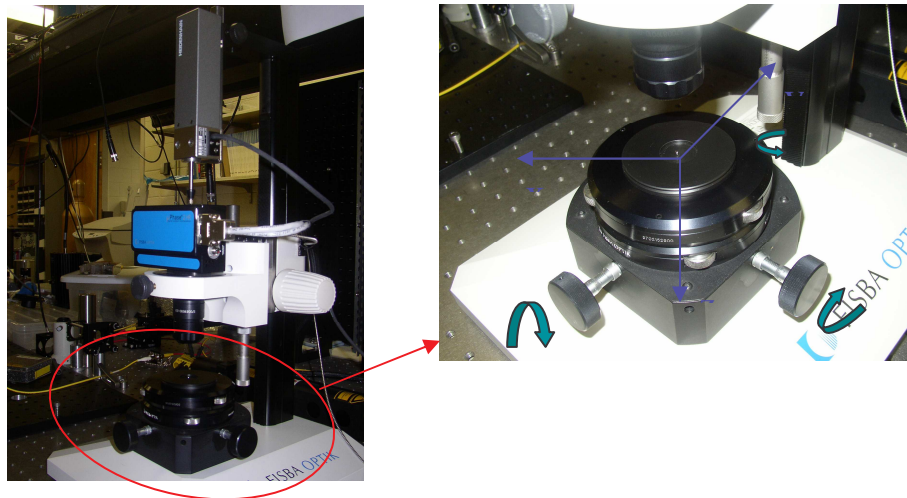


Figure 6.5: FISBA OPTIK $\mu\text{phase}^{\text{®}}$ interferometer. It is used to measure an aspheric micro lens to get an OPD map. Misalignment sensitivity measurements (Chapter 5) are also done as an aspheric micro lens is translated to X Y and Z (shown to the right)

Figure 6.5. This interferometer uses a He Ne laser source with a Twyman Green set up. In order to measure our aspheric micro lens, we used an objective with a numerical aperture of 0.34. At the beginning of each measurement, we “null” at the confocal (discussed in section 6.2.2) position. Normally it does not give us the surface profile measurement directly as New ViewTM 5000 (SWLI). Instead, it gives us the OPD map, which can be converted to height (surface) profile. We also used this same interferometer

for misalignment measurements discussed in chapter 5. As shown in the right side of Figure 6.5, the x , y , and z axis as the coordinate of the translation motion of a part (micro lens). In this section, we focused on how to extract surface profile from OPD measurement, and estimate the conic surface parameters of our aspheric micro lens.

6.2.1 Extracting surface profile from OPD map

Based on our assumption of OPD analysis, the difference between the reference sphere with the test surface along the radius of the reference sphere is an OPD (See

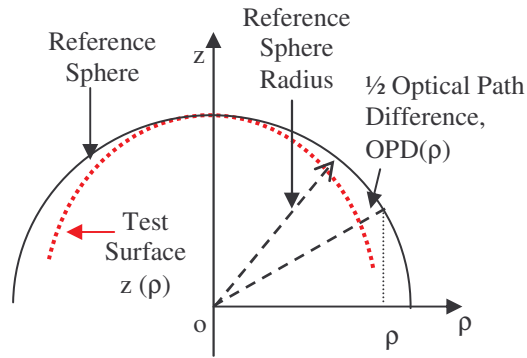


Figure 6.6: the optical path difference along the radial direction, $\rho^2 = X^2 + Y^2$

Figure 6.6). Mathematically, it can be expressed as equation 6.2. Z_{Ref} and Z_{sag} are the surface height of the reference sphere and the test surface respectively. X , Y , and Z are the

$$OPD = \sqrt{X^2 + Y^2 + Z_{Ref}^2} - \sqrt{x^2 + y^2 + Z_{sag}^2}$$

where $x = X \pm \delta x$ & $y = Y \pm \delta y$ & $Z_{Ref} = R \pm \delta z$ (6.2)

$$R = \sqrt{X^2 + Y^2 + Z_{Ref}^2}$$

global coordinates which are used to define the reference sphere. To simplify the expression let's assume there is no misalignment ($\delta x = 0$, $\delta y = 0$, and $\delta z = 0$). In this case, the expression is simplified and easily solved to give the surface profile of equation 6.3.

$$Z_{sag} = R - OPD \tag{6.3}$$

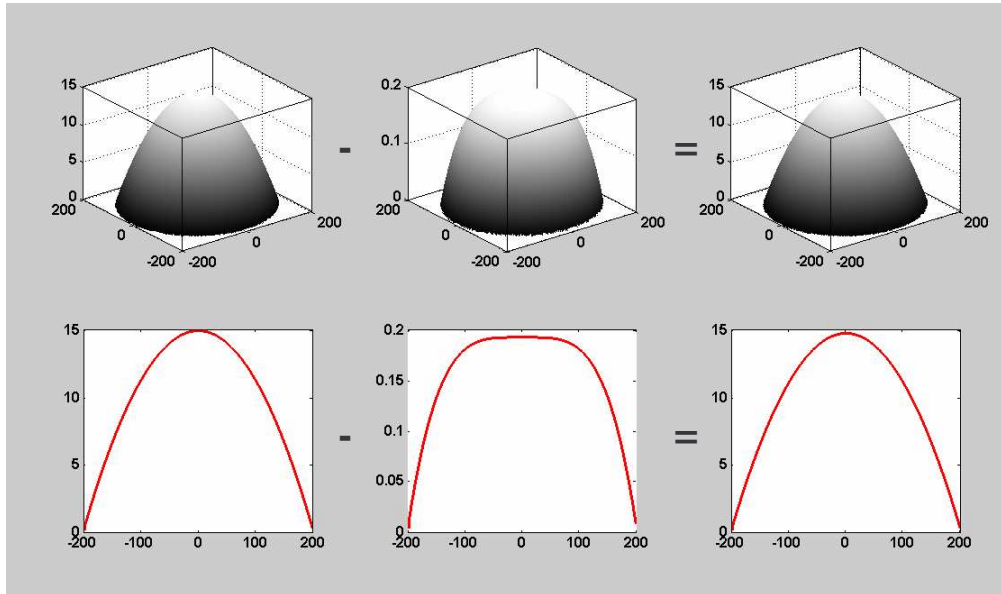


Figure 6.7 Extracting a surface profile based on an OPD map with no misalignment and the radius of curvature of the lens. A sphere, an OPD, and extracted surface are shown from left to right. All units are in μm

This Equation can be visualized as shown in Figure 6.7. It shows the extracted surface (right), the sphere (left) of radius $1366 \mu\text{m}$, and OPD map (middle). This simple example shows us that all we need is the radius of curvature of our lens to reproduce its surface profile since we have our OPD map from the measurement. This is the general idea we followed to generate our surface profile. However, the details on how to measure the radius of curvature and how to deal with the misalignment issues will be addressed in the coming sections.

6.2.2. Estimating the conic surface parameters and uncertainty

In order to generate the surface height profile of our aspheric micro lens, we need to estimate the best-fit radius and the aperture of the lens. In estimating these parameters, we discussed the associated uncertainties and the misalignment uncertainty. The first value to be determined is the best-fit radius of the lens. We used FISBA OPTIK $\mu\text{phase}^{\text{®}}$ interferometer for the measurement of the best-fit radius of our aspheric micro lens. As

shown in Figure 6.8, we can determine the radius of curvature of the aspheric micro-refractive lens by placing it at confocal and cat's eye positions. First, we set the encoder

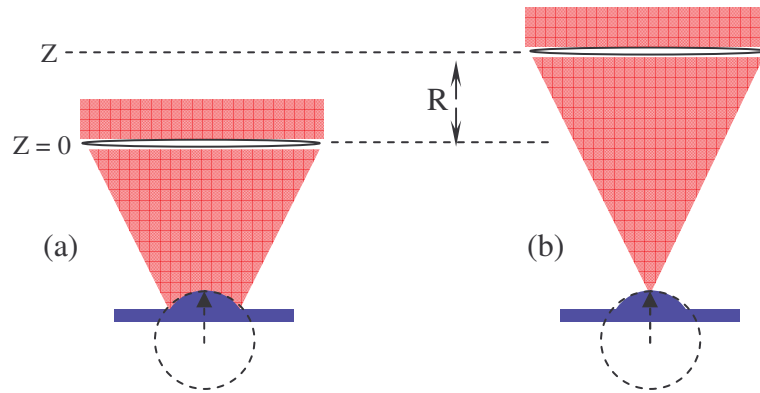


Figure 6.8: (a) Confocal and (b) Cat's eye positions to measure radius of curvature R .

to zero at the confocal position. As the micro lens is moved along the optical axis to the cat's eye position, the encoder records the vertical (z) distance. Note that as the Figure 6.8 tells us that the objective is moving relative to the micro lens to find the two positions. The difference between the two positions is normally the best-fit radius of curvature of the aspheric micro lens. Since we cannot perfectly null at confocal and not knowing the exact position of cat's eye, we had to follow additional methods to determine these exact positions (or minimize errors). The method we followed to minimize position errors is what we called misalignment sensitivity measurement. We applied misalignment sensitivity measurement method on both confocal and cat's eye positions. We measured our aspheric micro lens at confocal position to get the OPD map from which we fit to Zernike polynomials and get all Zernike coefficients. At the same time, we record the z position. Then we did the same thing on additional eight Z positions (four on either side of the confocal position). We repeat the same procedure for the cat's eye position.

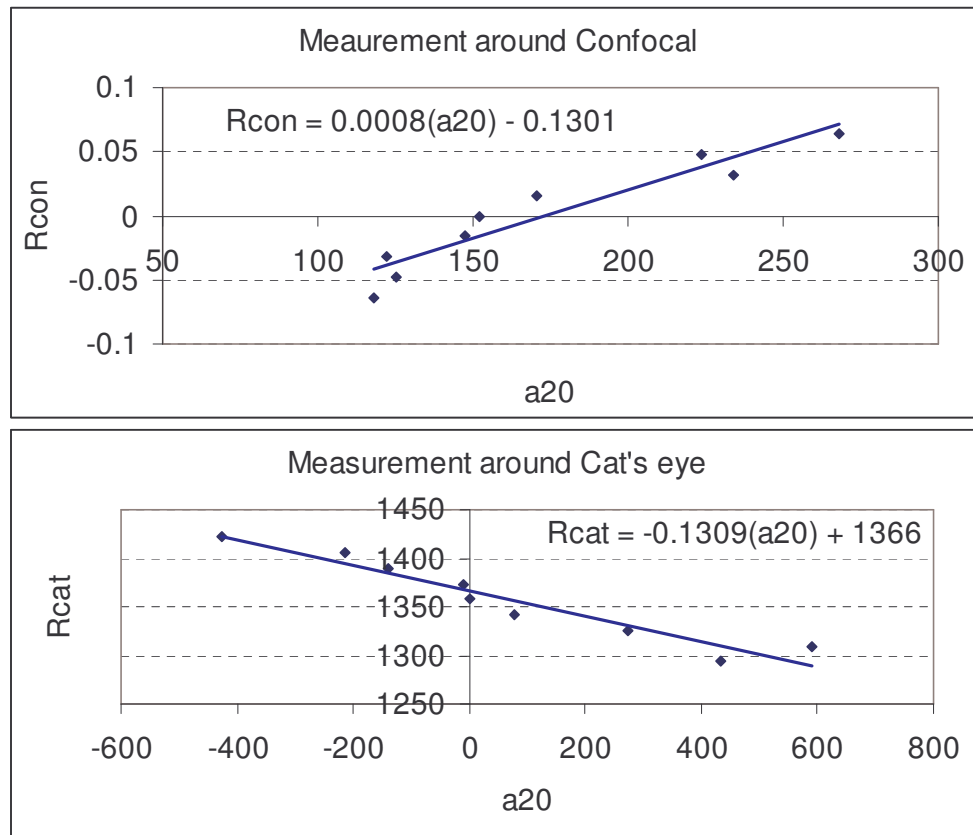


Figure 6.9: Heidenhain gauge reading around the Confocal and Cat's eye positions. The displacement readings (Z positions) at Confocal and Cat's eye are referred to as R_{con} and R_{cat} respectively. In both cases, the power Zernike coefficient is a_{20} . All the units are in μm .

Finally, we collect all the power terms from each measurement and corresponding Z positions and plot them. The plot is Z positions versus power term of the Zernike coefficient as shown in Figure 6.9. After linear fit, the difference between the Z intercepts ($a_{20} = 0$) of the two graphs gives us the best-fit radius of curvature of our aspheric micro lens. As it can be calculated from the graphs shown in Figure 6.9, the radius measured is $1366.1\mu\text{m}$. Note that the best-fit radius we found (by equating Zernike power term zero from the plot) is different from the base radius of the aspheric microlens. The base radius can be calculated after finding out the relationship between Zernikes and Siedel (primary) aberration. We described this relation in Chapter 4 and used it to find the

base radius of curvature in the best-fit conic constant analysis of Chapter 7. We found out that the base radius can be approximated by best-fit radius since the correction value is very small as compared to uncertainty of the best-fit radius. Now we can extract our aspheric micro lens surface profile since we have both R and OPD using simple equation of 6.3. However, there are associated uncertainties in determining the best-fit radius and getting the OPD. For example, there is a misalignment issue in getting all these measurement.

There are two ways to find the uncertainty in the best-fit radius measurement. One of them is ofcourse the spread (standard deviation, σ) from number of measurements. Another way is by extrapolating a measurement into number of measurements assuming a probability distribution. We followed the later. From our measurement, we found the uncertainty in slope and offset by a linear square fit method. As we described, the power Zernike terms were recorded in conjunction with the z positions to determine the best-fit radius of curvature. The linear equation of Z position as a function of power term is given by Equation 6.4.

$$Z = ma + Z_0 \quad (6.4)$$

Where m is the slope and Z_0 is the offset. Since numbers of readings were needed on and either side of the “null” position at cat’s eye and confocal positions, chi-square minimization is needed to use the linear square fit. The linear Equation 6.4 can be rewritten in the matrix form of Equation 6.5 [54]. Where the bar signs indicates average. The solution of m and Z_0 as it is solved directly from the matrix is given by equation 6.6.

$$\begin{pmatrix} \overline{a^2} & \overline{a} \\ \overline{a} & 1 \end{pmatrix} \begin{pmatrix} m \\ Z_0 \end{pmatrix} = \begin{pmatrix} \overline{aZ} \\ \overline{Z} \end{pmatrix} \quad (6.5)$$

$$m = \frac{B_{aZ}}{B_{aa}}$$

$$\text{where } B_{aZ} = \overline{aZ} - \overline{a}\overline{Z} \quad \text{and} \quad B_{aa} = \overline{a^2} - (\overline{a})^2$$

$$Z_0 = \overline{Z} - m\overline{a}$$
(6.6)

To get an estimate of the uncertainties in m and Z_0 , we use the relationship between the standard deviation of a function $f(m, Z)$, and the standard deviation of its variables m and

$$\sigma_f = \left(\frac{\partial f}{\partial m} \right) \sigma_m^2 + \left(\frac{\partial f}{\partial Z_0} \right) \sigma_{Z_0}^2$$
(6.7)

Z_i given by equation 6.6. In this case, errors in both m and Z_0 are caused by errors in Z_i .

Therefore, equation 6.7 can be rewritten as in equation 6.8.

$$\sigma^2(m) = (\Delta Z)^2 \sum_{i=1}^N \left(\frac{\partial m}{\partial Z_i} \right)^2$$

$$\sigma^2(Z_0) = (\Delta Z)^2 \sum_{i=1}^N \left(\frac{\partial Z_0}{\partial Z_i} \right)^2$$
(6.8)

After solving the partial derivatives and substitute them back to equation 6.8, the uncertainties in the slope and offset of the best-fit straight line is given by equation 6.9.

$$\sigma^2(m) = \frac{(\Delta Z)^2}{N} \frac{1}{B_{aa}}$$

$$\sigma^2(Z_0) = \frac{(\Delta Z)^2}{N} \frac{\overline{x^2}}{B_{aa}}$$
(6.9)

Since the best-fit radius of curvature is calculated from the difference of offsets of the two positions (cat's eye and confocal), one can use only the offset uncertainty. We used both parts of Equation 6.9, with Gaussian distribution equation to get values due to uncertainty. Therefore, the new slope and offset are found by adding these values to the slope and offset of the original values (see Equation 6.4). Based on this linear square fit method we extrapolated 100 radii measurements.

The second type of parameter, which causes uncertainty in the measurement, is the aperture. At “null” position of the measurement of confocal position, the aperture is related to the radius of curvature of the micro lens and the numerical aperture (NA). This

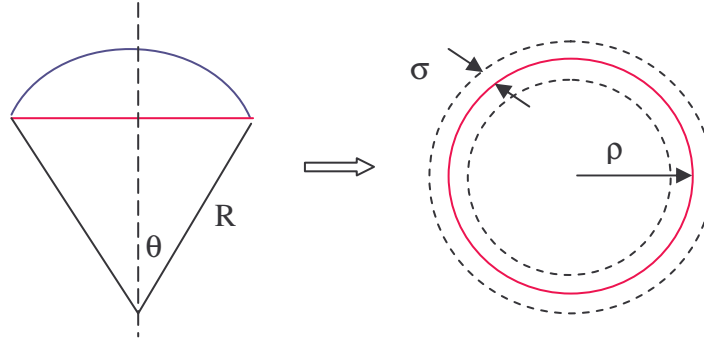


Figure: 6.10 Aperture radius ρ has uncertainty σ due to uncertainty in the radius (R) measurement and numerical aperture ($= \sin\theta$) used in the set up

relationship can easily be observed from Figure 6.10 and is given by Equation 6.10.

$$\rho = R \sin \theta \quad (6.10)$$

As it can be seen from the equation, the aperture is the function of θ and R. Therefore the uncertainty in the aperture can be rewritten as a form of Equation 6.7. The uncertainty in the aperture is given by equation 6.11[55].

$$\begin{aligned} \sigma_{\rho}^2 &= \left(\frac{\partial \rho}{\partial R}\right)^2 \sigma_R^2 + \left(\frac{\partial \rho}{\partial \theta}\right)^2 \sigma_{\theta}^2 \\ \sigma_{\rho}^2 &= (\sin^2 \theta) \sigma_R^2 + (\cos^2 \theta) \sigma_{\theta}^2 \end{aligned} \quad (6.11)$$

The third type of uncertainty is caused by the misalignment during the measurement. All the 15 measurements on our aspheric micro lens are carried out at only approximate “null” positions. As explained in Chapter 5 misalignment error is unavoidable. Misalignment introduces wave front aberrations, which can be described with the set of Zernike polynomials.

For a very small misalignment, aberrations can be approximated by linear equations. In extracting aspheric micro lens surface profile from OPD map requires misalignment corrections. In order to do corrections, uncertainties in the linear fit should be examined as it was described for radius and aperture. If we consider Equation 6.5 for our misalignment treatment, Z represents higher order aberrations, a represents the lowest order aberrations [tip (a_{11}), tilt (a_{1-1}) and power (a_{20})]. Therefore, the linear equation is higher order aberration as a function of lowest order aberrations. The same way as we did for other parameters, uncertainties due to misalignment will be evaluated using equation 6.9. Its process in the program we developed in relation to Zernikes will be discussed in chapter 9.

7. EXTRACTING BEST FIT CONIC CONSTANT

The surface profile of our aspheric microlens can be retrieved directly from the SWLI measurement technique, and can be generated from PSI by combining the optical path difference (OPD) with a base radius of curvature. Processing the surface profile data and best estimation of conic parameters and their uncertainties are needed to generate the best conic fit to the measurement. The four conic parameters that are estimated from the SWLI measurement are the base radius of curvature, the aperture of the lens, the sag of the lens, and the lens center. The three conic parameters that are estimated from the generated surface profile of PSI measurement are the base radius of curvature, the aperture of the lens and the sag of the lens. Our procedure employs least squares minimization to extract a best-fit conic value, which is then subjected to a Monte Carlo analysis to obtain the combined uncertainty of the best-fit conic constant.

7.1 Chi-square minimization based on SWLI measurement

As described in chapter 6 of equation 6.1, our surface (Z) is a function of the base radius R , aperture radius ρ , and the conic constant K . Since all other parameters except K are estimated from the measurement with uncertainties, the optimization process to find the best-fit is relatively easy. To obtain an optimum best-fit we use a least squares analysis, known as chi-square minimization. Equation 7.1 is the mathematical description of chi-square. In the expression, Z_m is the measured surface height at each pixel; Z_s represents the model surface height profile. Since Z_s is the model, it is the simulated surface height profile, which is a function of R , ρ and K given by Equation 2.9. To understand how the chi-square minimization works see the 2D measurement profile, in

Figure 7.1. Our model is simulated from the pixel size information of the estimate for ρ and the best-fit radius of curvature estimate for R from the measurements. The

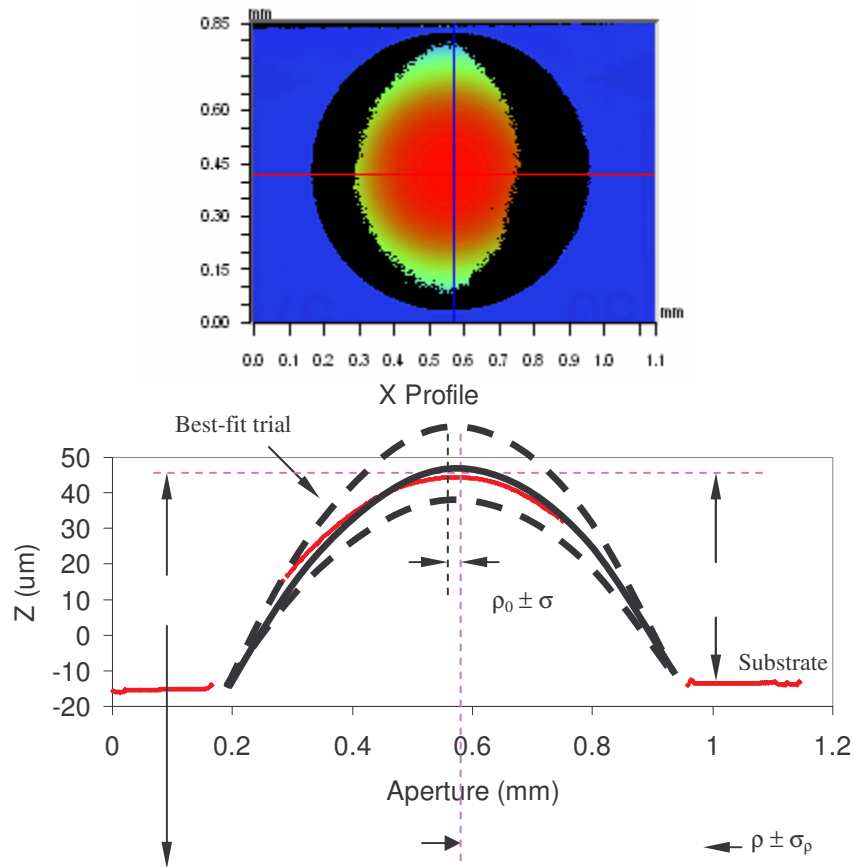


Figure 7.1: (a) Aspheric micro lens surface with its substrate as measured by a scanning white light interferometer using a stitching method. (b) 2D profile of the measurement (red line) as schematically fit with trial models (dotted lines) and the best fit (bold line). The four parameters with uncertainties used to find the best-fit conic constant are shown.

measurement profile is generated from the estimate of the lens center and the sag. This is easily visualized from Figure 7.1(b). We fix the best estimated parameters and vary K to find the best-fit of our measured surface profile. As K varies, the model varies, as illustrated by the dotted lines in Figure 7.1(b). At the K that corresponds to the minimum chi-square, we get the bold line profile, which is very close to the measured line profile. At the chi-square minimum condition, the derivative of chi-square with respect to conic

constant is zero. Based on the method of finding the four uncertainty parameters described in Section 6.1, the best estimates of sag, aperture diameter, and center are $57.7\mu\text{m}$, $800\mu\text{m}$, and $0\mu\text{m}$, respectively for both stitched and not stitched. The radii are $1360\mu\text{m}$ and $1370\mu\text{m}$ for stitched and not stitched, respectively. Using these four best estimate values and varying the conic constant at a step of 0.03, we find the best-fit conic constant. The Matlab code we developed for chi-square minimization is shown in APPENDIX D as a part of Monte Carlo analysis. Figure 7.2 shows the result of a chi-square minimization, where -2.4 and -2 are the best-fit conic constants for the stitched and not stitched, respectively.

$$\chi^2 = \sum_{i=1}^N ((Z_m)_i - (Z_s)_i)^2 \quad (7.1)$$

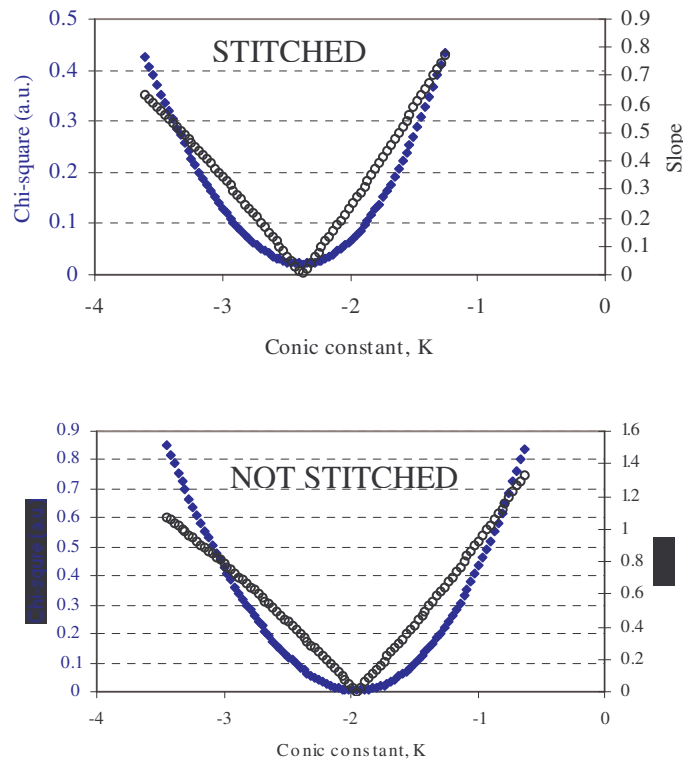


Figure 7.2: Chi-square versus conic constant K . The minimum value of chi-square is at a slope equal to zero. $K = -2.4$ for the stitched data and $K = -2$ for the not stitched data.

7.2 Chi square minimization based on PSI measurement

In PSI measurement, 15 OPD measurement data were taken at “null” position of the aspheric micro lens. The best-fit radius of the micro lens was measured as the difference of recorded positions of confocal and cat’s eye positions. Two spherical micro lenses were measured at ‘null’ position 55 times in order to determine the interferometric bias. We discussed about the three major sources of uncertainty. Here we are going to integrate them in the main program (APPENDIX E) used for our analysis of PSI measurement.

The program we developed for PSI measurement analysis involves the following key procedures, and uses Monte Carlo analysis whenever it is needed. Average 55 measurements of each spherical ball lenses and find their respective Zernike coefficients. Extrapolate Zernike coefficient of the spherical ball lens of the same best-fit radius of our aspheric micro lens. Reconstruct surface map from these Zernikes give us the interferometric bias. Then each of the 15 OPD measurements of our aspheric micro lens is corrected for bias, subtract the interferometric bias from it. The next step is to generate an OPD map from misalignment information of the bias corrected data. This OPD map is subtracted from the sphere radius (same as best fit radius of the aspheric micro lens) to extract the surface profile of the aspheric micro lens. Once the surface profile is determined we use estimates of the base radius of curvature and the lens aperture to generate a model conic surface for which only the conic constant remains an unknown fit parameter. Therefore, we extract the best-fit conic constant using the least squares minimization process, and then we apply the Monte Carlo analysis to find the combined uncertainty of the best-fit conic constant.

7.2.1 Radius and lens aperture distributions

As we described in section 6.2.2, the measurement of the best fit radius is calculated from the difference between the “null” positions of confocal and cat’s eye. Since it is not possible to null the micro lens, we measured the power terms and z positions in either side of the confocal and cat’s eye “null” positions and plot z versus power term from which the difference between the z intercepts of the two plots give us the radius value. The best-fit radius distribution is found using linear square fit as described in section 6.2.2. We extrapolated 100 measurements with Gaussian distribution in which the mean is the best-fit radius of our aspheric micro lens. Note that the best estimate of the best-fit radius of curvature (calculated from the least square minimization

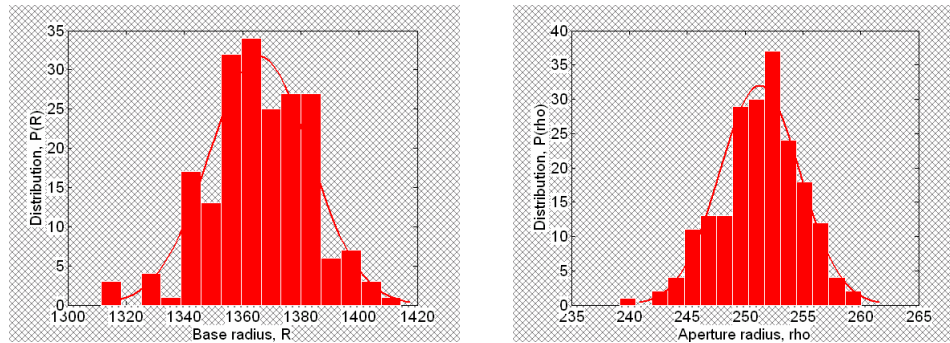


Figure 7.3: Radius and aperture distribution used in the analysis.
 (a) $R=1366\mu\text{m} \pm \sigma_R$, $\sigma_R =17.2\mu\text{m}$ (b) $\rho=251.4\mu\text{m} \pm \sigma_\rho$,
 $\sigma_\rho=3.4\mu\text{m}$

of z versus power term plots) is $1366.1 \mu\text{m}$. Since we estimate a cone angle of $10.6^\circ \pm 1$ and an aperture is related to the best-fit radius as described in Equation 6.10, we found out that the best estimate of the aperture radius is $251.4 \mu\text{m}$. In our Monte Carlo analysis during the extraction of surface profile of our aspheric micro lens, the distributions of radius and aperture after repeating the process 200 times is shown in Figure 7.3. Based on

theses distributions, the mean value (with mean uncertainty) of the radius and aperture radius are (1366 ± 1.22) μm and (251.4 ± 3.4) μm , which are about the same as our best estimates.

7.2.2 Interferometric bias

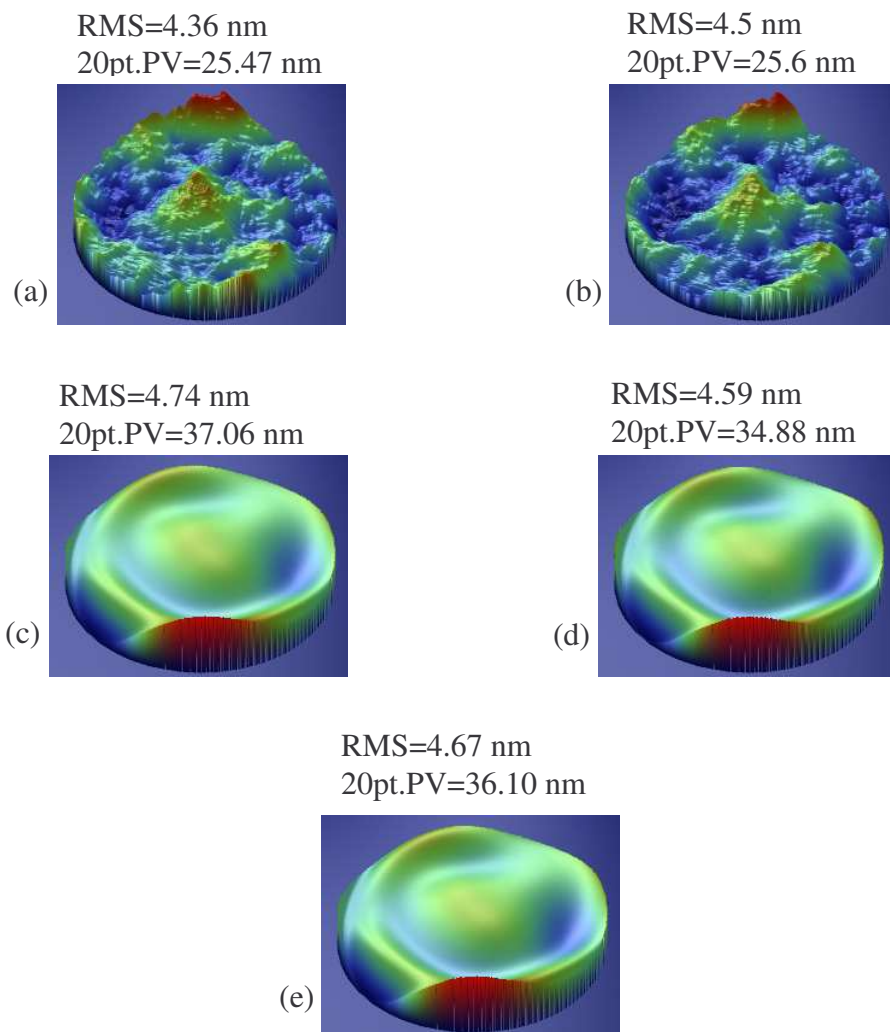


Figure 7.4: Interferometric bias extrapolated from the measurement of two spherical micro lenses. (a) and (b) are the raw bias (after averaging 55 measurement) from 0.99mm and 1.985mm radius balls respectively. (c) and (d) are bias maps from the same balls based on 36 Zernike coefficients. (e) the extrapolated bias from the ball of radius 1366.1 μm .

In the bias analysis, we measured two spherical ball lenses of radius 0.99mm and 1.985mm. Since the best fit radius measurement of the aspheric micro lens is between these radius values we decided to measure these balls 55 times and extrapolate the bias for the best-fit radius equal to the mean value of the radius distribution. The main concept behind the method of finding the interferometric bias is that, after the repeated measurement of a ball randomly, the random errors of the measurement can be eliminated by averaging, and the only error left is the interferometric bias error.

All the 55 measurements are averaged after subtracting tip, tilt and power from each measurement and Zernike coefficients of this averaged measurement is found. Since we did it for the two spherical balls, we extrapolate the Zernike coefficients to the radius of curvature equal to the best-fit radius of our aspheric micro lens. These coefficients are multiplied by the corresponding Zernike polynomials to obtain the bias map. Figure 7.4 shows the interferometric bias due to the three spheres from which Figure 7.4 (e) used in the analysis.

7.2.3 OPD map due to misalignment

The OPD measurement is done at confocal “null” position of the aspheric micro lens. It is obvious and explained in Chapter 5 that there is always misalignment error in the measurement. This OPD measurement is corrected and reproduced as we call it using misalignment correction as follows. We subtract interferometric bias map from a randomly picked measurement of the 15 raw OPD measurements. Then we find the Zernike coefficients of this bias corrected OPD measurement data after subtracting tip/tilt and power. Plot all the higher order Zernikes versus the lowest order Zernkes to apply the linear square fit to find uncertainties in the slope and offset using Equation 6.8. The new

slope and offset can be rewritten as the sum of the linear square fit slope or offset plus the Gaussian distribution (will be discussed in section 7.3) of slope or offset. Therefore the new slope or offset is given by Equation 7.2.

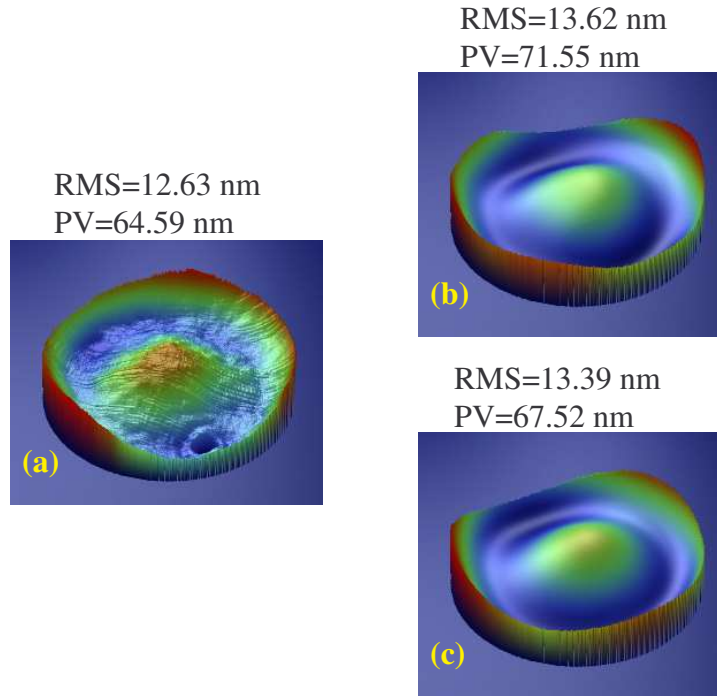


Figure 7.5: (a) Bias corrected OPD measurement (b) reproduced OPD map from Zernikes (c) randomly generated OPD map after misalignment correction.

$$\begin{aligned} m' &= m + G(\mu_{m'}, \sigma(m)^2) \\ Z'_0 &= Z_0 + G(\mu_{Z'_0}, \sigma(Z_0)^2) \end{aligned} \quad (7.2)$$

Since the uncertainty can be approximated by one sigma of a Gaussian distribution of mean zero, we use them in finding the new values of these higher order Zernikes. The new higher order Zernikes is found using Equation 6.3 by replacing the slope and offset by the new slopes and offsets of equation 7.2. In this analysis, we use the first 16 Zernike terms out of 36 Zernike terms, which we consider the biggest contributors for OPD surface map. Finally, the OPD map is plotted so that it is ready to be added to surface

map of a sphere of radius equal to the base radius of the aspheric micro lens. Figure 7.5 shows an example of randomly generated OPD map in the course of the analysis. As it is shown in the Figure, the most part of the corrected measured OPD map is about the same as the generated OPD map. This is true not only by the observed picture but also by the values of RMS and PV values. The generated OPD map differs by RMS value of 0.76 nm (~6%) and by PV value of 2.93 nm (~4.5%) from the measured OPD map. This is just randomly picked example. We compared the averages and found out that differences in RMS and PV between the measured and generated OPD are smaller than 4% and 2% respectively. Note that we get different OPD maps from misalignment corrections. Since the generated OPD maps are based on the measured OPD, their differences due to misalignment correction analysis directly contribute to the measurement noise. Therefore, when we do the Monte Carlo later in Section 7.3, we consider the measurement noise as one of the parameters to vary.

7.2.4 Surface profile generation and extracting the best fit conic constant

In order to facilitate the method of extracting the best-fit conic constant, our aspheric micro lens surface profile had to be generated. The two essential parameters needed to generate the surface profile are the OPD map and the base radius of curvature (approximated by best fit radius) of our aspheric micro lens. The best-fit radius of curvature distribution and misalignment corrected OPD maps are found based in previous sections. Now, the surface profile is generated by subtracting OPD from the base radius of curvature as described in section 6.2.1. Figure 7.6 shows an example of generated surface profile.

The next step is to find the best-fit conic constant by least squares minimization method. In order to find the best-fit, we simulate our surface using the general sag equation

described in Equation 2.9. As the equation, we should use the base radius of curvature, which we do not have from the PSI measurement. The base radius of curvature can be calculated by adding correction due to OPD in the direction of the optic axis to the best fit radius of sphere calculated from the z versus power plot as described in section 6.2.2.

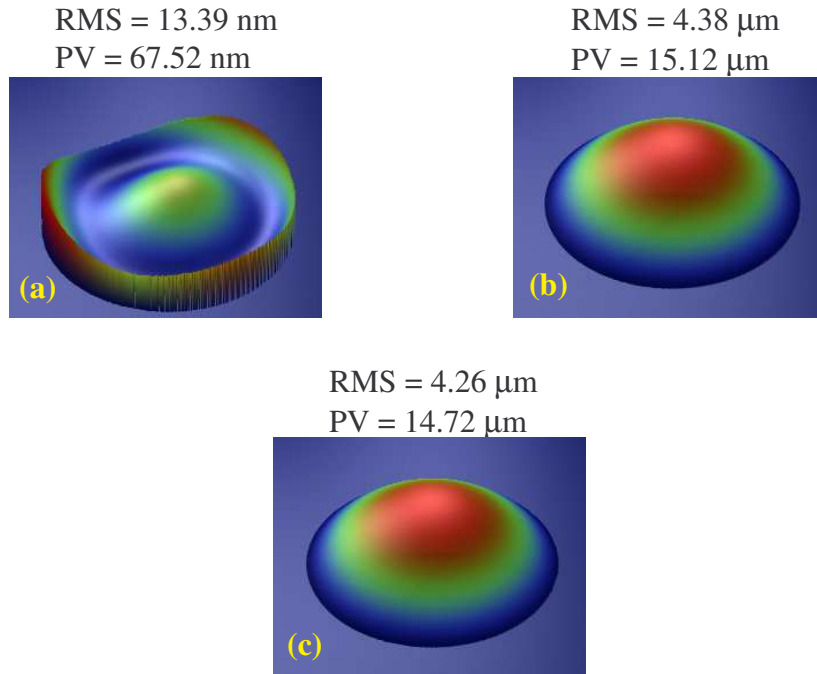


Figure 7.6: (a) Misalignment corrected OPD map (b) sphere profile of radius 1371.48 μm (c) Generated surface profile of the micro aspheric lens Profile.

The OPD in the optics axis direction is nothing but it is the difference between aspheric and sphere for a fixed aperture as discussed in section 2.2. But the idea of adding OPD from Zernike coefficient results is not straightforward. The Zernike coefficient we obtained from the OPD measurement involves aberration balancing, mixed of low and high order aberrations. Therefore, we need to find the relationship between Zernikes and the power series wavefront aberrations.

The relationship between Zernikes and the power series wavefront aberrations are described in references 47 and 49, and described at the end of chapter 4 of this dissertation. Since we need the focus term for correction, the primary Seidel with Zernike relationship is enough. The focus term of this relationship as stated in reference 47 is given by

$$W(\rho)_{focus} = \rho^2 \left(2Z_3 - 6Z_8 \pm \sqrt{Z_4^2 + Z_5^2} \right) \quad (7.3)$$

Where Z_3 , Z_8 , Z_4 , and Z_5 are the measured Zernike coefficients for power, low order spherical aberration, 0° astigmatism and 45° astigmatism, respectively.

The Zernike coefficients follow the ISO representation described in Section 4.4. Using Equation 7.3, we plugged the Zernike terms from the PSI analysis and found $0.2 \mu\text{m}$. This represents curvature in the wavefront in the paraxial limit (in the region near the optical axis). This is the curvature information of interest to determine the radius of the lens near the apex. We can convert the $0.2 \mu\text{m}$ curvature to an approximate distance the microlens would have to be moved to null out this curvature. This is the radius correction value we are after. We can determine this distance with the interpolation information used to determine the two null positions for cat's eye and confocal in the radius measurement. The correction value is $\sim 0.7 \mu\text{m}$. In order to correct and find the base radius, we have to add $0.7 \mu\text{m}$ to the best-fit radius of $1366.1 \mu\text{m}$. However, the uncertainty of the best-fit radius found from Section 7.2.1 is $17 \mu\text{m}$. The correction as compared to uncertainty is really small which can be ignored, and use the best-fit radius as the base radius. In addition to the base radius, we used the best estimate of aperture radius of $251.4 \mu\text{m}$. Another important parameter we need is the sag. Since we cannot directly get the information as we have done for SWLI, here we approximated by the average sag values of the 200 generated surface profiles. Using this approach, the best estimated sag is about $22.9 \mu\text{m}$.

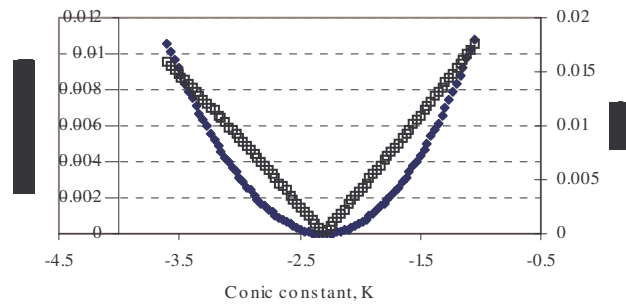


Figure 7.7 Chi-square versus conic constant K . the minimum value of chi-square is at a slope equal to zero. $K=-2.3$

As we have done for SWLI, we used the base radius and aperture radius information to generate the simulated surface profile and the sag is to regenerate our extracted surface profile (same as measured surface profile). Then we fix the best estimated parameters and vary conic constant K to find the best-fit conic constant. This is done based on the chi-square minimization formula given by equation 7.1. Using the best estimate values (base radius, aperture radius, and sag) and varying the conic constant at a step of 0.03, we find the best-fit conic constant. Figure 7.7 shows the chi-square and its derivative (slope) plots, which indicate the best-fit conic constant.

7.3 Monte Carlo for best-fit conic constant

Our Monte Carlo simulation code (APPENDIX D) is used to determine the combined uncertainty in the best-fit conic constant. The estimates of the four parameters discussed above are assumed to follow Gaussian distributions. The well known Gaussian distribution curve is given by the expression 7.4 and shown in Figure 7.8. The probability, $P(x)$ of one sigma (σ) is the integration of Gaussian curve bounded by $\mu \pm \sigma$. In Figure 7.8, the shaded region is the probability of one sigma for zero mean is about 68.27%. Based on the Gaussian assumption, the uncertainty u is approximated by one sigma. In

our analysis, each of the four parameters has its own mean (μ) and sigma (σ). These are taken to be the best estimate for the parameter and its uncertainty.

$$G(\mu, \sigma^2) = \frac{e^{-\frac{(x-\mu)^2}{2\sigma^2}}}{(2\pi\sigma^2)^{1/2}} \quad (7.4)$$

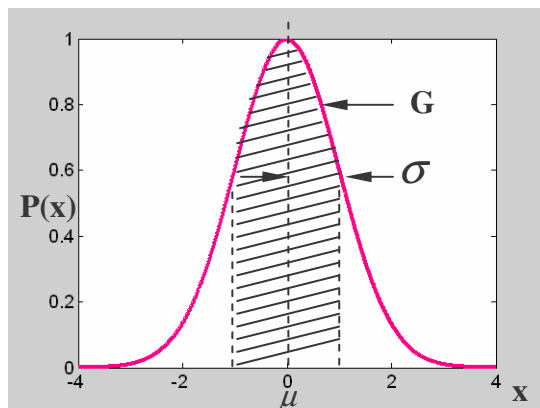


Figure 7.8: Probability distribution. G is the Gaussian curve, σ represents the spread and the shaded region is its probability which is equal to 68.27%

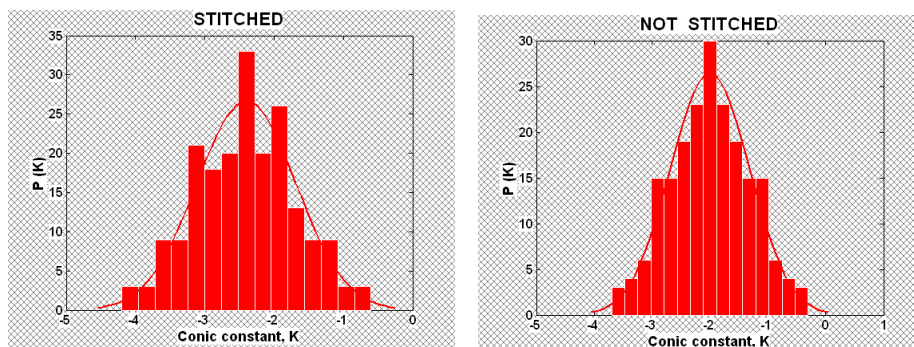


Figure 7.9: The probability distributions of the best-fit conic constant of stitched and not stitched measurement data. The best-fit conic constants are -2.4 ± 0.72 and -2 ± 0.68 for stitched and not stitched respectively

In the case of SWLI measurement, our Monte Carlo code randomly picks radius, aperture, sag, and center location from these Gaussian distributions. The radius and aperture values are used to generate the model of the surface profile, while the sag and the center

location are used to generate the surface profile from the data. In addition to these parameters, it randomly picks a measurement among the set of eleven measurements to capture the uncertainty due to noise between measurements. This process is repeated 200 times to find 200 different combinations of the four input parameters. The result is a distribution of best-fit conic constant values. The distributions for the stitched and not stitched measurements are shown in Figure 7.9.

The widths of these distributions are good estimates of the combined uncertainties. Although the means at first glance are quite different, they are within one sigma of each other. However, given that the estimates of the base radius are different between stitched and not stitched and that more of the surface is measured with the stitching procedure, a difference in the best-fit conics is expected.

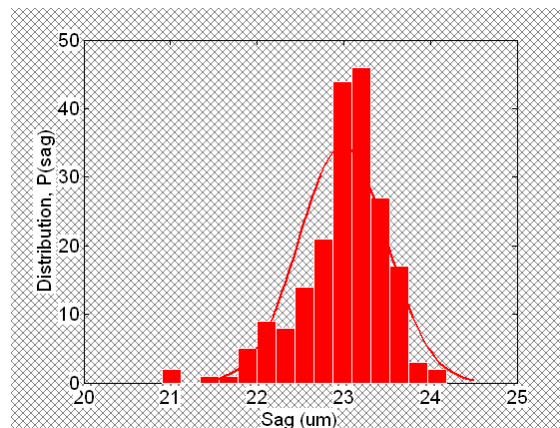


Figure 7.10: Sag distribution (22.9 ± 0.50)

The Monte Carlo simulation code (APPENDIX D) used for SWLI measurement analysis is also used for PSI measurement with a slight modification. Estimates of the three parameters (base radius, aperture radius and sag) discussed in Section 7.2.4 are assumed to follow Gaussian distribution. The base radius (approximated by best fit radius) and aperture radius distributions are shown in section 7.2.1. In the same way, the sag

distribution found from the 200 generated surface profiles is shown in Figure 7.10. As we saw from the distribution, the sag is $(22.9 \pm 0.5) \mu\text{m}$.

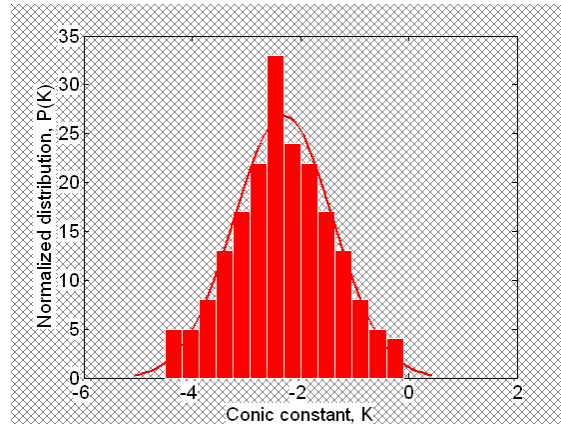


Figure 7.11: The probability distribution of the best fit conic constant of the the generated surface profiles of OPD measurement. $K = -2.27 \pm 0.91$

As we have done for SWLI, the Monte Carlo analysis is used to determine the combined uncertainty in the best-fit conic constant. The Monte Carlo code randomly picks base radius, aperture radius, and sag from their respective distributions. In addition to these parameters, the code randomly picks a measurement among the set of 200 extracted surfaces (same as measurement data). The result is the distribution of best-fit conic values where the mean value is about the same as the best estimate of the best-fit conic constant. It is summarized in Figure 7.11.

7.4 Uncertainty parameters effect on the best-fit conic constant

As described in our Monte Carlo analysis of section 7.3, each of the uncertainty parameters is randomly picked from their respective distributions and one of the measurements at a time to find the best-fit conic constant through chi-square minimization process. This tells us the combined effect of uncertainty parameters on

finding the best-fit conic constant. This is good to get the best-fit conic constant value and the overall broadness of the distribution but it doesn't tell us the individual contributions directly.

To assess the contribution of each parameter's uncertainty, we carry out the Monte Carlo analysis where only a single parameter is varied at a time. The other parameters are set at their best estimate values. In the case of SWLI measurement, the average of the eleven measurements is used for the surface height data as each of the parameters is allowed to vary. To estimate the impact of the noise only, we fix the four parameters to their best estimate values and randomly pick a measurement from the group of eleven. Fifty iterations were used for this analysis. The mean and sigma values of the resulting conic distributions are summarized in Table III and shown in Figure 7.12.

Table III: The best-fit conic constants due to individual parameters, measurement noise, and combined (All).

SWLI (best fit conic constant)				
	Stitched		Not stitched	
	μ	σ	μ	σ
ALL	-2.44	0.72	-1.98	0.68
RADIUS	-2.44	0.55	-2.00	0.62
SAG	-2.36	0.47	-1.92	0.39
NOISE	-2.49	0.29	-1.93	0.36
APERTURE	-2.35	0.26	-1.98	0.25
CENTER	-2.37	0.00	-1.95	0.00

For a given stitched or not stitched condition, we expect the mean conic values shown in Table III to be the same. Taking the uncertainty in the mean as the standard deviation of the values divided by the square root of N ($N=50$ here) [11], we see that the observed variation is not statistically significant. For example, the mean conic value for the stitched case when all parameters are varied (All) is -2.44 ± 0.1 and the mean conic values for the individual parameter investigations are within this uncertainty. The same

is true for the not stitched case where the mean for the full Monte Carlo is -1.98 ± 0.1 .

The relative importance of the individual contributions to the overall uncertainty can be appreciated from plots of these distributions, as shown in Figure 7.12. The data in Table III is used to generate Gaussian profiles. The mean of each distribution is shifted to zero so the widths can be clearly compared.

The full Monte Carlo analysis, where all parameters and noise are varied, leads to the broadest distribution for both stitched and not stitched, as expected. The listing order of

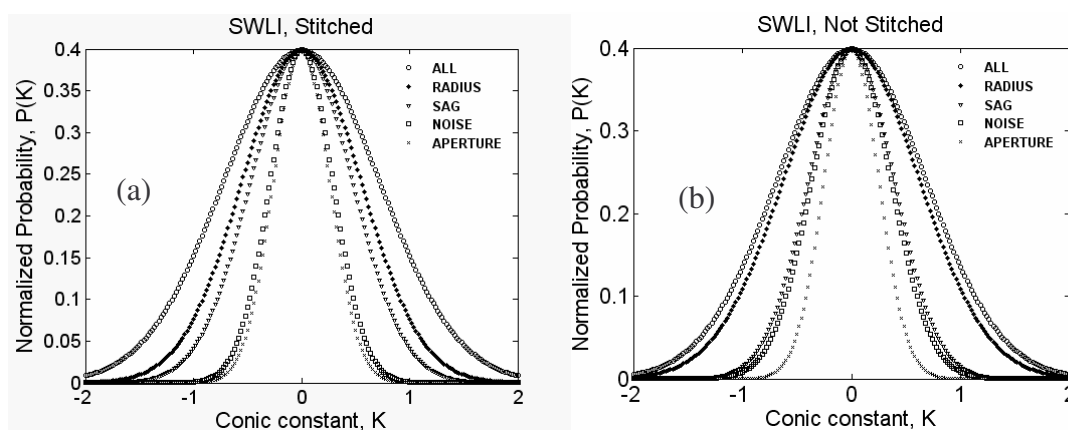


Figure 7.12: (a) The distribution of uncertainty parameters versus conic constant for stitched data. (b) The distribution of uncertainty parameters versus conic constant for not stitched data.

the parameters in the figures convey their relative significance. The uncertainty in the radius is the dominant contribution but uncertainty in the center is the least contribution for both stitched and not stitched measurements. From this analysis, one can determine what aspect of the measurement must be improved to reduce (optimize) the final conic uncertainty. Note that the best-fit conic is very sensitive to the base radius value. Uncertainties for both the stitched and not stitched R values are $20 \mu\text{m}$ ($\sim 1.5\%$) and this small uncertainty broadens the K distributions to a sigma of ~ 0.7 ($\sim 30\%$ for stitched and $\sim 36\%$ for not stitched). Consequently, part of the difference in the mean conic between

stitched and not stitched is due to the 10 μ m difference in the best estimate R values ($R = 1.36$ mm and 1.37 mm for stitched and not stitched, respectively). Setting the mean R to 1.37 mm rather than 1.36 mm for the stitched analysis and repeating the Monte Carlo process confirmed this. The best-fit conic constant for the stitched drops to -2.1 , which is closer to the not stitched best-fit conic constant. The presence of more surface data in the stitched measurements also contributes to the difference between stitched and not stitched conic means. Repeating the Monte Carlo procedure with the stitched data, but masking it down to the same diameter as the not stitched data, in addition to setting the base radius estimate to 1.37 mm, investigated this. The result of the conic distribution has a mean of -2.05 , which again is closer to the not stitched mean of -1.98 .

Individual parameters and measurement noise can also be evaluated using Monte Carlo analysis in the case of PSI measurements. Varying each parameter at a time keeping the rest at their mean positions can do this. The three parameters (base radius, aperture radius, and sag) mean positions are their best estimate values described in Section 7.2.2. The mean of measurement data is the average value of the 200 generated surface profiles. The mean and sigma values of the resulting distributions are summarized in Table VI and shown in Figure 7.13.

Table VI: The best-fit conic constants due to individual parameters, generated surface noise, and combined (All)

	PSI (best fit conic constant)	
	μ	σ
ALL	-2.27	0.91
RADIUS	-2.39	0.71
SAG	-2.29	0.70
NOISE	-2.35	0.68
APERTURE	-2.21	0.38

Even though the means shown in Table VI is expected to be the same, statistically speaking, the variations of the means are insignificant. This can easily be seen by calculating the uncertainty in the mean of “All”. Since we iterated 50 times in the code, the uncertainty in the mean is about $0.13\mu\text{m}$. Therefore, all the means are within $(-2.27 \pm 0.13)\mu\text{m}$. The relative importance of the individual contributions to the over all uncertainty (combined, All) can be appreciated from plots shown in Figure 7.13. The data in VI is used to generate these distributions, where the mean of each distribution is shifted to zero. The combined effect of all the parameters is the broadest distribution as expected. Even though the radius leads to the broadest distribution next to “All”, the relative significant of the contributions from the base radius, noise, and sag are comparable. In our PSI technique, we described that the OPD measurement data is related to misalignment. We generated OPD maps from the misalignment correction as described in Section 7.2.3. Because the OPD data and the base radius information are used to generate surface profiles, the noise is directly related to the misalignment information.

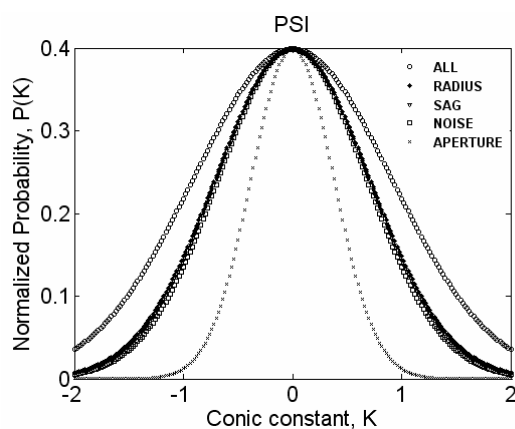


Figure 7.13: The probability distribution functions for the individual parameters versus conic constant

8 SUBTRACTING INTENDED SHAPE

Intended shapes (surfaces) of an aspheric micro lens can easily be simulated using the general mathematical expression for general aspheres given by Equation 2.9. Since the design shape of this particular aspheric micro lens has a conic surface of base radius 1.375 mm and conic constant of -2.1 , we used the special case of general asphere expression which assumes all deformation constants to be zero for conic surfaces. Prior knowledge of the micro lens is necessary so that our measurement data can be subtracted from it. We obtain the design information from Digital Optics Corporation (DOC).

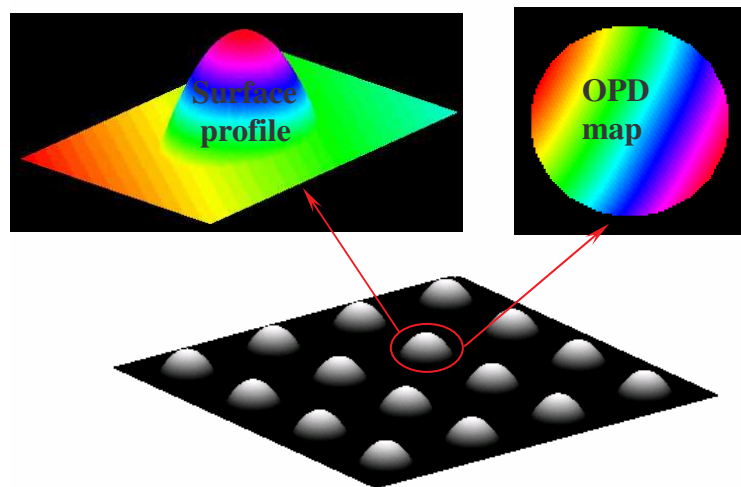


Figure 8.1: A simulated micro lens arrays and simulated measurements of a refractive micro lens based on SWLI technique (surface profile) and PSI technique (OPD map).

In order to validate our analysis we should be able to verify our measurement simulation code. In general, from an array of micro lenses, one of them can be picked up and measured for its surface profile directly using SWLI technique or its OPD measurement using PSI technique. Both techniques applied on the measurement of an aspheric micro lens can be simulated as shown in Figure 8.1.

The intended aspheric micro lens measured in different setup of interferometer can be simulated and analyzed. APPENDIX F is the matlab code we developed for simulated measurement of intended shape. Since we used two interferometer set ups, which follow two different techniques, SWLI and PSI, we need crucial information that is required for simulation. Knowing the objective used in the interferometer and pixel information we can simulate the measurement. In the next two sections of this chapter, we described simulated measurements of intended aspheric micro lens on two different setups, SWLI and PSI.

8.1 Subtracting intended shape from the surface profile measurement

An aspheric micro lens measurement on a SWLI can easily be simulated based on the information of our intended shape conic parameters, numerical aperture (NA), and pixel size information from the interferometer. The NA of New View 5000 with a Mirau objective of 10X is 0.3 and the pixel size is $1.1\mu\text{m}$ (640 X 480) with system magnification of one. In addition to these, we can incorporate like misalignment and noise to make it look like the real measurement. To simplify things we added just noise in our code, APPENDIX F, which simulates the measurement of our intended aspheric micro lens. Now we have two surface profiles, the intended shape and the measurement of the intended shape (our aspheric micro lens). Figure 8.2 shows two types of measurements (with or with out noise) based on SWLI technique. Subtracting the intended shape from the measured surface profile of the intended gives us the residual surface error profile. Since our reference (intended) surface is the same as measured (by simulation), ideally we expect zero for the difference between intended and simulated measurement data (with out noise). As shown in Figure 8.2 it is 0.05 nm, close to zero. In the second part of the simulated measurement ,we added a Gaussian noise with zero

mean and $0.3\mu\text{m}$ sigma, we get $\sim 20\text{ nm}$ as the difference between Intended shape the simulated measurement data (with noise), As it can easily be assessed, the 20 nm RMS is

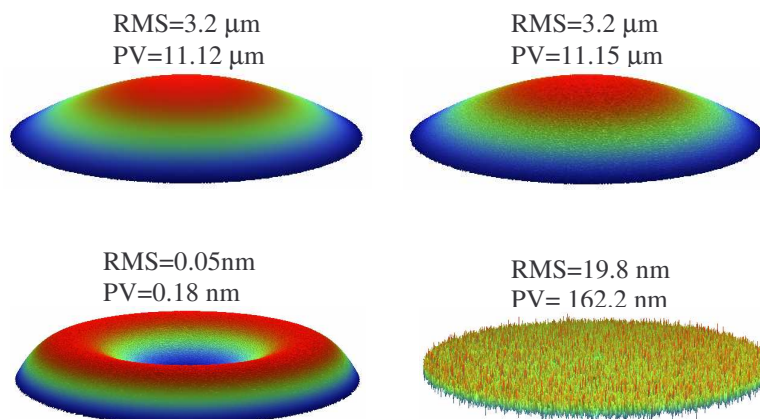


Figure 8.2: The simulated measurements of the intended shape without noise and with noise are shown at the top left and right respectively. The measurement covers $220\mu\text{m}$ aperture radius. Intended subtracted from measurement data (with out noise) and Intended subtracted from measurement data (with noise) are shown at the bottom left and right respectively.

because of the added Gaussian noise but the 0.05 nm may be from the approximations used in the simulated measurement code (APPENDIX F) and the conversion of data files between two different programs (Matlab and Vision). These results explained how good our simulation is. In addition to this the optimum conic constant is -2.1 (same as intended) for simulated measurement without noise but -2.17 for simulated measurement with noise. It is important to notice here is that the noise affects the best-fit conic constant measurement. Other parameters can be changed to show the effects on the best-fit conic constant values. But this is just enough to show that measurement can be simulated. Since the actual effects of parameters on our measurement are explained in Chapter 9, we do not need to simulate the measurement.

8.2 Subtracting intended shape from the OPD measurement

As we have simulated measurements of SWLI, we can also simulate the measurements of our intended aspheric micro lens based on PSI technique. The Twyman Green set up of Fisba Optik follows the PSI technique to give us the OPD measurement data. The NA of spherical objective used is 0.34 and the pixel size of $2.285\mu\text{m}$. In addition to this, the conic parameters of our intended aspheric micro lens are needed to simulate the OPD measurement of Fisba Optik.

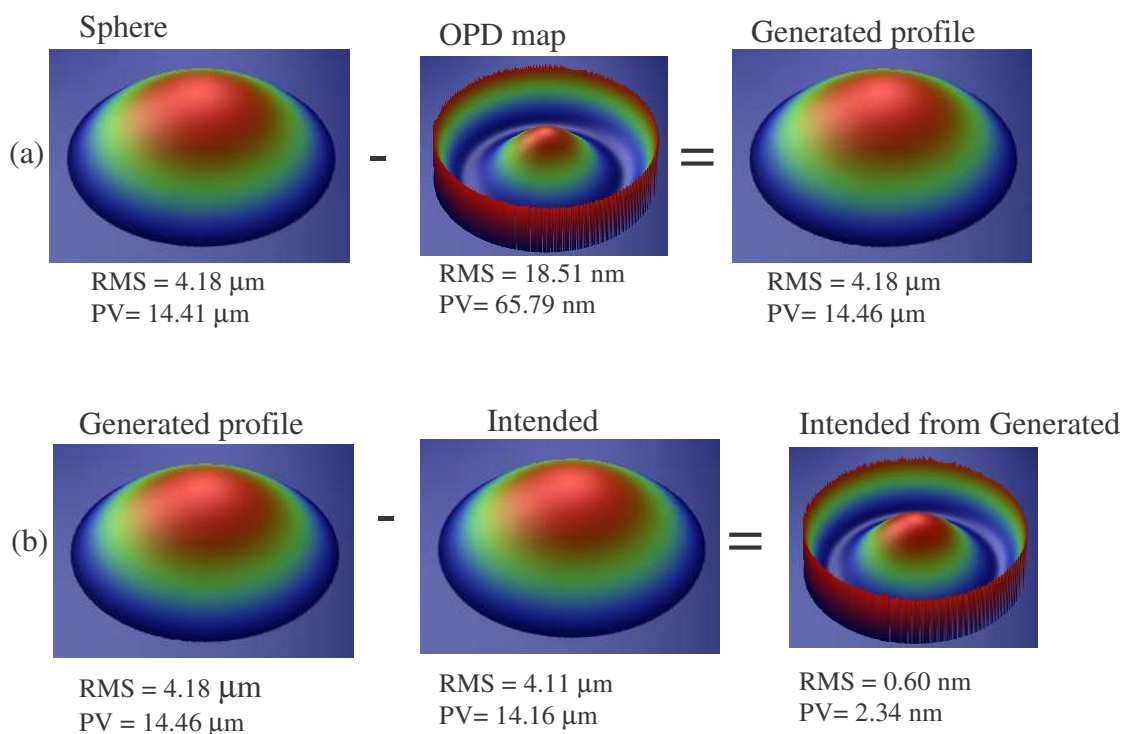


Figure 8.3: (a) The surface of an aspheric micro lens is generated by subtracting simulated OPD measurement data from a sphere with radius equal to the base radius of the lens. (b) The deviation of generated from the intended is found by subtracting intended from the generated surface profile of the micro lens. Aperture radius is $251\ \mu\text{m}$

We developed a Matlab code (APPENDIX G), which simulates the OPD measurement of our intended aspheric micro lens. To discuss about subtracting the design

shape in this type of measurements, we need to go further in extracting the surface profile from OPD maps. We already derived an equation to extract the surface from the OPD map in Section 6.2. The simulated OPD measurement should be subtracted from the sphere of radius R according to Equation 6.2. As an example, we simulated the OPD map of an aspheric micro lens of base radius $1375\ \mu\text{m}$ with conic constant of -2.1 as measured by Fisba Optik and shown in Figure 8.3. The first part of the figure shows how to generate the surface profile of an aspheric micro lens. To get our OPD map we assumed the null position of our micro lens coincides with the reference sphere wavefront of radius equal to the base radius of the micro lens. As we know from the discussion of general aspheres, these two radii are the same only at the apex point. Because of this, our OPD map at “null” position cannot be zero. Since the OPD map simulated is the deviation of the micro lens surface from the sphere wave front, we simply subtract the OPD map from the sphere in order to generate the surface profile of the lens. Finally, to understand how good the surface is generated, we compared it to the intended shape as shown in Figure 8.3(b). The RMS is not zero as expected. This is because of the fact that the OPD is calculated along the radius but the surfaces are subtracted along z -direction. Therefore, the surface error results for both SWLI and PSI are small. As it was indicated in the above two Figures, the residual surface error after subtracting intended shape from the simulated data (without noise) are about $0.05\ \text{nm}$ and $0.6\ \text{nm}$ in RMS for SWLI and PSI techniques respectively. This tells us that the difference in residual error analysis may be different by a maximum of about $0.6\ \text{nm}$ RMS (for $502\ \mu\text{m}$ aperture diameter) which comes from approximations and the program itself. We will see how this error compared to overall residual surface error to be discussed in Chapter 9. If the surface error is more

than 100 nm, the contribution from 0.6 nm errors is less than 0.6%. Depending on demanding applications, this kind of error can be ignored.

9. RESIDUAL ERROR ANALYSIS

We discussed on how to get surface measurement data of an aspheric micro lens based on two techniques, SWLI and PSI. In the case of SWLI technique, we described how to correct the surface profile measurement and estimate four major parameters (base radius, aperture radius, sag, and center of the lens) to find the best fit on the bases of chi-square minimization and optimize the best-fit conic constant. In the case of PSI measurement, we described the three main sources of uncertainty parameters namely, the best-fit radius, aperture of the lens, and misalignment. We discussed how to correct for misalignment in Section 7.2.3. We also discussed in detail how to extract the aspheric micro lens surface from its OPD measurement in Chapters 6 and Section 7.2.4. For both techniques, we subtract the design shape and the best-fit surfaces from the surface profile of the measured (or generated surface from OPD measurement in the case of PSI) aspheric micro lens. In doing this we obtain the remaining profiles, which are called the residual surface error maps. We then fit each of the surface error maps to a set of Zernike polynomials to capture the dominant aberrations and their variations. The result is a distribution of a Zernike coefficient (aberration) describing the surface error. Therefore, as we have done for the best-fit conic constant based on Monte Carlo analysis, we are going to obtain the combined uncertainty of an aberration. Furthermore we will investigate the individual aberration contributions.

9.1 Surface error analysis based on SWLI measurement

In the SWLI measurements, the surface height profile from the NewViewTM 5000 is corrected for tip and tilt using Vision[®] 32 software. The corrected surface data, the best-

fit surface profile, and the intended surface height profile are used in the analysis discussed below. As described in Sections 7.1 and 7.2, our least squares minimization and Monte Carlo analysis are used to find the best-fit conic value and associated combined uncertainty. Since we have the best-fit conic constant, we have the best-fit conic surface. The intended surface is generated from the design parameters provided by the micro-lens manufacturer, Digital Optics Corporation. The residual surface error is

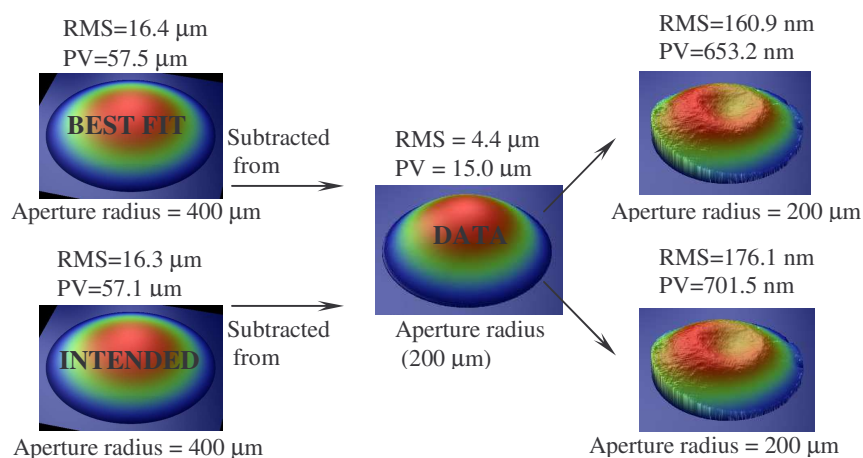


Figure 9.1 Residual surface error map of stitched data. The surface error as best fit subtracted from data is shown at the top right. The surface error as intended subtracted from the data is shown at the bottom right

found by subtracting the intended surface from the data. We can also regard the residual surface error as the deviation of the best fit from the measured data. As an example, the residual surface error maps are shown to the right in Figure 9.1. The error maps are masked to a circular aperture and only piston has been removed since the tip and tilt of the data is corrected based on the substrate tip and tilt information as described in Section 6.1. We choose a circular aperture in order to accommodate a Zernike polynomial fit to the residual error [56]. The difference between the two residual error maps appears small. The difference in RMS values is 15.2 nm. This suggests that even though the difference

between the intended surface profile and the best-fit surface profile is small, the best-fit method by itself is not comprehensive for the characterization of microlenses. In the same way the residual surface error maps for the not stitched measurement is shown to the right in Figure 9.2. The difference in RMS values is also small, about 6 nm, indicates again the difference shows the best-fit method by itself is not enough to know all about the microlens.

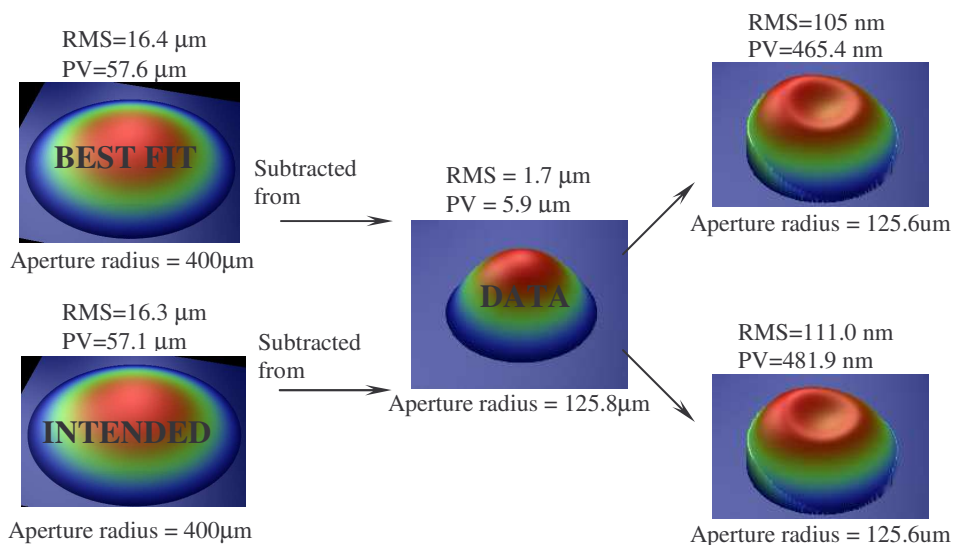


Figure 9.2 Residual surface error maps of not stitched data. The surface error as best fit subtracted from data is shown at the top right. The surface error as intended subtracted from the data is shown at the bottom right.

In general, both stitched and not stitched measurements give us about λ agreement with the intended lens shape and the best-fit conic shape. In addition to the best fit conic surface, the residual surface errors, described as aberrations give us a lot of information about our aspheric micro aspheric lens. These aberrations are useful for describing the lens performance and in providing feedback to the manufacturing so that process can be monitored.

Therefore, the final step in our analysis is to fit the residual surface error maps to Zernike polynomials to get the 36 Zernike coefficients. The mean (μ) and sigma (σ) values of the 36 Zernike coefficients from the full Monte Carlo analysis of 200 iterations are summarized in APPENDIX H. The dominant aberrations we found in our analysis are a_{11} (tip), a_{1-1} (tilt), a_{20} (defocus), and a_{40} (third order spherical aberrations), for both stitched and not stitched. Let us focus on the rotationally invariant components (a_{20} , a_{40} , and a_{60}) as it is summarized in Table IV. With the Zernike polynomials, a higher order radial term (e.g. the a_{60} polynomial) includes lower order radial terms. For example, the a_{60} Zernike coefficient corresponds to the polynomial $20\rho^6 - 30\rho^4 + 12\rho^2 - 1$ [47]. In the same way, the a_{40} and a_{20} are related to the 4th power and 2nd power of ρ , respectively. Therefore, our aspheric micro lens surface shape is related to these polynomials. It is very clear that an approximate profile of the aspheric micro lens is related to a ρ^2 surface profile. This can be seen from Table IV of “Intended from best fit” column, since the a_{20} coefficient is dominant.

Table IV: Mean (μ) and sigma (σ) values of the dominant aberrations. All units are in nanometers (nm).

Zernike	Intended from data				Best fit from data				Intended from best fit			
	Stitched		Not stitched		Stitched		Not stitched		Stitched		Not stitched	
	μ	σ	μ	σ	μ	σ	μ	σ	μ	σ	μ	σ
a_{20}	-87	52	-178	91	-37	77	-147	110	50	55	31	60
a_{40}	-148	8	-114	14	-147	8	-114	14	-2	2	-0.07	3
a_{60}	15	7	40	12	15	7	40	12	0.01	0.01	0.0	0.01

As was done for the best-fit conic analysis, we can ascertain the contribution of the individual parameters to the final uncertainty in these Zernike coefficients by allowing only one parameter to vary at a time. The uncertainty in these coefficients is related to the

uncertainty of the input parameters. These parameters are discussed in Sections 7.1 and 7.2. As an example, consider the impact of the input uncertainties on the third order spherical aberration. Table V summarizes the spherical aberration distributions due

Table V: Mean and sigma values of the spherical aberration Zernike coefficients.

SWLI (spherical aberration)				
	Stitched		Not stitched	
	μ (nm)	σ (nm)	μ (nm)	σ (nm)
ALL	-147.4	8.4	-112.5	13
NOISE	-148.7	7.9	-114.4	12
RADIUS	-148.3	1.9	-111.9	2.1
APERTURE	-147.8	1.8	-111.5	0.4
SAG	-147.9	1.5	-111.5	1.3
CENTER	-148.1	0.2	-110.6	0.9

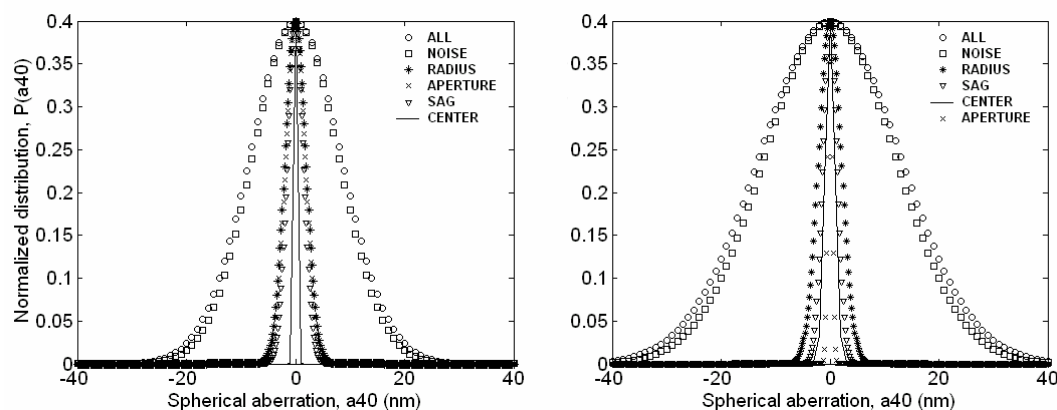


Figure 9.3: (a) The probability distribution functions for the individual parameters versus spherical aberration, a_{40} , for the stitched data (b) The probability distribution functions for the individual parameters versus spherical aberration, a_{40} , for not stitched data

to the four uncertainty parameters, measurement noise, and combined (ALL). Based on Table V, their respective contributions are shown in Figure 9.3. As we have done in the case of conic constant distribution, the mean values are shifted to zero so that the widths of the distributions can be clearly compared. Measurement noise is the largest contributor

to the overall a_{40} residual error uncertainty. Again, the mean a_{40} values should be the same when only single parameters are allowed to vary. As it is done in Section 7.3, we check the statistical significance of the mean values by calculating the uncertainty in the mean. We find that the mean a_{40} value for the full Monte Carlo analysis (ALL) is 147.4 ± 1.2 and 112.5 ± 1.8 for stitched and not stitched data, respectively. Even if the noise is the dominant contributor, all the means are within the acceptable mean uncertainty. Therefore, the uncertainty in the means is statistically insignificant.

It is interesting to note that the order of importance of each parameter is different for the a_{40} analysis than was the case for the best-fit conic analysis. In the case of the best-fit conic constant distributions shown in Figure 7.12, the measurement noise was not a dominant contributor to the overall conic constant uncertainty. The best-fit conic constant apparently is not as sensitive to the measurement noise as the spherical aberration term.

9.2 Surface error analysis based on PSI measurement

The last step in PSI analysis is to get the residual error map. It is found by subtracting the intended surface profile of an aspheric micro lens from its generated surface profile, which is derived from the base radius and OPD measurement. The method of subtracting intended shape is followed the same approach explained in Chapter 8. Figure 9.4 shows an example of subtracting intended surface profile from generated surface profile, and subtracting best surface profile from the generated surface profile. In this illustration, we used the mean generated surface profile, averaged from the 200 generated surface profiles. Since the best fit conic constant of the averaged generated surface profile is

about -2.27 but the intended surface profile has a conic constant of -2.1 , the difference in the two error surface maps (shown in Figure 9.4) is expected. However, the difference between these error maps is very small. Quantitatively, the difference in RMS value is ~ 12 nm.

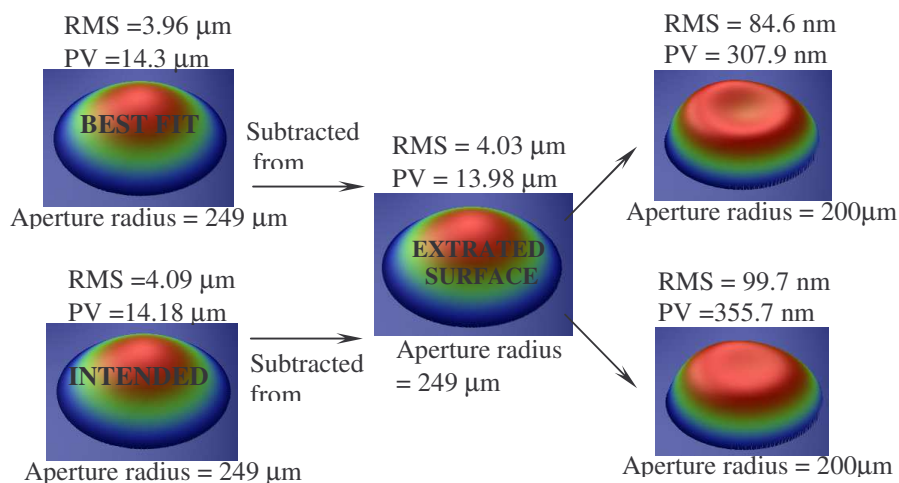


Figure 9.4 Residual surface error map of averaged generated surface profile of aspheric micro lens. The surface error as best fit subtracted from generated surface is shown at the top right. The surface error as intended subtracted from the generated surface is shown at the bottom right

The final step in our analysis is to fit the residual error maps to Zernike polynomials. Since the first sixteen Zernike coefficient terms were responsible for the generation of OPD maps from misalignment correction analysis as described in Section 7.2.3, we obtain the first sixteen Zernike coefficients after the fit to the Zernike polynomials. The result is summarized in APPENDIX I. here for our analysis we summarized only the rotationally invariant aberrations in Table VII.

The dominant aberrations among the rotationally invariant terms are defocus (a_{20}) and spherical aberration (a_{40}). This result is comparable with SWLI technique. The a_{20} term in the “intended from best fit” column is about 49 nm as compared to 50 nm in

SWLI technique of the stitched data. However, this result is from the combined effect of all the parameters and generated surface noise. To access the individual contribution to

Table VII: Mean and sigma values of the dominant aberrations. All units are in nanometers (nm).

Zernike	Intended from data		Best fit from data		Intended from best fit	
	Mean	σ	Mean	σ	Mean	σ
a_{20}	-130.4	115.9	-118.9	106.9	48.8	60.3
a_{40}	-111.6	5.3	-110.5	30.1	0.4	30.1
a_{60}	0.5	2.9	-0.6	2.9	0.1	0.4

Table VIII: Mean and sigma values of spherical aberrations due to individual parameters, and combined (All)

PSI (spherical aberration)		
	Best fit from data	
	Mean (nm)	σ (nm)
ALL	-110.5	30.1
RADIUS	-114.2	22.6
NOISE	-109.7	22.2
SAG	-111.5	20.1
APERTURE	-107.3	11.8

the over all effect of the distribution, we need to vary each parameter while keeping others at their mean values. This can be done using Monte Carlo analysis method we used in previous sections. As an example, Table VIII summarizes the spherical aberration distributions due to the three uncertainty parameters, generated surface data noise, and combined (All).

Based on Table VIII, their respective contributions can be compared as shown in Figure 9.5. As we saw it in Table VIII, the mean values seems different but as we have checked by calculating the mean uncertainty for previous analysis, we check it here and

found that all the means are within (110.5 ± 4.1) nm. It indicates that the mean value differences are statistically insignificant.

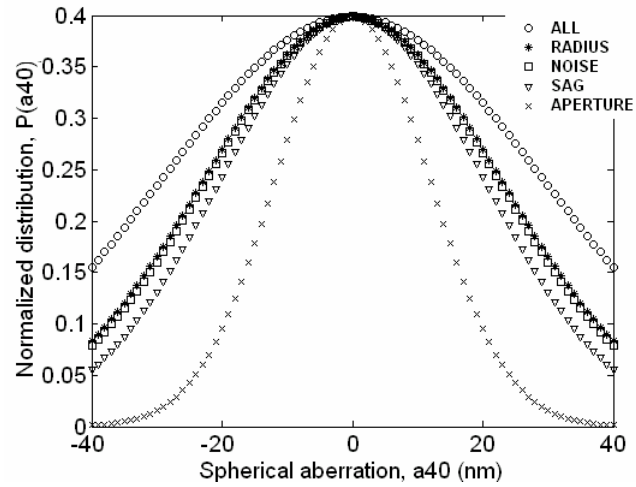


Figure 9.5: The probability distributions of spherical aberration due to individual parameters and combined (All)

10. CONCLUSIONS

We have developed a new analysis strategy with major components of determining the best-fit conic constant using chi-square minimization; estimate the uncertainty in the best-fit conic constant, and determining the aspects of the measurement that have the dominant effect on the best-fit conic constant. We used a Monte Carlo simulation to estimate a measurement uncertainty for the best-fit conic constant and to determine the dominant uncertainty contributors for the best-fit conic constant. Our new analysis strategy can be applied to any type of micro lens measurement. We illustrate the approach by obtaining data from the two major micro lens metrology techniques, SWLI and PSI. An aspheric micro lens was measured on a scanning white light interferometer using both a stitched and not stitched measurement mode, and on phase shifting interferometry. We applied our new analysis strategy procedures to the data. We extracted the surface measurement data from OPD measurement data in the case of PSI technique. We found the best-fit conic constant values -2.4 ± 0.72 and -2.0 ± 0.68 for the stitched and not stitched data, respectively. We also found -2.27 ± 0.91 for the case of PSI technique. To have a sense what we found in our analysis, the intended conic value based on the lens designer is -2.1 . In addition to a full Monte Carlo analysis where all input parameter uncertainty is considered, input parameters were individually varied to assess individual contributions to the overall uncertainty. For both the stitched and not stitched data of SWLI technique, the estimate of the base radius from the measurements has the largest impact on the overall conic constant uncertainty. In PSI technique, even though the base radius has the largest impact as SWLI technique, the noise and sag have almost comparable effect.

We also presented an alternative analysis approach to characterizing surface geometry for microlens manufacturing. Current practice focuses on determining the best-fit conic constant and we propose to alternatively look at the surface error on the lens only. The residual surface error is the difference between either the intended shape and the measured surface geometry or the best-fit conic surface and the measured surface geometry. We focused on a Zernike polynomial description of the residual surface error. Focusing on the surface error will provide stronger feedback to the manufacturing process. The analysis in both SWLI and PSI techniques shows that the residual surface error is dominated by power and spherical aberration terms, indicating that the actual lens shape is not a perfect conic, but rather a general aspheric. The Monte Carlo analysis yields uncertainties for the Zernike coefficients of the residual error map. Interestingly in SWLI technique, the relative contributions of each input uncertainty to the final uncertainty for the Zernike coefficients does not follow what we find for the contributions in the best-fit conic constant analysis. As an example, the uncertainty in the a_{40} is dominated by the measurement noise, unlike the uncertainty in the best-fit conic constant that was dominated by the base radius uncertainty. The residual spherical aberration appears to be very sensitive to the measurement noise. In PSI technique, the individual contributions in both best-fit conic constant and residual analysis follow the same trend.

As a tool to our new analysis strategy, we developed a comprehensive misalignment simulation code, which allows as generating the OPD map for aspheric surfaces misaligned in both transnational and rotational during the measurement. We also developed a code, which does the PSI analysis to extract the aspheric surface profile

measurement. Furthermore, we wrote a code that used for Monte Carlo analysis. All the main codes are found in the appendices.

In general, our new analysis shows that all results are comparable and overlaps within the combined uncertainty found in both techniques. This will assure that with proper analysis, different techniques of measurement should give the same result for the same micro lens. In addition to these the difference of the best fit conic constant from the intended and the Zernike coefficients of residual surface error are indications of the aspheric micro lens performance and process variations in the manufacturing. Since we have a lot of information from our new analysis strategy, feedback to the manufacturing process can be investigated.

REFERENCES

1. Born M., and Wolf, E., 1980, Principle of optics, sixth edition (Oxford: Pergamon), pp 110-113
2. Rudolf Kingslake, "Lens design fundamentals" 1978.
3. H. P. Herzig, "Micro-optics elements, systems and applications," edited by Hans Peter Herzig, reprinted 1998.
4. H. P. Herzig, "Micro-optics elements, systems and applications," edited by Hans Peter Herzig, pp. 127-150, reprinted 1998.
5. Popovic, Z.D., Sprague, R.A. and Connell, G.A.N. (1988), "Technique for monolithic fabrication of micro lens arrays," *app. Opt.* 27, No. 7, pp. 1281-1284.
6. Frank L. Pedrotti, S.J. Leno S. Pedrotti, "Introduction to optics", 2nd edition, 1992.
7. Digital Optics Corporation, private communication.
8. Wayent J.C. 1982, *Laser Focus*, May, p.65.
9. J.E. Greivenkamp and J. H. Burning, "Phase shifting interferometers," in *Optical shop testing*, D. Malacara, ed. (Wiley, 1992), pp. 501-598.
10. . S. Kino and S. S. C. Chim, "Mirau correlation microscope," *Applied Optics* **29**, 3775-3783 (1990).
11. L. Deck and P. de Groot, "High speed noncontact profiler based on scanning white light interferometry," *Applied Optics* **33**, 7334-7338 (1994).
12. J. Schmit and A. Olszak, "High precision shape measurement by white-light interferometry with real time scanner correction," *Applied Optics* **41**, 5943-5950 (2002).
13. Rufino Diaz-Urbe and Alejandro Comejo-Rodriguez, "Conic constant and paraxial radius of curvature measurements for conic surfaces", *Applied Optics*, **25** 20 (1986).
14. Solomon A. Gugsu and Angela Davies, "Monte Carlo analysis for the determination of the conic constant of an aspheric micro lens based on a scanning white light interferometric measurement, *proc. SPIE* vol. 5878, p. 92-102.
15. I.N.Bronshtein and Semendyayev, "HAND BOOK OF MATHEMATICS", reprint of the third edition, Springer-Verlag Berlin Heidelberg 1998.

16. J.M.A. Danby, "Fundamentals of celestial mechanics," Appendix A, 2nd edition, 1989.
17. Eugene Hech, Optics, third edition 1998, pp 378.
18. Born, M., and Wolf, E., 1980, Principle of optics, sixth edition (Oxford: Pergamon), pp 505
19. Daniel Malacara, 1992, Optical Shop Testing, second edition, pp 518-533
20. Daniel Malacara, 1992, Optical Shop Testing, second edition, pp 551-553
21. Daniel Malacara, 1992, Optical Shop Testing, second edition, pp 527-529
22. Creath, K., "Phase-Measurement Interferometry Techniques," progress in optics. Vol. XXVI, E. Wolf, Ed., Elsevier Science Publishers, Amsterdam, 1988, pp. 351-391.
23. J. Schwider, "Advanced evaluation techniques in Interferometry," progress in optics. Vol. XXVIII, E. Wolf, Ed., Elsevier Science Publishers, Amsterdam, 1988, pp. 273-353.
24. James C. Wyant, 'White Light interferometry'
25. K.G. Larkin, "Efficient nonlinear algorithm for envelope detection in white light interferometry"
26. J. Perina, Z. Hradil, B. Jurco, "Quantum Optics and fundamentals of physics"(Kluwer Academic Publisher, Dordrecht 1994)
27. Partrick Sandoz, Robert devillers and Arturo Plata, "Unambiguous profilometry by fringe-order identification in white-light phase-shifting interferometry", Journal of modern optics, 1997, vol. 44, No. 3, 519-534
28. Davidson M., Kaufman K., Mazor I., and Cohen F., 1987, Proceedings of the SPIE, vol. 775 (Bellingham, Washington: SPIE), p. 233.
29. Lee B. S., and Strand T C., 1990, Applied Optics, **29**, 3784
30. Kino G. S., and Chim S.C., 1990, Applied Optics, **29** 3775
31. Caber, P.J., 1993, Applied Optics, **32** 3438
32. Sandoz P., and Tribillon G., 1993, Journal of Modern Optics, **40** 1691

33. Hariharan P., and Roy M., 1995, Journal of Modern Optics, **42** 2357
34. De Groot P., and Deck L., 1995, Journal of Modern Optics, **42** 389
35. Hariharan P., and Roy M., 1994, Journal of Modern Optics, **41** 2197
36. P. de Groot, “ What is Frequency Domain Analysis ? “, 9/23/1993, R&D Technical Bulletin, www.zygo.com
37. P. de Groot, X. Colonna de Lega, J. Kramer, and M. Turzhitsky, “Determination of fringe order in white-light interference microscopy”, Applied Optics, vol. 41, No. 22, August 2002.
38. Born, M., and Wolf, E., 1980, Principle of optics, sixth edition(Oxford: Pergamon), pp 203-232
39. R. Kingslake, “The interferometer patterns due to the primary aberrations”,
40. Allen Nussbaum, “Optical system design” (© 1998 by Prentice Hall PTR), pp111
41. Charles S. Williams and Orville A. Becklund, ‘Introduction to the Optical Transfer Function”, pp 109
42. F. Zernike, “Beugungstheorie des Schneidensver-Eahrens und senier verbosserten Form, der phase nkontrastmethode,” physica, vol. 1, 1934, p.689
43. C. -J. Kim, R.R.Shannon, “catalogue of zernike polynomials,” applied optics and optical engineering, vol. 10, R.R. Shannon, J.C. Wyant (eds.), Academic, New York, 1987, chap. 4, pp. 193-233.
44. “Zernike polynomials and wavefront fitting,” D. Malacara (ed.), optical shop testing, Wiley, New York, 1978, app. 2, pp. 489-505
45. M. Born and E. Wolf, principle of optics, pergamon, New York, 1980.
46. Born, M., and Wolf, E., 1980, Principle of optics, sixth edition (Oxford: Pergamon), pp 465.
47. James Wyant and Katherine Creath, Basic Wavefront Aberration Theory for Optical Metrology”, Chapter 1.
48. Daniel Malacara, 1992, Optical Shop Testing, second edition, pp 465.
49. Robert K. Tyson, “Conversion of Zernike aberration coefficients to Seidel and higher-order power-series aberration coefficients,” optics letters, vol. 7, No.6,June 1982.

50. Solomon A. Gugsa and Angela Davies, "A Simulation package for evaluating interferometric micro apheric lens measurements, proceedings of the 2005 NSF DMII Granteses conference Scottsdale, AZ.
51. C.J. Evans, "Compensation of Errors Introduced by Nonzero Fringe Densities in Phase-shifting Interferometry," *Annals of CIRP*, vol. 42, pp. 577-780, 1993
52. R.E. Parks, C.J.Evans, P.J.Sullivan, L-Z. Shao, and B. Loucks, "Measurements of the LIGO Pathfinder Optics," *SPIE Conference Proceeding*, vol. 3134, pp. 95-111, 1997
53. D. Malacara, "Optical Shop Testing" Appendix 1, Wiley, New York, 1992.
54. G.J. Borse, "Numerical Methods with Matlab[®] A Resource for scientists and engineers," pp. 316, Boston, 1997.
55. Philip R. Benvington, "Data reduction and error analysis for physical sciences," USA, 1969.
56. D. Malacara, "Optical Shop Testing" chapter 13, Wiley, New York, 1992.

APPENDIX A: A LEAST-SQUARES MINIMIZATION AND MONTE CARLO APPROACH TO ESTIMATING THE CONIC CONSTANT AND UNCERTAINTY FOR MICROLENS MEASUREMENTS

Solomon A. Gugs

Department of Physics and Optical Science
9201 University City Blvd., Charlotte, NC 28223-0001

Angela Davies

Department of Physics and Optical Science
9201 University City Blvd., Charlotte, NC 28223-0001

Abstract: The ability to accurately characterize physical attributes of an aspheric microlens is crucial to understanding and improving processing in micro-optic manufacturing. Since most microlenses are plano-convex, where the convex geometry is a conic surface, current procedure is limited to obtaining an estimate of the lens' conic constant, averaging out the surface irregularities to get a best-fit conic surface. The results are later used to evaluate processing output. A standardized process of determining the best-fit conic is lacking in addition to a method of estimating the uncertainty. We have developed an approach for determining the conic constant plus associated uncertainty that is both reliable and applicable to the two most dominant microlens metrology methods in use today, namely, scanning white light interferometry (SWLI) and phase shifting interferometry (PSI). Our procedure uses least squares minimization to extract a best-fit conic value, which is then subjected to a Monte Carlo analysis to capture combined uncertainty.

1. Introduction: While microlenses in general have become important components in many technologies such as tele- and data-communication devices, optical data storage, and detector arrays, microlenses with a conic surface geometry are especially useful in today's micro-optic applications. A single refracting conic surface such as a hyperboloid with a specific conic constant whose value depends on the refractive index, corrects on-axis spherical aberration and perfectly images collimated light on axis [1]. This functionality is commonly used to couple light into and out of optical fibers. Thus many microlens design specifications require a conic surface geometry with a specific conic constant. While conic tolerances do vary

with application, they can approach ± 0.3 in demanding applications [2]. Further, one must expect that new or improved applications will drive tolerances lower, particularly as manufacturers move to passive rather than active alignment processes in an effort to reduce cost. Ideally, in-house metrology should provide a conic measurement of a microlens and an associated measurement uncertainty that is an order of magnitude lower than the tolerance. This would assure compliance of the end product, while reducing the number of situations where the characterization of the microlens itself becomes a bottleneck in the manufacturing process.

There are two interferometry-based technologies which are commonly used to characterize microlens geometry, namely phase shifting interferometry (PSI) [3] and scanning white light interferometry (SWLI) [4-6]. In some cases, instrument software can extract a best fit conic constant, but the analysis is usually proprietary, making it difficult for the lens manufacturer to assess measurement uncertainty. An alternative for extracting the conic is discussed in the literature [7], but the proposed method is not applicable to microlenses, nor is it applicable to interferometric measurements. As a consequence, manufacturers are obliged to spend capital developing their own proprietary data analysis methods. Our goal is a non-proprietary, comprehensive, procedure for estimating best-fit conic and uncertainty that can be utilized by both microlens manufacturers and customers alike. While the analysis is somewhat time-consuming and not recommended for high-volume routine inspection, it is valuable for less frequent detailed assessments for quality control. Our analysis yields a comprehensive estimate of

uncertainty and can be used to validate in-house high-speed/high volume conic estimate methods.

Our procedure employs least squares minimization to extract a best-fit conic value, which is then subjected to a Monte Carlo analysis to capture combined uncertainty. First we obtain the surface height profile data which is directly captured in SWLI, and can be generated from PSI by combining measures of the optical path difference (OPD) with a radius of curvature. Once the profile data is determined, we use estimates of the base radius of curvature and the lens aperture to generate a model conic surface for which only the conic constant remains an unknown fit parameter. Based on measurement uncertainties, appropriate probability distributions are selected for the model parameters, and a Monte Carlo process is used to iterate the minimization and to produce a final distribution of best-fit conic constants. A collection of repeated measurements are incorporated into the Monte Carlo simulation to capture uncertainty due to measurement noise. The mean of the output conic distribution then becomes a good estimate of the best-fit conic and the width an estimate of the combined uncertainty. The simulation can be repeated with uncertainty contributors varied one at a time. This provides needed and heretofore unavailable insight into measurement aspects that most affect the combined conic uncertainty. In this paper, we describe our approach in the context of application to SWLI and PSI measurements of a sample microlens.

2. The Sample Microlens: The surface of a general aspheric microlens can be represented by a conic and an even-order polynomial [8],

$$z(k, \rho, R, A_i) = \frac{-\rho^2}{R} \frac{1}{1 + \sqrt{1 - (1+k)\frac{\rho^2}{R^2}}} - A_1\rho^4 - A_2\rho^6 - \dots \quad (1)$$

where z is the surface height, k is the conic constant, $\rho = \sqrt{x^2 + y^2}$ is the aperture coordinate, R is the base radius of curvature, and the A_i 's are the deformation constants. The equation describes a conic surface when all deformation constants are zero. The design specifications for our sample conic microlens are a conic constant, $k = -2.1$, a base radius of curvature, $R = 1375 \mu\text{m}$, and a clear aperture diameter of $800\mu\text{m}$ [2].

3. Generating the Surface Profile: The first step of the analysis is to generate the surface profile from the measurement data. SWLI and PSI are the most common techniques for characterizing the surface profile of a microlens. Details of the methods can be found in the literature [9-16].

We demonstrate the application to SWLI measurements with data taken with a NewView™ 5000 SWLI. Scanning white light interferometers are also known as optical profilers and yield a direct estimate of the height profile of a surface. We used a 10x Mirau interferometric objective, a spatial sampling of $2.2 \mu\text{m}$ (320×240), and a system magnification of 2, which generated an observable pixel size of $1.103 \mu\text{m}$ as read from the calibrated instrument. Measurements can be taken in either of two ways, a single measurement taken at the apex of the lens or a collection of measurements taken using the stitching mode. SWLI instruments are limited in the surface slopes that can be measured. If the slope is too high, light does not reflect back into the objective. We used the stitching measurement mode whereby a higher NA objective can be used to capture steeper slopes, and to compensate, smaller area measurements are then taken as the lens is translated under the objective and stitched together for a final result. Even so, only the region near the apex of the lens is measured. A sample measurement is shown in Figure 1.

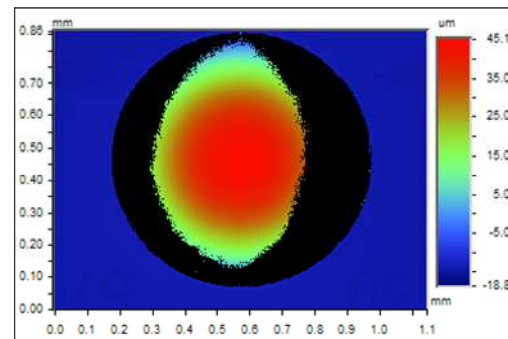


Fig. 1: One of the SWLI measurements of the microlens surface profile.

It is important to take a collection of measurements to allow measurement noise to be included in the final uncertainty. We took a total of 11 stitched measurements. We repositioned and rotated the lens between the measurements to capture reproducibility. The images were

rotated back to the same orientation for the remaining analysis (made possible by a fiducial near the lens edge). We define the axis of the microlens to be perpendicular to the plane of the substrate, therefore the substrate region is aligned perpendicular to the optical axis of the instrument for data acquisition. Residual tip and tilt misalignment was removed with Vision® 32 software.

We take only the data from the apex region of the lens (central portion in Figure 1). To complete the generate of the height profile, we estimate the sag of the lens from the measurements to define the height of the data above the substrate plane. Among the collection of 11 measurements we estimate a mean sag of $57.7 \mu\text{m}$ with an uncertainty (standard deviation) of ± 0.7 . We also need to define the x, y (plane of the substrate) location of the lens center. We take this to be the center of a circular mask fit to the data drop-out boundary at the edge of the lens (see Figure 1) and estimate an uncertainty of a fraction of a pixel on average, $\pm 0.63 \mu\text{m}$.

For the SWLI height profile generation, the dominant uncertainty contributors are noise in the measurements themselves (e.g. from turbulence, vibration, and source and detector noise) and estimation of the sag. Calibration of the instrument in x, y (plane of substrate), and z contributes uncertainty, but these contributions are small compared to the sources. For example, the calibration uncertainty for z is $\pm 0.26\%$, leading to an uncertainty of $0.1 \mu\text{m}$ for a sag of $57.7 \mu\text{m}$, whereas the measurement noise leads to a sag uncertainty of $0.7 \mu\text{m}$. Therefore, calibration uncertainty can be ignored. The estimated one-pixel variation in the lens center definition is negligible.

Generating the profile estimate from the PSI measurement is more involved. We use a Fisba Optik $\mu\text{phase}^{\circledR}$ interferometer with a numerical aperture of 0.34 and a spatial sampling of $2.285 \mu\text{m}$ (512×512) for the PSI measurements. The Fisba Optik is a Twyman-Green configuration and measures the optical path difference (OPD) for the lens surface from wave front phase information [8, 17-21]. The OPD map must be combined with the profile of a sphere to generate the lens surface profile. The Fisba uses a Heidenhain displacement gauge to measure (equivalently) z -position changes of the microlens. This allows the microlens radius to

be measured. A height profile is generated by adding the OPD data to a spherical surface with the radius determined from a radius measurement. The OPD represents the departure of the surface from a best fit sphere in the radial direction [22, 23]. We approximate this by adding the OPD in the z direction, which involves a cosine approximation. This introduces an error that is small compared to our measurement noise and does not affect our result. But, this approximation should be avoided for lower noise applications. We took a total of 15 OPD measurements to capture measurement noise for our uncertainty evaluation. A calibration map is subtracted from each measurement to remove the interferometer bias. The calibration is determined by carrying out a random ball test [24, 25]. One of the OPD measurements is shown in Figure 2.

The radius is measured on the Fisba following the procedure described in reference 26. In short, the radius is the distance the lens is translated between the cat's eye and confocal positions (technically the interferometer is translated in the Fisba, but the effect is the same). The two positions are determined by collecting a series of measurements around the confocal and cat's eye positions and using the curvature in the measured wavefront to interpolate to the two best null positions. An uncertainty can be estimated as the standard deviation observed when the measurement is repeated several times. We followed a more involved process whereby we estimated an uncertainty for the interpolation process, which is influenced by the uncertainty in the wavefront curvature measurements and the Heidenhain gauge uncertainty. The details of the analysis are beyond the scope of this paper and will be published elsewhere [25]. In summary, we estimate a radius of $1366 \mu\text{m} \pm 17 \mu\text{m}$. This radius measurement yields an estimate of the radius of a best-fit sphere to the lens surface over the aperture of the OPD measurement. Note that this is not the same as the base radius for an aspheric lens. This is however the correct radius to use to build the surface profile in the manner described.

The numerical aperture of the OPD measurement must be known in order to add the OPD data to the spherical data. Recall that the OPD is a measure of the surface departure from a best-fit sphere, taken with the lens positioned so the center of curvature coincides with the focus of

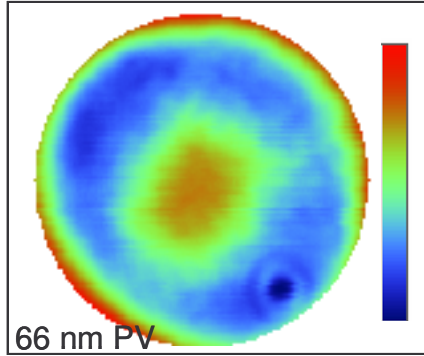


Fig. 2: One of the PSI measurements of the microlens.

light from the interferometer. The NA defines the solid angle of the OPD measurement at confocal. Thus the NA of the measurement defines the $\sin\theta$ of the lens geometry, as shown in Figure 3. The NA will be lower than the NA of the interferometer objective if the cone of light overfills the lens and/or the data is masked. From our masking and objective NA information, we estimate a cone angle of $10.6^\circ \pm 1^\circ$. The equation that defines the aperture from the geometry is $\rho_{\max} = R \sin\Theta$. An angle of 10.6° and a radius of 1366 mm gives $\rho_{\max} = 251.4 \mu\text{m}$. Error propagation gives an uncertainty estimate of $\pm 3.4 \mu\text{m}$ for ρ_{\max} .

This aperture is less than the full aperture of the microlens (full aperture $\sim 400 \mu\text{m}$). One advantage of PSI compared to SWLI is that the entire surface of the lens can be measured, as long as the NA of the interferometer is large enough so wave front overfills the lens. The NA for our measurements is large enough to measure the entire surface, but we masked our data down so the aperture matches the largest circular patch measured by the SWLI. In this way we can compare PSI to SWLI for measurements of the same lens region. In general, however, the full

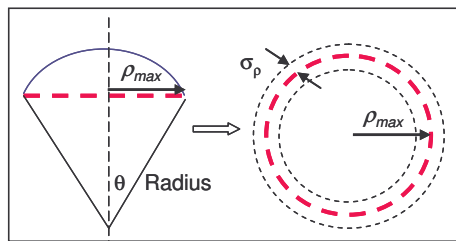


Fig. 3: Geometric relationship between aperture radius ρ_{\max} , radius of microlens and angle θ .

surface geometry should be used for the PSI analysis. Using this subaperture does not mathematically effect the conic constant.

PSI surface geometry measurements are susceptible to artifacts if the lens is not well nulled for the measurement [27]. Well nulled means the focus of light from the interferometer is coincident with the center of curvature of the lens. It is not mechanically possible to position the lens perfectly thus some artifacts are always present. The artifacts are observed as high order aberrations that increase with misalignment. The correlation can be observed by plotting the higher order Zernike coefficients versus the low order coefficients that represent misalignment (corresponding to tip tilt and power). For example one will observe an approximately linear relationship between the A_2^0 (power) coefficient and the A_4^0 (low order spherical aberration) coefficient [25]. The slope from a linear fit to each curve estimates the correlation. These plots are referred to as alignment sensitivity plots. Although the microlens is nulled as well as possible for each of the 15 measurements, residual misalignment provides us with enough data to generate the alignment sensitivity plots. The aberrations up to second order spherical are included in our analysis. The average Zernike tip, tilt and power among our 15 measurements are approximately zero, but the standard deviation shows the likelihood for a single measurement to be misaligned. These tip tilt and power standard deviations are multiplied by the sensitivity curve slopes for an uncertainty estimate for each higher order Zernike coefficient (up to second order spherical). These uncertainties are used in the Monte Carlo simulation.

To summarize, the dominant uncertainty contributors for PSI height profiles are noise in the measurement, estimation of the best-fit sphere radius, estimation of the aperture, and aberrations due to misalignment.

4. Building the Conic Surface Model: The next step is to build a conic model, leaving only the conic constant k as an unknown parameter to be determined from the χ^2 minimization. The parameters needed are the base radius of curvature and the aperture radius. Mathematically, the base radius of a conic surface is the same as the radius of a sphere at the vertex, i.e., the sphere for $k = 0$ (R in

Equation 1). This is not the same radius as used for the PSI profile generation. The aperture radius is the radius of the lens footprint, referred to as ρ_{max} . Both parameters are depicted in Figure 4. Note that the vertical scale in the plot is much larger than the horizontal scale.

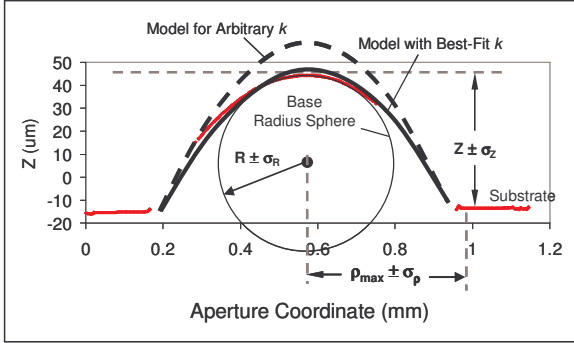


Fig. 4: Two dimensional profile of a measurement, the best-fit conic model, and a model generated with an arbitrary k . The parameters used to generate the model are the base radius R , and the aperture radius ρ_{max} .

For the SWLI measurements, we approximately estimate the base radius with a sequential masking process. We subsequently masked down our surface profile data incrementally to a level of 5% of the lens surface about the apex. That is, the stitched data was masked down starting from 100% to 5% at a step of 5%. A best-fit sphere is fit to each of the masked down images using Vision® 32 software to compute the radius. The masking process was repeated for each of the 11 measurements. The mean values are plotted in Figure 5 as a function of mask diameter and the standard deviations are shown as error bars. The analysis shows an increase in the radius below an aperture size of approximately 300 μm , suggesting an estimate for R of 1.5 mm. However, tests we carried out with simulated data showed that the radius for small apertures becomes extremely sensitive to noise and is misleading below a mask diameter of $\sim 300 \mu\text{m}$. Therefore we used the values at a mask diameter of 300 μm as our estimate, giving $R = 1.36 \text{ mm} \pm 20 \text{ mm}$.

The aperture radius of the microlens cannot be directly measured in SWLI because no data is obtained from the steep edges of the lens. Thus we have to make an assumption about the lens surface in this region. We assume the surface continues smoothly from where the data drop out begins to the measured edge of the flat substrate (see Figure 1). We fit a circular mask to this

edge and use the radius as our aperture radius estimate. We repeat this process for all measurements and calculate a mean radius of 400 μm and an uncertainty of 2.42 μm . Note that this uncertainty could be expanded to capture possible lens geometry variation in the data drop out region. Profilometry measurements could be used to investigate this in detail.

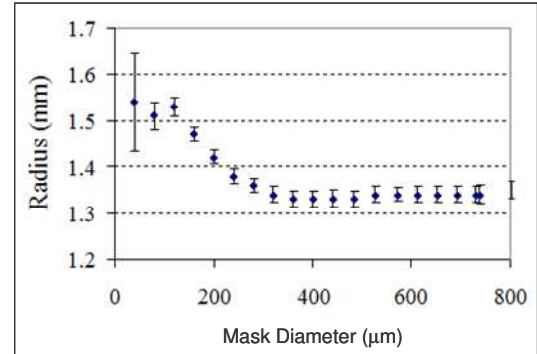


Fig. 5: Best-fit sphere radius versus aperture diameter (masked data).

A base radius and aperture must be estimated from the PSI measurements, as well. Using the Fisba, we directly measure the radius of the best-fit sphere over the aperture of the OPD measurement. This is not the same as the base radius for a conic surface. One could estimate the base radius by carrying out the same sequential masking process as was done with the SWLI profile data. Also, the base radius can be estimated from as a correction to the best-sphere radius from knowledge of the higher order aberrations observed in the OPD maps. We took the later approach. The first step is to calculate the Seidel focus description of the OPD map. This is given by a linear combination of Zernike coefficients [32, 33],

$$W(\rho)_{focus}^{seidel} = \left(-6A_4^0 + \sqrt{(A_2^2)^2 + (A_2^{-2})^2} \right) \rho^2 \quad (6)$$

where A_4^0 , A_2^2 , and A_2^{-2} are the measured Zernike coefficients for low order spherical aberration, 0° astigmatism and 45° astigmatism, respectively. From the average Zernike coefficients, Equation 6 gives a coefficient for the Seidel focus term of 0.2 μm (quantity in parenthesis). This represents curvature in the wavefront in the paraxial limit (in the region near the optical axis). This is the curvature information of interest to determine the radius of the lens near the apex. We can convert the 0.2

μm curvature to an approximate distance the microlens would have to be moved to null out this curvature. This is the radius correction value we are after. We can determine this distance with the interpolation information used to determine the two null positions for cat's eye and confocal in the radius measurement. The correction value is $\sim 0.7 \mu\text{m}$. This is small compared to the $17\mu\text{m}$ uncertainty we estimate for the best-fit sphere R value, therefore we can use this value to approximate the base radius for the model with our level uncertainty. The details of this analysis are described elsewhere [ref Solomon]. The correction would have to be made for lower noise applications.

The aperture radius needed for the model is the same value needed for the surface profile generation from PSI data. We use the same estimate, namely $\rho_{\text{max}} = 251.4 \mu\text{m} \pm 3.4 \mu\text{m}$.

5. χ^2 Minimization and the Monte Carlo Simulation: A conic surface is uniquely defined with a base radius, aperture diameter and conic value. At this point, we have estimated the base radius and aperture diameter for the model, leaving only the conic parameter as unknown. We have also generated a surface profile from the measurement to compare to the model. The next step is to carry out a one-parameter χ^2 minimization to determine the best-fit conic value with

$$\chi^2 = \sum_{i=1}^N ((z_m)_i - (z_s)_i)^2 \quad (2)$$

where z_m is the model value at each $x_i y_i$ coordinate (calculated from Equation 1), and z_s are the corresponding height values from the profile data. Figure 4 shows a SWLI data profile with the best-fit k compared to a model generated with an arbitrary k . With a fixed base radius and aperture diameter, the model sag is defined by k . The best-fit k yields the model with the best sag agreement with the data (the solid smooth line in the plot).

The χ^2 minimization is carried out for a specific measurement profile and model parameters R and ρ_{max} , as summarized by Figure 4. A single χ^2 minimization does not show the possible variation in k due to uncertainties. We can estimate the uncertainty by repeating the minimization while statistically sampling all of the likely values for the model parameters and profile data. The likely values are defined by the

uncertainties estimated from the measurements. To do this, we define Gaussian probability distributions for the model parameters, R and ρ_{max} , each with the appropriate mean and σ . The values used for SWLI are $R = 1360 \mu\text{m} \pm 20 \mu\text{m}$ and $\rho_{\text{max}} = 400.0 \mu\text{m} \pm 2.4 \mu\text{m}$ and the values for PSI are $R = 1366 \mu\text{m} \pm 17 \mu\text{m}$ and $\rho_{\text{max}} = 251.4 \mu\text{m} \pm 3.4 \mu\text{m}$. We randomly pick an R and ρ_{max} from the Gaussian distributions for each iteration (each χ^2 minimization). We also randomly select a data profile for each iteration to capture uncertainty in the measured profile. This step is measurement specific.

For SWLI measurements, profile uncertainty sources are measurement noise, the lens center location, and the sag value. For PSI, uncertainty sources are measurement noise (including misalignment errors), radius, and aperture (defined by the NA). For SWLI, we generate a profile by randomly picking one of the 11 measurements, and then using a randomly chosen sag and a lens center value from Gaussian distributions defined by the appropriate mean and uncertainty for each. The values for the sag distribution are $57.7 \mu\text{m} \pm 0.7 \mu\text{m}$ and lens center distribution $0 \pm 0.6 \mu\text{m}$.

For PSI, we generate a profile by randomly picking one of the 15 OPD measurements and using a randomly chosen radius and aperture value from appropriately defined Gaussian distributions. The values for the radius distribution are $1366 \mu\text{m} \pm 17 \mu\text{m}$ and $251.4 \pm 3.4 \mu\text{m}$ for the aperture distribution. We then add small high-order aberration corrections to the OPD map to represent misalignment uncertainty. We do this by randomly picking a tip, tilt, and power from Gaussian distributions based on the standard deviations observed among the 15 measurements. We then multiply the tip, tilt, and power by the sensitivity curve slopes discussed above. This results in a set of correction coefficients for the high order Zernike for the OPD map. These coefficients are multiplied by the corresponding Zernike polynomial and this is then added to the OPD map. This is the OPD map that is added to the best-fit sphere for the measurement profile.

The Monte Carlo simulation is iterated 200 times. The approach assumes uncertainty sources are uncorrelated, and this may not be rigorously true (for example measurement noise may impact the radius value). But, likely any correlation has a

smaller effect on the final k distribution than the individual contributions. The Monte Carlo approach is also useful because individual contributions can be investigated one at a time to assess relative importance. That is, all uncertainty contributions can be fixed and only one aspect allowed to vary at a time. Differences in the output k distributions are then a good indicator of measurement aspects limiting the final k uncertainty. Only 50 iterations were used for these studies.

6. Results and Discussion: The results of our complete Monte Carlo simulation are shown in Figure 6. For SWLI, the mean k value is -2.4 and the standard deviation is $0.7 \mu\text{m}$ (part (a)). For the PSI measurements the mean is -2.3 and the standard deviation is $0.9 \mu\text{m}$. Thus, the design conic value of -2.1 for the lens falls within the range of possible k values suggested from our analysis. The analysis shows that current levels of measurement uncertainty will not allow us to evaluate conic conformance at a level below ± 0.7 at best.

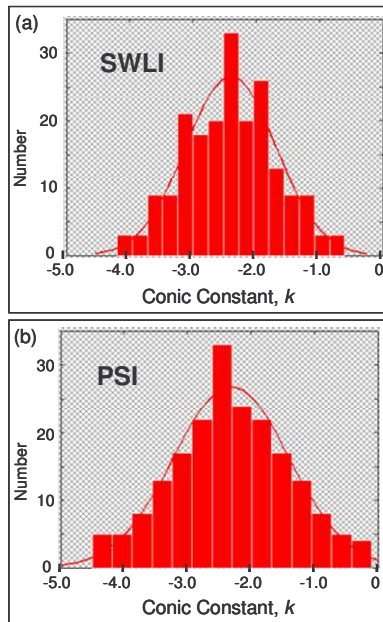


Fig. 6: The probability distributions for k from the Monte Carlo simulation. The mean best-fit conic constant of the SWLI and PSI are $k = -2.4 \pm 0.7$ and $k = -2.3 \pm 0.9$.

The simulation result for individual contributions is summarized in Table 1 and Figure 7. The table lists the mean and σ values for the k distributions when uncertainty sources

are varied one at a time. The variation in the mean is not statistically significant, taking the uncertainty in the mean as σ/\sqrt{N} . The distribution widths are the important quantities to compare. For a visual comparison of the widths,

	SWLI		PSI	
	Mean	σ	Mean	σ
All	-2.44	0.72	-2.27	0.91
Radius	-2.44	0.55	-2.39	0.71
Sag	-2.36	0.47	-	-
Noise	-2.49	0.29	-2.29	0.68
Aperture	-2.35	0.26	-2.21	0.38
Center	-2.37	0.00	-	-

we generate a Gaussian fit to $k - k_{mean}$ for each distribution. These distributions are compared in Figure 7. The analysis shows that the radius and the sag dominate the combined k uncertainty for SWLI measurements. The radius and measurement noise dominate the uncertainty for the PSI measurements. Note that the conic value is very sensitive to the radius value. Variations in R of $\sim 1\%$ lead to 20% variation in k .

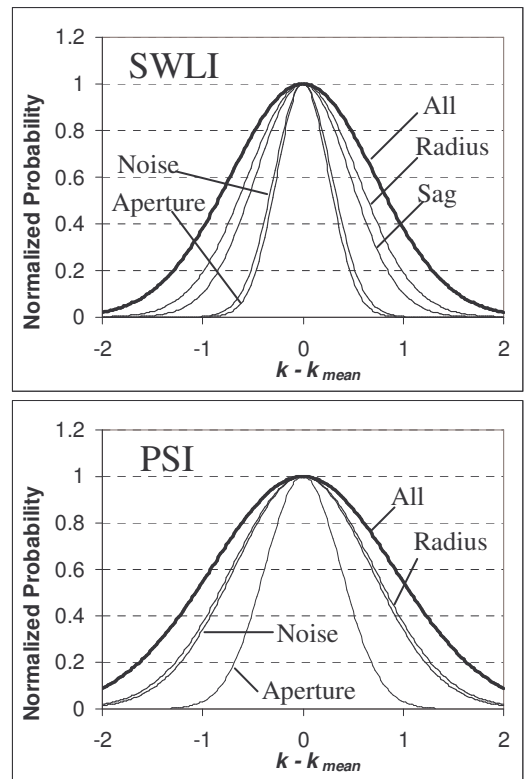


Fig. 7: The $k - k_{mean}$ distributions where uncertainty contributors are varied one at a time. (a) Results for

the SWLI measurements. (b) Results for the PSI measurements.

7. Conclusions: We have devised and documented a new procedure for analyzing data from microlens geometry measurements that is applicable to any type of microlens measurement. We illustrate the approach by applying it data from the two major microlens metrology techniques, SWLI and PSI. The major components of our analysis are (1) determine the best-fit conic constant for a microlens using chi square minimization, (2) estimate the uncertainty in the best-fit conic constant using a Monte Carlo simulation, and (3) use a Monte Carlo simulation to determine the aspects of the measurement that have the greatest effect on the best-fit conic constant.

8. Acknowledgements: This material is based upon work supported by the National Science Foundation under Grant No. 0323505. Any opinions, findings, and conclusions or recommendations expressed in this material are those of the authors and do not necessarily reflect the views of the National Science Foundation. The authors would also like to thank Mark Boomgarden and Chris Linnen from Digital Optics Corporation, and Tom Suleski from UNC Charlotte.

7. References:

- [1] Frank L. Pedrotti, S.J. Leno S. Pedrotti, "Introduction to optics", 2nd edition, 1992.
- [2] Digital Optics Corporation, private communication.
- [3] J.E. Greivenkamp and J. H. Burning, "Phase shifting interferometers," in *Optical shop testing*, D. Malacara, ed. (Wiley, 1992), pp. 501-598.
- [4] G. S. Kino and S. S. C. Chim, "Mirau correlation microscope," *Applied Optics* **29**, 3775-3783 (1990).
- [5] L. Deck and P. de Groot, "High speed noncontact profiler based on scanning white light interferometry," *Applied Optics* **33**, 7334-7338 (1994).
- [6] J. Schmit and A. Olszak, "High precision shape measurement by white-light interferometry with real time scanner correction," *Applied Optics* **41**, 5943-5950 (2002).
- [7] Rufino Diaz-Urbe and Alejandro Comejo-Rodriguez, "Conic constant and paraxial radius of curvature measurements for conic surfaces", *Applied Optics*, **25** 20 (1986).
- [8] D. Malacara, "Optical Shop Testing" Chapter 13, Wiley, New York, 1992.
- [9] Davidson M., Kaufman K., Mazor I., and Cohen F., *Proceedings of the SPIE*, **775** (Bellingham, Washington: SPIE), p. 233 (1987).
- [10] Lee B. S., and Strand T C., 1990, *Applied Optics*, **29**, 3784
- [11] Kino G. S., and Chim S.C., *Applied Optics*, **29** 3775 (1990).
- [12] Caber, P.J., *Applied Optics*, **32** 3438 (1993).
- [13] Sandoz P., and Tribillon G., *Journal of Modern Optics*, **40** 1691 (1993).
- [14] Hariharan P., and Roy M., *Journal of Modern Optics*, **42** 2357 (1995).
- [15] De Groot P., and Deck L., *Journal of Modern Optics*, **42** 389 (1995).
- [16] Hariharan P., and Roy M., *Journal of Modern Optics*, **41** 2197 (1994).
- [17] Gallagher, J. E. and D. R. Herriott, "Wavefront Measurement." U. S. Patent 3, 694,088 (1972/1972).
- [18] Burning, J. H., D. R. Herriott, J. E. Gallagher, D. P. Rosenfeld, A. D. White, and D. J. Brangaccio, "Digital Wavefront Measuring Interferometer for Testing Optical Surfaces and Lenses," *Appl. Opt.*, **13**, 2693 (1974).
- [19] Greivenkamp, J. E., "Interferometric Measurements at Eastman Kodak Company," *Proc. SPIE*, **816**, 212 (1987a).
- [20] Carre, P. "Installation et Utilisation du Comparateur Photoelectrique et Interferentiel du Bureau International des Poids de Mesures," *Metrologia* **2**, 13 (1966).
- [21] Hariharan, P. B. F. Oreb, and T. Eiju, "Digital Phase-Shifting Interferometry: A simple

Error-Compensating Phase Calculation Algorithm," *Appl. Opt.*, 26, 2504 (1987a).

[22] D. Malacara and S. L. DeVore, "Interferogram Evaluation and Wavefront Fitting," in *Optical Shop Testing*, D. Malacara, Ed. Wiley, New York, 1992.

[23] D. Malacara, "Optical Shop Testing" Appendix 1, Wiley, New York, (1992).

[24] "Self-calibration for Micro-refractive Lens Measurements." N. Gardner and A. Davies, *Optical Engineering*, 45 (3), (2006).

[25] S. Gugsu, "New Analysis Strategies for Micro Aspheric Lens Metrology," Ph. D. Dissertation, Department of Physics and Optical Science, UNC Charlotte, to be submitted June 2006.

[26] T. L. Schmitz, A. Davies, and C. J. Evans, "Uncertainties in interferometric measurements of radius of curvature." SPIE Conference Proceedings, SPIE's 46th Annual International Symposium on Optical Science and Technology, July (2001).

[27] C. J. Evans, "Compensation of Errors Introduced by Nonzero Fringe Densities in Phase-shifting Interferometry," *Annals of the CIRP*, **42**, pp. 577-780, 1993.

[28] Robert K. Tyson, "Conversion of Zernike aberration coefficients to Seidel and higher-order power-series aberration coefficients," *Optics Letters*, **7**, No. 6, June 1982

APPENDIX B: A MONTE CARLO ANALYSIS OF SURFACE ERRORS FOR ASPHERIC MICROLENS MANUFACTURING

Solomon A. Guga

Department of Physics and Optical Science
9201 University City Blvd., Charlotte, NC 28223-0001

Angela Davies

Department of Physics and Optical Science
9201 University City Blvd., Charlotte, NC 28223-0001

Abstract: The ability to accurately characterize physical attributes of an aspheric microlens is crucial to understanding and improving processing in micro-optic manufacturing. Since most microlenses are plano-convex, where the convex geometry is a conic surface, current practice focuses on estimating the manufactured lens' conic constant, which ignores the surface geometry that departs from an exact conic surface. The best-fit conic is later used to evaluate processing output. We propose an alternative analysis that focuses on the surface errors, rather than the best-fit conic constant. We consider the surface errors as the difference between the measured geometry and the best-fit conic surface or as the difference between the measured geometry and the design specification for the lens. A complete uncertainty assessment is an important part of our approach. We estimate uncertainties for several parameters from the measurement and then carry out a Monte Carlo simulation to estimate the resulting variation in the surface error. We focus on a Zernike polynomial description of the surface error, and the Monte Carlo analysis yields a combined uncertainty for each Zernike coefficient. We describe our approach as applied to the two most dominant microlens metrology methods in use today, namely, scanning white light interferometry (SWLI) and phase shifting interferometry (PSI).

1. Introduction: While microlenses in general have become important components in many technologies such as tele- and data-communication devices, optical data storage, and detector arrays, microlenses with a conic surface geometry are especially useful in today's micro-optic applications. A single refracting conic surface such as a hyperboloid with a specific conic constant whose value depends on the refractive index, corrects on-axis spherical

aberration and perfectly images collimated light on axis [1]. This functionality is commonly used to couple light into and out of optical fibers. Thus many microlens design specifications require a conic surface geometry with a specific conic constant. While conic tolerances do vary with application, they can approach ± 0.3 in demanding applications [2]. Further, one must expect that new or improved applications will drive tolerances lower, particularly as manufacturers move to passive rather than active alignment processes in an effort to reduce cost. The conic is a key design parameter, consequently microlens characterization to date focuses on estimating the best-fit conic for the manufactured lens. The lens however, is not likely to be a perfect conic therefore the departure from an exact conic is not captured. Further the best-fit conic does not directly reflect the errors in the manufactured part, i.e. the difference between the surface geometry and the design specification. The current approach is convenient for assessing part performance and tolerance compliance, but the connection to problems with the manufacturing process is less direct. A strong connection between measurement output and process parameters is critical for effective process feedback and control.

In this paper we describe a new analysis strategy for microlens manufacturing. We propose to focus on the *surface errors*, rather than the best-fit conic constant. In order to connect the new analysis with current practice, we consider the surface errors as either (i) the difference between the measured geometry and the *best-fit conic surface* or as (ii) the difference between the measured geometry and the *design specification* for the lens. In either case, we consider a Zernike polynomial description of the surface error map [3] as the final output. A complete

uncertainty assessment is an important part of our approach. We estimate uncertainties for several parameters from the measurement and then carry out a Monte Carlo simulation to estimate the resulting combined uncertainty in the surface error map and therefore a combined uncertainty for each Zernike coefficient.

We describe our analysis through an illustration with a representative aspheric microlens. We measured the lens using both scanning white light interferometry (SWLI) [4-6] and phase shifting interferometry (PSI) [7], which are the two dominant metrology techniques used in microlens manufacturing. The first step is to measure the lens and estimate measurement uncertainties. This information is then used in a Monte Carlo simulation as shown schematically in Figure 1. For each iteration through the Monte Carlo loop, we first generate an estimate of the surface profile from the measurement data. Each iteration through the Monte Carlo loop, we first generate an estimate of the surface profile from the measurement. This estimate includes appropriately chosen randomly variables to capture the affect of measurement uncertainty. These details depend on the measurement type (PSI or SWLI). Once a representative estimate of the surface profile is generated, the surface error map is calculated as either the difference from the best-fit conic surface or from the design specification (design shape). The best-fit conic surface is determined with a χ^2 minimization process, the details of which are described elsewhere [8]. The last step is to fit the surface error map to the set of Zernike polynomials [3] and store the coefficients in an array. The output of the Monte Carlo loop is a distribution for each Zernike coefficient. The mean of each distribution is an estimate of the coefficient for the surface error map and the standard deviation is an estimate of the combined uncertainty. The simulation can be repeated where only a single uncertainty source varies at a time to investigate uncertainty sensitivity to individual contributions. In the sections that follow, we describe the sample lens used for the illustration, the experimental details of the measurements and the uncertainty estimations, and the Monte Carlo simulation details, followed by the results and discussion.

2. The Sample Microlens: The surface of a general aspheric microlens can be represented by a conic and an even-order polynomial [9],

$$z(k, \rho, R, A_i) = \frac{-\rho^2}{R} + \sqrt{1 - (1+k)\frac{\rho^2}{R^2}} - A_1\rho^4 - A_2\rho^6 - \dots \quad (1)$$

where z is the surface height, k is the conic constant, $\rho = \sqrt{x^2 + y^2}$ is the aperture coordinate, R is the base radius of curvature, and the A_i 's are the deformation constants. The equation describes a conic surface when all deformation constants are zero. The design specifications for our sample conic microlens are a conic constant, $k = -2.1$, a base radius of curvature, $R = 1375 \mu\text{m}$, and a clear aperture diameter of $800\mu\text{m}$ [2].

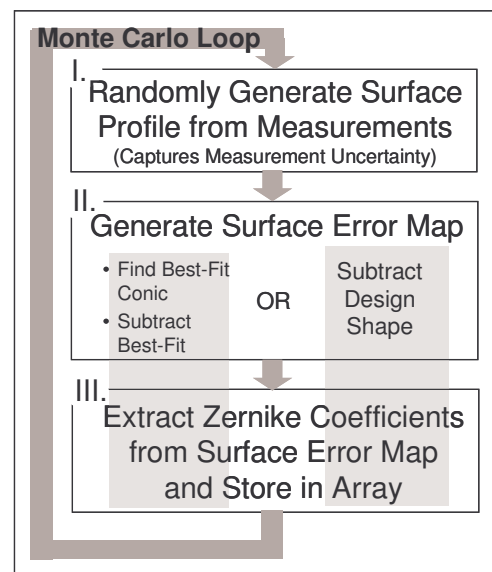


Fig. 1: Schematic of the Monte Carlo process.

3. Measurement Details and Uncertainty Estimates: In this section we describe the measurements of the sample lens with both a scanning white light interferometer (SWLI) and a phase shifting interferometer (PSI). These are the two common measurement methods used to characterize microlenses. Details of the methods can be found in the literature [10-17].

Measurements of our sample lens were taken with a NewView™ 5000 SWLI. Scanning white light interferometers are also known as optical profilers and yield a direct estimate of the height profile of a surface. We used a 10x Mirau interferometric objective, a spatial sampling of $2.2 \mu\text{m}$ (320×240), and a system magnification of 2, which generated an observable pixel size of $1.103 \mu\text{m}$ as read from the calibrated instrument. Measurements can be taken in either of two ways,

a single measurement taken at the apex of the lens or a collection of measurements taken using the stitching mode. SWLI instruments are limited in the surface slopes that can be measured. If the slope is too high, light does not reflect back into the objective. We used the stitching measurement mode whereby a higher NA objective can be used to capture steeper slopes, and to compensate, smaller area measurements are then taken as the lens is translated under the objective and stitched together for a final result. Even so, only the region near the apex of the lens is measured. A sample measurement is shown in Figure 2 (a).

It is important to take a collection of measurements to allow measurement noise to be included in the uncertainty assessment. We took a total of 11 stitched measurements. We repositioned and rotated the lens between the measurements to capture reproducibility. The images were rotated back to the same orientation for the remaining analysis (made possible by a fiducial near the lens edge). We define the axis

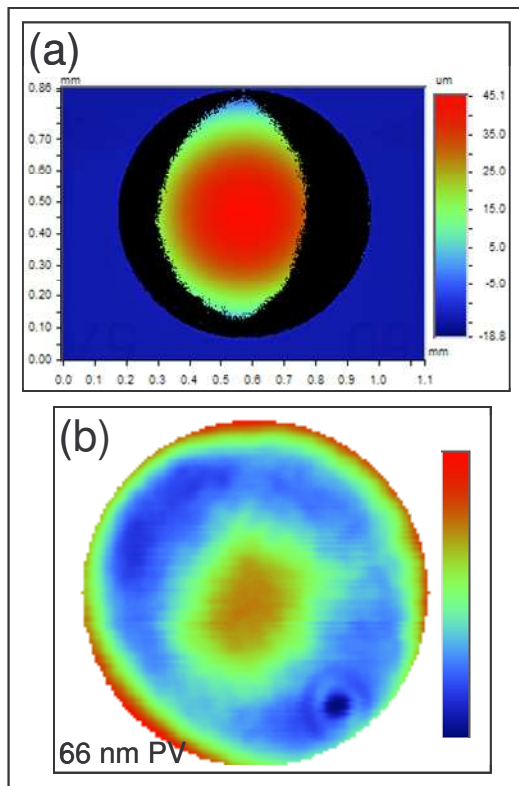


Fig. 2: Examples of measurements taken of the sample lens. (a) SWLI measurement. (b) Optical path difference map taken with the PSI.

of the microlens to be perpendicular to the plane of the substrate, therefore the substrate region is aligned perpendicular to the optical axis of the instrument for data acquisition. Residual tip and tilt misalignment was removed with Vision@ 32 software.

We take only the data from the apex region of the lens (central portion in Figure 2 (a)). To complete the generate of the height profile, we estimate the sag of the lens from the measurements to define the height of the data above the substrate plane. Among the collection of 11 measurements we estimate a mean sag of $57.7 \mu\text{m}$ with an uncertainty (standard deviation) of ± 0.7 . We also need to define the $x y$ (plane of the substrate) location of the lens center. We take this to be the center of a circular mask fit to the data drop-out boundary at the edge of the lens (see Figure 1) and estimate an uncertainty of a fraction of a pixel, $\pm 0.63 \mu\text{m}$.

For the SWLI height profile generation, the dominant uncertainty contributors are noise in the measurements themselves (e.g. from turbulence, vibration, and source and detector noise), estimation of the sag, and lens center. Calibration of the instrument in x, y (plane of substrate), and z contributes uncertainty, but these contributions are small compared to the sources. For example, the calibration uncertainty for z is $\pm 0.26\%$, leading to an uncertainty of $0.1 \mu\text{m}$ for a sag of $57.7 \mu\text{m}$, whereas the measurement noise leads to a sag uncertainty of $0.7 \mu\text{m}$. Therefore, calibration uncertainty can be ignored. The estimated one-pixel variation in the lens center definition is negligible.

Generating the profile estimate from the PSI measurement is more involved. We use a Fisba Optik $\mu\text{phase}^{\circledR}$ interferometer with a numerical aperture of 0.34 and a spatial sampling of $2.285 \mu\text{m}$ (512×512) for the PSI measurements. The Fisba Optik is a Twyman-Green configuration and measures the optical path difference (OPD) for the lens surface from wave front phase information [7, 18-22]. The OPD map must be combined with the profile of a sphere to generate the lens surface profile. The Fisba uses a Heidenhain displacement gauge to measure (equivalently) z -position changes of the microlens. This allows the microlens radius to be measured. A height profile is generated by adding the OPD data to a spherical surface with the radius determined from a radius

measurement. The OPD represents the departure of the surface from a best fit sphere in the radial direction [23, 24]. We approximate this by adding the OPD in the z direction, which involves a cosine approximation. This introduces an error that is small compared to our measurement noise and does not affect our result. But, this approximation should be avoided for lower noise applications. We took a total of 15 OPD measurements to capture measurement noise for our uncertainty evaluation. A calibration map is subtracted from each measurement to remove the interferometer bias. The calibration is determined by carrying out a random ball test [25, 26]. One of the OPD measurements is shown in Figure 2 (b).

The radius is measured on the Fisba following the procedure described in reference 27. In short, the radius is the distance the lens is translated between the cat's eye and confocal positions (technically the interferometer is translated in the Fisba, but the effect is the same). The two positions are determined by collecting a series of measurements around the confocal and cat's eye positions and using the curvature in the measured wavefront to interpolate to the two best null positions. An uncertainty can be estimated as the standard deviation observed when the measurement is repeated several times. We followed a more involved process whereby we estimated an uncertainty for the interpolation process, which is influenced by the uncertainty in the wavefront curvature measurements and the Heidenhain gauge uncertainty. The details of the analysis are beyond the scope of this paper and are described elsewhere [26]. In summary, we estimate a radius of $1366 \mu\text{m} \pm 17 \mu\text{m}$. This radius measurement yields an estimate of the radius of a best-fit sphere to the lens surface over the aperture of the OPD measurement. Note that this is not the same as the base radius for an aspheric lens. This is however the correct radius to use to build the surface profile in the manner described.

The numerical aperture of the OPD measurement must be known in order to add the OPD data to the spherical data. Recall that the OPD is a measure of the surface departure from a best-fit sphere, taken with the lens positioned so the center of curvature coincides with the focus of light from the interferometer. The NA defines the solid angle of the OPD measurement at confocal. Thus the NA of the measurement defines the $\sin\theta$ of the lens geometry, as shown

in Figure 3. The NA will be lower than the NA of the interferometer objective if the cone of light overfills the lens and/or the data is masked. From our masking and objective NA information, we estimate a cone angle of $10.6^\circ \pm 1^\circ$. The equation that defines the aperture from the geometry is $\rho_{\max} = R \sin\Theta$. An angle of 10.6° and a radius of 1366 mm gives $\rho_{\max} = 251.4 \mu\text{m}$. Error propagation gives an uncertainty estimate of $\pm 3.4 \mu\text{m}$ for ρ_{\max} .

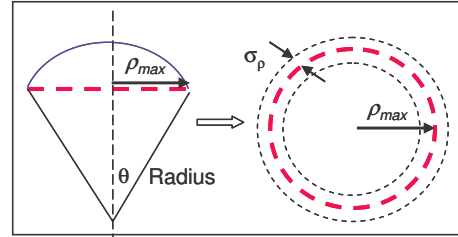


Fig. 3: Geometric relationship between aperture radius ρ_{\max} , radius of microlens and angle θ .

This aperture is less than the full aperture of the microlens (full aperture $\sim 400 \mu\text{m}$). One advantage of PSI compared to SWLI is that the entire surface of the lens can be measured, as long as the NA of the interferometer is large enough so the wave front overfills the lens. The NA for our measurements is large enough to measure the entire surface, but we masked our data down so the aperture matches the largest circular patch measured by the SWLI. In this way we can compare PSI to SWLI for measurements of the same lens region. In general, however, the full surface geometry should be used for the PSI analysis.

PSI surface geometry measurements are susceptible to artifacts if the lens is not well nulled for the measurement [28]. Well nulled means the focus of light from the interferometer is coincident with the center of curvature of the lens. It is not mechanically possible to position the lens perfectly, thus some artifacts are always present. The artifacts are observed as high order aberrations that increase approximately linearly with misalignment. The correlation can be observed and quantified by plotting the higher order Zernike coefficients versus the low order coefficients that represent misalignment (the coefficients corresponding to tip tilt and power). For example an approximately linear relationship will exist between the a_{20} (power) coefficient and the a_{40} coefficient (low order spherical aberration) [26]. The slope from a linear fit to

each curve estimates the correlation. These plots are referred to as alignment sensitivity plots. Although the microlens is nulled as well as possible for each of the 15 measurements, residual misalignment provides us with enough data to generate the alignment sensitivity plots. The aberrations up to second order spherical are included in our analysis. The average Zernike tip, tilt and power among our 15 measurements are approximately zero, but the standard deviation shows the likelihood for a single measurement to be misaligned. These tip tilt and power standard deviations are multiplied by the sensitivity curve slopes for an uncertainty estimate for each higher order Zernike coefficient (up to second order spherical). These uncertainties are used for the random generation of the surface profile in the Monte Carlo simulation.

To summarize, the dominant uncertainty contributors for PSI height profile measurements are noise in the measurement, estimation of the best-fit sphere radius, estimation of the aperture, and aberrations due to misalignment.

4. The Monte Carlo Simulation: Once the measurements are taken and uncertainties estimated, the Monte Carlo simulation can be carried out (Figure 1). The goal of the simulation is to determine the *distribution* of surface error maps that are likely, given the measurement uncertainty. To make the results more quantitative, we fit each error map to a set of Zernike polynomials and consider the mean and standard deviation for each Zernike coefficient. Thus, one can evaluate the amount of spherical aberration, astigmatism, coma, etc. in the surface error map and the uncertainty for each aberration. The analysis details for each iteration are described in this section.

For the SWLI, each surface profile estimate is determined by randomly picking one of the 11 measurements, and then using a randomly chosen sag and a lens center value from Gaussian distributions defined by the appropriate mean and uncertainty for each. The values for the sag distribution are $57.7 \mu\text{m} \pm 0.7 \mu\text{m}$ and lens center distribution $0 \pm 0.6 \mu\text{m}$. Then the two types of surface error maps are calculated. For the comparison to the design shape, the design shape is directly subtracted from the measurement surface profile. For the comparison to the best-fit conic, the best-fit conic surface is first determined, and then this is

directly subtracted from the measurement surface. The determination of the best-fit conic is described in detail elsewhere [8]. In brief, a conic surface model is compared to the data in a least-squares sense where only the conic constant is left as an unknown fit parameter. Definition of the conic model requires an estimate of the aperture diameter and the base radius of curvature. These values are also randomly chosen from Gaussian distributions defined by the appropriate mean and uncertainty. Information from the measurements is used to estimate these values. With this approach, the impact of the best-fit conic uncertainty is also captured in the final uncertainty in the surface error map (the surface error map compared to the best-fit conic, that is).

Examples of surface error maps for SWLI measurements are shown in Figure 4. The best fit conic surface is very close to the design shape conic, therefore the two surface error maps are very similar. Both maps contain tilt, power, astigmatism, and low-order spherical aberration. Tilt would result from an asymmetric etch during the manufacturing or a center offset between the measurement profile and the subtracted surface (best-fit conic or design shape). The spherical aberration indicates that the surface is not a perfect conic, but rather a general asphere. We did not characterize and remove system biases from the SWLI measurements and these can easily be on the order of 100s of nanometers [25]. Calibration to measure and remove these biases are challenging and beyond the scope of this work [29].

For PSI, we generate a profile by randomly picking one of the 15 OPD measurements and using a randomly chosen radius and aperture value from appropriately defined Gaussian distributions. The values for the radius distribution are $1366 \mu\text{m} \pm 17 \mu\text{m}$ and $251.4 \pm 3.4 \mu\text{m}$ for the aperture distribution. We then add small high-order aberration corrections to the OPD map to represent misalignment uncertainty. We do this by randomly picking a tip, tilt, and power from Gaussian distributions based on the standard deviations observed among the 15 measurements. We then multiply the tip, tilt, and power by the sensitivity curve slopes discussed above. This results in a set of correction coefficients for the high order Zernike coefficients for the OPD map. These coefficients are multiplied by the corresponding

Zernike polynomial and this is then added to the OPD map.

Examples of surface error maps for PSI measurements are shown in Figure 5. Again, the two error maps are very similar. The PSI measurements show surface errors dominated by power and spherical aberration. The power is larger than observed with the SWLI measurements. In Figure 5, two versions of the error maps are shown to appreciate both aberration features. The small inset to the left is the as-calculated surface error map dominated by the power. The larger image is the error map after removing power. A difference in the surface error maps between the SWLI and PSI measurements is not surprising. Measurement biases were removed from the PSI measurements but not from the SWLI measurements, as mentioned, and likely accounts for the difference.

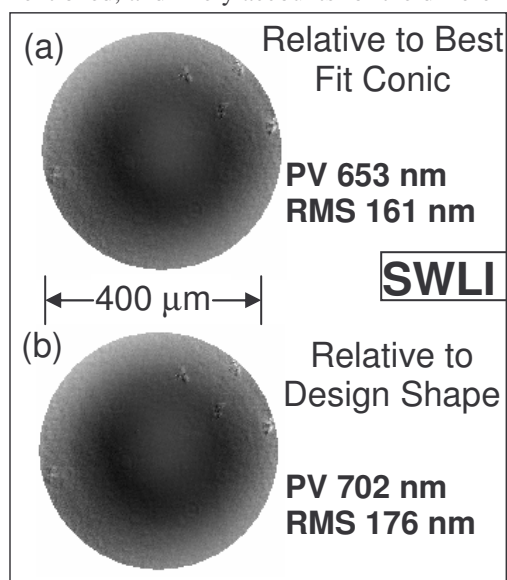


Fig. 4: Example surface error maps for the SWLI measurement analysis. The error maps subtracting both the best-fit conic surface and subtracting the design shape are shown.

The Monte Carlo simulation is iterated 200 times and 36 Zernike coefficients for each surface error map are determined and stored in an array [3]. The distributions for the coefficient at the conclusion of the Monte Carlo loop are the final goal. Each distribution captures the most likely Zernike coefficient and the expected variation due to measurement uncertainty. Our approach assumes uncertainty sources are uncorrelated, and this may not be rigorously true (for example measurement noise may impact the radius value).

But, likely any correlation has a smaller effect on the final Zernike coefficient distributions than the individual contributions.

A Monte Carlo approach is also useful because individual contributions to the uncertainty are easily investigated. One can repeat the simulation and allow only single uncertainty sources to vary at a time. This yields insight into their relative importance. We used only 50 iterations for these studies.

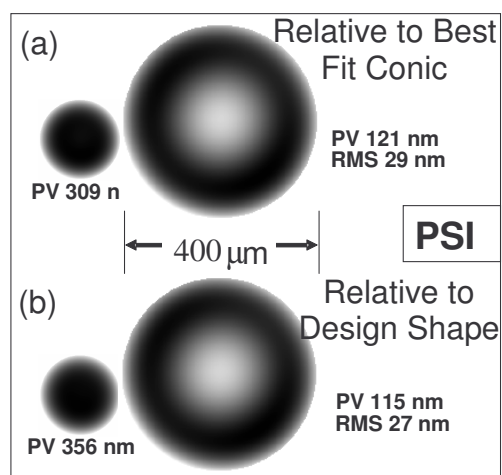


Fig. 5: Example surface error maps for the PSI measurement analysis. The error maps subtracting both the best-fit conic surface and subtracting the design shape are shown. Curvature is the dominant surface error observed for the PSI analysis, as seen in the smaller images on the left. Power is removed in the larger images so the spherical aberration can be seen.

5. Results and Discussion: The surface error map information is captured by the distributions of Zernike coefficients resulting from the Monte Carlo simulation. The mean and standard deviation for each distribution are good estimates of the Zernike coefficient of the surface error map and its uncertainty, respectively.

The dominant structure in the surface error maps from the SWLI measurements are tilt, power, astigmatism and spherical aberration. The type of information obtained is shown in Table 1 which lists the mean and standard deviation for the power and spherical aberration coefficients for the SWLI measurements. The values for both types of surface error maps are shown (compared to the design shape and the best-fit conic surface). Notice that the lowest order spherical aberration coefficient is the largest, followed by the power. The Monte Carlo analysis shows that the measurement uncertainty

has a much larger impact on the uncertainty in the power Zernike coefficient compared to the spherical aberration coefficient. This is useful information because, for example, much of the power error in the surface can be compensated for in a final lens assembly and alignment process, whereas the spherical aberration cannot.

Table 1: Example Zernike coefficient results for the surface error maps. The numbers correspond to the analysis applied to the SWLI measurements. The mean and standard deviations for the rotational symmetric coefficients are shown. Units are nanometers.				
Zernike Coefficient	Measurement Minus Design Shape		Measurement Minus Best-Fit Conic	
	Mean	σ	Mean	σ
A_{20}	-87	52	-38	77
A_{40}	-148	8	-147	8
A_{60}	15	7	15	7

Table 2: Example Zernike coefficient results for the surface error maps where uncertainty sources are varied one at a time to estimate relative importance. The numbers correspond to the analysis applied to the SWLI measurements where the surface error map is the difference between the measurement and the best-fit conic surface. The mean and standard deviations for the rotational symmetric coefficients are shown. Units are nanometers.				
Zernike Coefficient	Power a_{20}		Low-Order Spherical Aberration a_{40}	
	Mean	σ	Mean	σ
All	-38	77	-147	8.4
Noise	-35	72	-149	7.9
Radius	-40	71	-148	1.9
Aperture	-34	3	-148	1.8
Sag	-34	6	-148	1.5
Center	-34	-	-148	0.2

The assessment of individual uncertainty contributions for the SWLI measurements is summarized in Table 2. The surface error map compared to the best-fit conic is used for the illustration. The first row contains the same numbers in Table 1. The subsequent rows show the Zernike distribution characteristics when only a single uncertainty sources is varied (while holding the other values constant). ‘Noise’, ‘Sag’, and ‘Center’ are uncertainty sources affecting the generation of the measurement

profile, while ‘Radius’ and ‘Aperture’ affect the conic model used to determine the best-fit conic surface. The variation in the mean is not statistically significant, taking the uncertainty in the mean as σ/\sqrt{N} . The distribution widths are the important quantities to compare. For a visual comparison of the widths, we generate a Gaussian fit to e.g. a_{40} - a_{40} mean for each distribution, the distributions for the a_{20} and a_{40} coefficients are compared in Figure 6. The analysis reveals that the power in the surface error (a_{20}) is very sensitive to uncertainty in the radius used for the best-fit conic determination and to the noise in the measurements. In contrast, the uncertainty in the a_{40} coefficient is dominated by the measurement noise only.

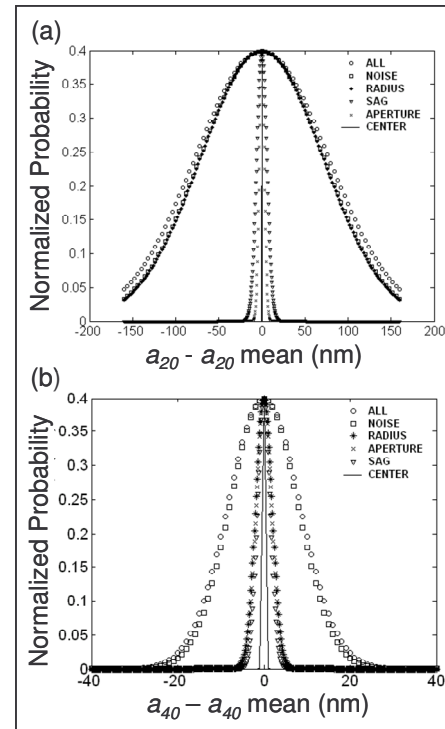


Fig. 6: Examples of two Zernike coefficient distributions for the SWLI measurements. The surface error maps are the difference between the measured geometry and the best-fit conic surface for these examples. (a) Distribution of the a_{20} Zernike coefficients for the surface error map. (b) Distribution of the a_{40} Zernike coefficients for the surface error map.

The dominant structure in the surface error maps from the PSI measurements are power and spherical aberration. Distribution parameters for the power (a_{20}) and the two lowest-order

spherical aberration coefficients (a_{40} and a_{60}) are listed in Table 3. The values for both types of surface error maps are shown. For the PSI measurements, the power and lowest-order spherical aberration have comparable contributions to the surface error maps. The measurement uncertainty has a dramatically larger impact on the uncertainty than the other coefficients. The Monte Carlo analysis shows that measurement uncertainty has a much larger impact on the final a_{20} uncertainty compared to any other aberration.

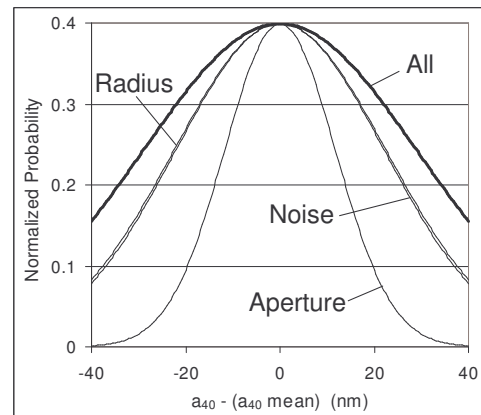
Zernike Coefficient	Measurement Minus Design Shape		Measurement Minus Best-Fit Conic	
	Mean	σ	Mean	σ
A_{20}	-130	116	-119	107
A_{40}	-112	5	-111	30
A_{60}	0.5	3	0.6	3

The assessment of individual uncertainty contributions for the PSI measurements is summarized in Table 4. The surface error map compared to the best-fit conic is used for the illustration. For the PSI measurements ‘Noise’, ‘Aperture’, and ‘Radius’ are uncertainty sources affecting the generation of the measurement profile, while ‘Aperture’ and ‘Radius’ alone affect the conic model used to determine the

Zernike Coefficient	Low-Order Spherical Aberration a_{40}	
	Mean	σ
All	-111	30
Noise	-110	22
Radius	-114	23
Aperture	-107	12

best-fit conic surface. For this analysis ‘Noise’ includes instrument noise in the measurements and the misalignment uncertainty discussed above. The distribution widths are compared in Figure 7 for the a_{40} where, as described above, Gaussian fits to $a_{40} - a_{40}$ mean were used for the comparison. The ‘Radius’ and the ‘Noise’ both have a significant and comparable contribution to the uncertainty in the a_{40} coefficient

6. Conclusions: We have presented an alternative analysis approach to characterizing surface geometry for microlens manufacturing. Current practice focuses on determining the best-fit conic constant and we propose to alternatively look at the surface error on the lens only. By surface error we mean the difference between the measured surface geometry and the design specification for the lens. We also consider the surface error as the difference between the measured geometry and the best-fit conic surface. Focusing on the surface error will provide stronger feedback to the manufacturing process while still allowing part conformance to be assessed. A complete uncertainty evaluation is a significant and important part of our approach. We estimate uncertainties for important



parameters

Fig. 7: Examples of one Zernike coefficient distribution for the PSI measurements. The surface error map is the difference between the measured geometry and the best-fit conic surface for this example.

from the measurement and then carry out a Monte Carlo simulation to estimate the resulting variation in the surface error map. We focus on a Zernike polynomial description of the surface error, and the Monte Carlo analysis yields a best estimate and an combined uncertainty for each

Zernike coefficient. We described our approach as applied to the two most dominant microlens metrology methods in use today, namely, scanning white light interferometry (SWLI) and phase shifting interferometry (PSI).

7. Acknowledgements: This material is based upon work supported by the National Science Foundation under Grant No. 0323505. Any opinions, findings, and conclusions or recommendations expressed in this material are those of the authors and do not necessarily reflect the views of the National Science Foundation. The authors would also like to thank Mark Boomgarden and Chris Linnen from Digital Optics Corporation, and Tom Suleski from UNC Charlotte.

8. References:

- [1] Frank L. Pedrotti, S.J. Leno S. Pedrotti, "Introduction to optics", 2nd edition, 1992.
- [2] Digital Optics Corporation, private communication.
- [3] J.C. Wayant and Katherine Creath, "Basic Wavefront Aberration Theory for Optical Metrology", in *Applied Optics and Optical Engineering*, vol. XI, Chapter 1, Academic Press (1992).
- [4] G. S. Kino and S. S. C. Chim, "Mirau correlation microscope," *Applied Optics* **29**, 3775-3783 (1990).
- [5] L. Deck and P. de Groot, "High speed noncontact profiler based on scanning white light interferometry," *Applied Optics* **33**, 7334-7338 (1994).
- [6] J. Schmit and A. Olszak, "High precision shape measurement by white-light interferometry with real time scanner correction," *Applied Optics* **41**, 5943-5950 (2002).
- [7] J.E. Greivenkamp and J. H. Burning, "Phase shifting interferometers," in *Optical shop testing*, D. Malacara, ed. (Wiley, 1992), pp. 501-598.
- [8] Solomon A. Gugs and Angela Davies, "Least-Squares Minimization and Monte Carlo Approach to Estimating the Conic Constant and Uncertainty for Microlens Measurements", to be published in *Applied Optics*
- [9] D. Malacara, "Optical Shop Testing" Chapter 13, Wiley, New York, 1992.
- [10] Davidson M., Kaufman K., Mazor I., and Cohen F., *Proceedings of the SPIE*, **775** (Bellingham, Washington: SPIE), p. 233 (1987).
- [11] Lee B. S., and Strand T C., 1990, *Applied Optics*, **29**, 3784
- [12] Kino G. S., and Chim S.C., *Applied Optics*, **29** 3775 (1990).
- [13] Caber, P.J., *Applied Optics*, **32** 3438 (1993).
- [14] Sandoz P., and Tribillon G., *Journal of Modern Optics*, **40** 1691 (1993).
- [15] Hariharan P., and Roy M., *Journal of Modern Optics*, **42** 2357 (1995).
- [16] De Groot P., and Deck L., *Journal of Modern Optics*, **42** 389 (1995).
- [17] Hariharan P., and Roy M., *Journal of Modern Optics*, **41** 2197 (1994).
- [18] Gallagher, J. E. and D. R. Herriott, "Wavefront Measurement." U. S. Patent 3, 694,088 (1972/1972).
- [19] Burning, J. H., D. R. Herriott, J. E. Gallagher, D. P. Rosenfeld, A. D. White, and D. J. Brangaccio, "Digital Wavefront Measuring Interferometer for Testing Optical Surfaces and Lenses," *Appl. Opt.*, **13**, 2693 (1974).
- [20] Greivenkamp, J. E., "Interferometric Measurements at Eastman Kodak Company," *Proc. SPIE*, **816**, 212 (1987a).
- [21] Carre, P. "Installation et Utilisation du Comparateur Photoelectrique et Interferentiel du Bureau International des Poids de Mesures," *Metrologia* **2**, 13 (1966).
- [22] Hariharan, P. B. F. Oreb, and T. Eiju, "Digital Phase-Shifting Interferometry: A simple Error-Compensating Phase Calculation Algorithm," *Appl. Opt.*, **26**, 2504 (1987a).
- [23] D. Malacara and S. L. DeVore, "Interferogram Evaluation and Wavefront Fitting," in *Optical Shop Testing*, D. Malacara, Ed. Wiley, New York, 1992.

[24] D. Malacara, "Optical Shop Testing" Appendix 1, Wiley, New York, (1992).

[25] "Self-calibration for Micro-refractive Lens Measurements." N. Gardner and A. Davies, *Optical Engineering*, 45 (3), (2006).

[26] S. Gugsu, "New Analysis Strategies for Micro Aspheric Lens Metrology," Ph. D. Dissertation, Department of Physics and Optical Science, UNC Charlotte, to be submitted June 2006.

[27] T. L. Schmitz, A. Davies, and C. J. Evans, "Uncertainties in interferometric measurements of radius of curvature." SPIE Conference Proceedings, SPIE's 46th Annual International Symposium on Optical Science and Technology, July (2001).

[28] C. J. Evans, "Compensation of Errors Introduced by Nonzero Fringe Densities in Phase-shifting Interferometry," *Annals of the CIRP*, **42**, pp. 577-780, 1993.

[29] Joanna Schmit and Erik Novak and Artur G. Olszak, "White-light interferometer with internal length standard", Veeco Metrology, 2650 E Elvira Road, Tucson, Arizona, USA

APPENDIX C: MISALIGNMENT SIMUATION CODE

```

% The program does the following
% request different inputs like conic constant, misalignments,etc
% correct OPDs at the edges
% specify sag equations for both reference and test surface
% calculate OPDs along the radial direction of the reference sphere radius
% use transformation of coordinates during misalignments
k=input('conic constant of the part ='); ks=0;
I0=1; La=0.6328;
r1=input('radius of curvature (um)of the part=');
dia=input('diamter (um) of the part=');
NAo=input('numerical aperture');
NAL=(dia/2)/r1; do=2*r1*NAo; MM=512;
x_center = MM/2; y_center = MM/2; center_pos = [x_center y_center];
if NAL > NAo NA=NAo; else NA=NAL; end
Mask=input('mask in % (80,etc) =');d=(Mask/100);
Lx=input('translation along X or Y=');
Ly=input('translation along Y or Y=');
Lz=input('translation along Z or Y=');
ThetaX=input('rotation angle of the part about X in CCW (+ve) or inCW (-ve)');
ThetaY=input('rotation angle of the part about Y in CCW (+ve) or inCW (-ve)');
ThetaZ=input('rotation angle of the part about Z in CCW (+ve) or inCW (-ve)');
A=[-MM/2:1:MM/2]; B=[-MM/2:1:MM/2]; [x1,y1]=meshgrid(A,B);
%%%%%%%%%%%%%%%%%%%%%%%%%%%%%%%%%%%%%%%%%%%%%%%%%%%%%%%%%%%%%%%%%%%%%%%%
% OPD correction at the edge (very small correction)
rho=r1*NA;
zsag=(-r1/(k+1))*(1-sqrt(1-(k+1)*NA^2))+r1;
zsagp=r1*(1-NA^2/2); % sag for a parabola
opd=abs(sqrt(rho^2 + zsag^2)-r1);
opdp=sqrt(rho^2 + zsagp^2)-r1; % OPD for a parabola
if k== -1
    Dpr= (do -2*NA*opdp);
else
    Dpr= (do -2*NA*opd);
end
r=r1*MM/Dpr; c=1/r; s=sqrt(x1.^2 + y1.^2);
%%%%%%%%%%%%%%%%%%%%%%%%%%%%%%%%%%%%%%%%%%%%%%%%%%%%%%%%%%%%%%%%%%%%%%%%
for ii=1:Lx
    if s < r
        xt=x1+ ii; yt=y1;
        Zs=-(c*s.^2./(1+sqrt(1-(k+1)*c^2*(s.^2))))+r; % the convex surface equation
        ZRef=-(c*s.^2./(1+sqrt(1-(ks+1)*c^2*(s.^2))))+r; % the reference wavefront
        else nan; end
        xsp=1*xt + 0*yt + 0*(Zs); ysp=0*xt + 1*yt + 0*(Zs); zsp=0*xt + 0*yt + 1*(Zs);
        W= -sqrt(x1.^2 + y1.^2 + ZRef.^2) + sqrt((xsp).^2 + (ysp).^2 + (zsp).^2);
        newzs=W; rr =(y_center)*d; [z_heights] = mask_circle(newzs,center_pos,rr);
    end
end

```

```

ITs=I0*(1+cos(4*pi*(z_heights./La))); % intensity; end

for jj=1:Ly
    if s < r
        xt=x1; yt=y1+ jj; %the part coordinate interms of the reference coordinate
        Zs=-(c*s.^2./(1+sqrt(1-(k+1)*c^2*(s.^2)))) +r; % the part (convex) surface equation
        ZRef=-(c*s.^2./(1+sqrt(1-(ks+1)*c^2*(s.^2))))+r; % the reference wavefront
        else nan; end
    xsp=1*xt + 0*yt + 0*(Zs); ysp=0*xt + 1*yt + 0*(Zs); zsp=0*xt + 0*yt + 1*(Zs);
    W= -sqrt(x1.^2 + y1.^2 + ZRef.^2) + sqrt((xsp).^2 + (ysp).^2 + (zsp).^2);
    newzs=W;rr =(y_center)*d; [z_heights] = mask_circle(newzs,center_pos,rr);
    ITss=I0*(1+cos(4*pi*(z_heights./La))); end

for q =1:Lz
    % reference sphere radius correction (z_misalignment)
    rz=r1-4*(q-1); C=1/rz;
    dr=sqrt(r^2 - 2*r*4*(q-1))-r; drz=sqrt(rz^2 - 2*rz*4*(q-1))-rz;
    X=(1+(dr/r))*x1; Y=(1+(dr/r))*y1; S=sqrt((X).^2 + (Y).^2);
    Xz=(1+(drz/rz))*x1; Yz=(1+(drz/rz))*y1; Sz=sqrt((Xz).^2 + (Yz).^2);

    if r <= rz & s < r & S < rz
        xt=X; yt=Y;
        Zs=-(c*s.^2./(1+sqrt(1-(k+1)*c^2*(s.^2)))) +r;
        ZRef=-(C*S.^2./(1+sqrt(1-(ks+1)*C^2*(S.^2))))+rz;

        xsp=1*xt + 0*yt + 0*(Zs-4*(q-1)); ysp=0*xt + 1*yt + 0*(Zs-4*(q-1));
        zsp=0*xt + 0*yt + 1*(Zs-4*(q-1));
        W= -sqrt(X.^2 + Y.^2 + ZRef.^2) + sqrt((xsp).^2 + (ysp).^2 + (zsp).^2);
        newzs=W;rr =(y_center)*d; [z_heights] = mask_circle(newzs,center_pos,rr);
        ITsss=2*I0*(1+cos(4*pi*(z_heights./La)));
    else if r > rz & s < r & Sz < rz
        xtz=Xz; ytz=Yz;
        Zs=-(c*s.^2./(1+sqrt(1-(k+1)*c^2*(s.^2))))+r;
        ZRef=-(C*Sz.^2./(1+sqrt(1-(ks+1)*C^2*(Sz.^2))))+rz;

        xsp=1*xtz + 0*ytz + 0*(Zs-4*(q-1)); ysp=0*xtz + 1*ytz + 0*(Zs-4*(q-1));
        zsp=0*xtz + 0*ytz + 1*(Zs-4*(q-1));
        W= -sqrt(X.^2 + Y.^2 + ZRef.^2)+sqrt((xsp).^2 + (ysp).^2 + (zsp).^2);
        newzs=W; rr = (y_center)*d; [z_heights] = mask_circle(newzs,center_pos,rr);
        ITsss=I0*(1+cos(4*pi*(z_heights./La)));
    else nan; end end end

for tip=1:2
    Rxp=[1 0 0; 0 cos(tip*ThetaX*pi/180) sin(tip*ThetaX*pi/180); 0 -sin(tip*ThetaX*pi/180)
    cos(tip*ThetaX*pi/180)];

```

```

Ryp=[cos(0*ThetaY*pi/180) 0 -sin(0*ThetaY*pi/180); 0 1 0; sin(0*ThetaY*pi/180) 0
cos(0*ThetaY*pi/180)];
Rzp=[cos(0*ThetaZ*pi/180) sin(0*ThetaZ*pi/180) 0; -sin(0*ThetaZ*pi/180)
cos(0*ThetaZ*pi/180) 0; 0 0 1];
R1p=Rxp*(Ryp*Rzp); R2p=Rxp*(Rzp*Ryp); R3p=Ryp*(Rxp*Rzp);
R4p=Ryp*(Rzp*Rxp); R5p=Rzp*(Rxp*Ryp); R6p=Rzp*(Ryp*Rxp); RR=R6p;
if s < r
    xt=x1; yt=y1;
    Zs=-(c*s.^2./(1+sqrt(1-(k+1)*c^2*(s.^2))));
    ZRef=-(c*s.^2./(1+sqrt(1-(ks+1)*c^2*(s.^2))));
    else      nan;      end
    xsp=RR(1,1).*(xt-1) + RR(1,2).*yt + RR(1,3).*(Zs);
    ysp=RR(2,1).*xt + RR(2,2).*(yt-1) + RR(2,3).*(Zs);
    zsp=RR(3,1).*xt + RR(3,2).*yt + RR(3,3).*(Zs-1);
    W= sqrt((xsp-x1).^2 + (ysp-y1).^2 + (zsp-ZRef).^2);
    newzs=W;rr =(y_center)*d;[z_heights] = mask_circle(newzs,center_pos,rr);
    ITssss=I0*(1+cos(4*pi*(z_heights./La))); end
for til=1:2
Rxt=[1 0 0; 0 cos(0*ThetaX*pi/180) sin(0*ThetaX*pi/180); 0 -sin(0*ThetaX*pi/180)
cos(0*ThetaX*pi/180)];
Ryt=[cos(til*ThetaY*pi/180) 0 -sin(til*ThetaY*pi/180); 0 1 0; sin(til*ThetaY*pi/180) 0
cos(til*ThetaY*pi/180)];
Rzt=[cos(0*ThetaZ*pi/180) sin(0*ThetaZ*pi/180) 0; -sin(0*ThetaZ*pi/180)
cos(0*ThetaZ*pi/180) 0; 0 0 1];
R1t=Rxt*(Ryt*Rzt); R2t=Rxt*(Rzt*Ryt); R3t=Ryt*(Rxt*Rzt);
R4t=Ryt*(Rzt*Rxt); R5t=Rzt*(Rxt*Ryt); R6t=Rzt*(Ryt*Rxt); RRt=R6t;
if s < r
    xt=x1; yt=y1;
    Zs=-(c*s.^2./(1+sqrt(1-(k+1)*c^2*(s.^2))));
    ZRef=-(c*s.^2./(1+sqrt(1-(ks+1)*c^2*(s.^2))));
    else      nan;      end
    xsp=RRt(1,1).*(xt+1) + RRt(1,2).*yt + RRt(1,3).*(Zs);
    ysp=RRt(2,1).*xt + RRt(2,2).*(yt+1) + RRt(2,3).*(Zs);
    zsp=RRt(3,1).*xt + RRt(3,2).*yt + RRt(3,3).*(Zs+1);
    W= sqrt((xsp-x1).^2 + (ysp-y1).^2 + (zsp-ZRef).^2);
    newzs=W;rr =(y_center)*d;[z_heights] = mask_circle(newzs,center_pos,rr);
    ITssss=2*I0*(1+cos(4*pi*(z_heights./La))); end

for tiz=1:2
Rxz=[1 0 0; 0 cos(0*ThetaX*pi/180) sin(0*ThetaX*pi/180); 0 -sin(0*ThetaX*pi/180)
cos(0*ThetaX*pi/180)];
Ryz=[cos(0*ThetaY*pi/180) 0 -sin(0*ThetaY*pi/180); 0 1 0; sin(0*ThetaY*pi/180) 0
cos(0*ThetaY*pi/180)];
Rzz=[cos(tiz*ThetaZ*pi/180) sin(tiz*ThetaZ*pi/180) 0; -sin(tiz*ThetaZ*pi/180)
cos(tiz*ThetaZ*pi/180) 0; 0 0 1];
R1z=Rxz*(Ryz*Rzz); R2z=Rxz*(Rzz*Ryz); R3z=Ryz*(Rxz*Rzz);

```

```

R4z=Ryz*(Rzz*Rxz); R5z=Rzz*(Rxz*Ryz); R6z=Rzz*(Ryz*Rxz); RRz=R6z;
if s < r
    xt=x1; yt=y1;
    Zs=-(c*s.^2./(1+sqrt(1-(k+1)*c^2*(s.^2))));
    ZRef=-(c*s.^2./(1+sqrt(1-(ks+1)*c^2*(s.^2))));
    else nan; end
    xsp=RRz(1,1).*(xt-2) + RRz(1,2).*yt + RRz(1,3).*(Zs);
    ysp=RRz(2,1).*xt + RRz(2,2).*(yt-2) + RRz(2,3).*(Zs);
    zsp=RRz(3,1).*xt + RRz(3,2).*yt + RRz(3,3).*(Zs-2);
    W= sqrt((xsp-x1).^2 + (ysp-y1).^2 + (zsp-ZRef).^2);
newzs=W; rr =(y_center)*d; [z_heights] = mask_circle(newzs,center_pos,rr);
ITsssss=2*I0*(1+cos(4*pi*(z_heights./La))); end

```

APPENDIX D: MONTE CARLO SIMULATION CODE

```

% This program does the following
% randomly pick the measured .opd file
% assigned random sigmas for Monte Carlo (zero for chi-square)
% generate simulated surface
% find chi-squares and do minimization
% generate intended surface
% find the residual error surfaces and find Zernikes
% save files to .xls and .opd as necessary
%%%%%%%%%%%%%%%%%%%%%%%%%%%%%%%%%%%%%%%%%%%%%%%%%%%%%%%%%%%%%%%%%%%%%%%%
L=50; NN=100;
NEWX=780;NEWY=780;x_centtt=NEWX/2;y_centtt=NEWY/2;
centt_pos = [x_centtt y_centtt];
NNEWX=880;NNEWY=880; CENTERXX=NNEWX/2; CENTERYY=NNEWY/2;
CENTTR_POSS=[CENTERYY CENTERXX];
Ka=-3.6; Kb=-0.6; dK=(Kb-Ka)/NN; % conic constant range and steps
aa=linspace(-NEWX/2,NEWX/2,NEWX);bb=linspace(-NEWY/2,NEWY/2,NEWY);
[X,Y]=meshgrid((1.103)*aa,(1.103)*bb);% pixel to um
Lenxx=length(aa);Lenyy=length(bb);
newm = floor(length(aa)); newn = floor(length(bb));padnum = nan;
Zsurf1 = zeros(newm,newn);Zsurf2 = zeros(newm,newn);
r3 = 400/1.103; % aperture radius
%%%%%%%%%%%%%%%%%%%%%%%%%%%%%%%%%%%%%%%%%%%%%%%%%%%%%%%%%%%%%%%%%%%%%%%%
for i=1:L
gg=floor(11*rand)+30;
fname_str=['DS2LSTITCH',num2str(gg),'.opd']; % file name
% fname_str=['DS2LSTITCHAVERAGE.opd'];
[array,wavelength,aspect,pxlsize]=readopd(fname_str);
[ii,jj]=find(~isnan(array));
imin=min(ii);imax=max(ii);jmin=min(jj);jmax=max(jj);
apr=randn;sr=0.5*randn; % sigmas of aperture radius and sag, zero for best estimate.
crx=0.5*randn;cry=0.5*randn; % sigmas of center, zero for best estimate.
rcr=20*randn; % sigma of the base radius, zero for best estimate.
x_center = ((jmax-jmin)/2);y_center = ((imax-imin)/2);
center_pos = [x_center y_center];
array11=array(imin:1:imax,jmin:1:jmax);
AARR=POSITION_N_PAD(newn,newm,y_centtt,x_centtt,array11,padnum);
[Zcc_height] = mask_circle(AARR,centt_pos,r3);
[Z_height] = mask_circle(Zcc_height,centt_pos,r3);
Zmax=max(Z_height(:));Zmin=min(Z_height(:)); % measured sag is 57.68um
Z_he1=Z_height-Zmax; Zmsag=(57.68)+sr;Z_heel=Z_he1+Zmsag;
R=1360; ;Rr=R+rcr;C=1/Rr;
S=(sqrt((X).^2 + (Y).^2));Smax=max(S(:));Smin=min(S(:));
for q=1:NN
KK=Ka + dK*(q-1);
if S < Rr

```

```

Zsurf1=-C*S.^2./(1+sqrt(1-(KK+1)*C^2*S.^2));
Zsurf2=-C*S.^2./(1+sqrt(1-(KK+dK+1)*C^2*S.^2));
Znew1=Zsurf1;Znew2=Zsurf2; r2=r3+apr;
[ZZ_height1] = mask_circle(Znew1,centt_pos,r2);
[ZZ_height2] = mask_circle(Znew2,centt_pos,r2);
else nan; end
newzz1=ZZ_height1;
[Z_heightt1] = mask_circle(newzz1,centt_pos,r2);
ZZZsagg1=max(Z_heightt1(:))-min(Z_heightt1(:));
newzz2=ZZ_height2;
[Z_heightt2] = mask_circle(newzz2,centt_pos,r2);
ZZZsagg2=max(Z_heightt2(:))-min(Z_heightt2(:));
ZtestSAG=max(ZZ_height1(:))-min(ZZ_height1(:));
ZZmax1=max(Z_heightt1(:));ZZmin1=min(Z_heightt1(:));
ZZsag1=ZZmax1-ZZmin1; ZZZ_1=(Z_heightt1-ZZmin1);
ZZmax2=max(Z_heightt2(:));ZZmin2=min(Z_heightt2(:));
ZZsag2=ZZmax2-ZZmin2;ZZZ_2=(Z_heightt2-ZZmin2);
ZZZ1=POSITION_N_PAD(NNEWY,NNEWX,CENTERYY,CENTERXX,ZZZ_1,
padnum);
ZZZ2=POSITION_N_PAD(NNEWY,NNEWX,CENTERYY,CENTERXX,ZZZ_2,
padnum);
Z_hee=POSITION_N_PAD(NNEWY,NNEWX,CENTERYY+crx,CENTERXX+cry,
Z_hee1,padnum);
Zneww1=(Z_hee-ZZZ1);
[Zopti1] = mask_circle(Zneww1,CENTTR_POSS,r2);
Zneww2=(Z_hee-ZZZ2);
[Zopti2] = mask_circle(Zneww2,CENTTR_POSS,r2);
dzz=std(~isnan(Zopti1));dz1=dzz(:);dz=4*sum(dz1(~isnan(dz1)));
ZEE1=Zopti1(:);E1=sum((ZEE1(~isnan(ZEE1))).^2./dz.^2);% E1 is Chi-square
ZEE2=Zopti2(:);E2=sum((ZEE2(~isnan(ZEE2))).^2./dz.^2);% E2 is Chi-square
slopeMin=((E1 -E2)./dK); % slope

if slopeMin < 0
fid=fopen('CHI_SQUARESTITCH.xls','at'); % save chi-square values
fprintf(fid,'%0.4ft%0.4ft%0.4ft%0.4fn',KK,E1,E2,slopeMin);fclose(fid);
ZAVG=(ZZZ1 + ZZZ2)./2; % Best fit
AA=[Rr,crx,cry,r3,Smax,Smin,r2,KK,Zmsag,ZZsag1,ZZsag2,E1,E2,slopeMin];
fid=fopen('BESTFITPSTITCH.xls','at');fprintf(fid,'format',AA);fclose(fid);
%%%%%%%%%%%%%%
% Intended surface
RC=1375; KC=-2.1; rc=r3; CC=1/RC;
if S < RC
ZI=-CC*S.^2./(1+sqrt(1-(KC+1)*CC^2*S.^2));[ZIN]
= mask_circle(ZI,centt_pos,rc);
else nan; end
NNEWW=ZIN; ZZ_IN=mask_circle(NNEWW,centt_pos,rc);

```

```

ZINN=ZZ_IN - min(ZZ_IN(:));
ZINT=POSITION_N_PAD(NNEWY,NNEWX,CENTERYY,CENTERXX,ZINN,
padnum);
%%%%%%%%%%%%%%%%%%%%%%%%%%%%%%%%%%%%%%%%%%%%%%%%%%%%%%%%%%%%%%%%%%%%%%%%
ZRESM= Z_hee - ZINT; ZRESD= Z_hee - ZAVG; ZRESF=ZRESD - ZRESM;
newzA=ZAVG; % best fit surface
fid=fopen('BESTFIT_1.xls','at');fprintf(fid,'format',zernsA);fclose(fid);
ZAVGG=POSITION_N_PAD(NNEWY,NNEWX,CENTERYY,CENTERXX,
newzA,padnum);
writeopd(['BESTFITSTITCH_',num2str(i),'.opd'],ZAVGG,633,1,0.001103);
newzI=ZINT; % Intended surface
fid=fopen('INTENDED_1.xls','at');fprintf(fid,'format',zernsI);fclose(fid);
ZINTT=POSITION_N_PAD(NNEWY,NNEWX,CENTERYY,CENTERXX,newzI,
padnum);
writeopd(['INTENDEDSTITCH_',num2str(1),'.opd'],ZINTT,633,1,0.001103);
newzE=Z_hee; % measured surface data
fid=fopen('DATA_1.xls','at');fprintf(fid,'format',zernsE);fclose(fid);
Z_heee=POSITION_N_PAD(NNEWY,NNEWX,CENTERYY,CENTERXX,newzE,
padnum);
writeopd(['DATASTITCH_',num2str(i),'.opd'],Z_heee,633,1,0.001103);
newzs=ZRESF; % Intended from Best fit
[z_heightss] = mask_circle(newzs,CENTTR_POSS,r2);
[x_vectF,y_vectF]=get_xy(newzs,1);
zz_RESF=RMTERMSISO((1.103)*x_vectF,(1.103)*y_vectF,z_heightss,[0 1 1 1 1
1 1 1 1 1 1 1 1 1 1 1 1 1 1 1 1 1 1 1 1 1 1 1 1 1 1 1],36);
[z_RESF] = mask_circle(zz_RESF,CENTTR_POSS,r2);
vsize= size(zz_RESF);
[mr,ma] = zern_radius_angle(vsize,CENTTR_POSS,r2);
num_zernss = 36;viz = 1:1:num_zernss; % find zernike
[vpars,rmses,spars,tpars,ppars] = zern_estim(zz_RESF,mr,ma,viz); zernss = (vpars);
fid=fopen('INTFBESTFITSTITCH_1.xls','at');fprintf(fid,'format',zernss);fclose(fid);
ZRESFF=POSITION_N_PAD(NNEWX,NNEWY,CENTERYY,CENTERXX,z_RE
SF,padnum);
writeopd(['INTFBESTFITSTITCH_',num2str(i),'.opd'],ZRESFF,633,1,0.001103);
newzm=ZRESM; % Intended from Data
[z_heightsm] = mask_circle(newzm,CENTTR_POSS,r2);
[x_vectM,y_vectM]=get_xy(newzm,1);
zz_RESM=RMTERMSISO((1.103)*x_vectM,(1.103)*y_vectM,z_heightsm,[0 1 1 1
1 1 1 1 1 1 1 1 1 1 1 1 1 1 1 1 1 1 1 1 1 1 1 1 1 1 1 1],36);
[z_RESM] = mask_circle(zz_RESM,CENTTR_POSS,r2);
vsize= size(zz_RESM);
[mr,ma] = zern_radius_angle(vsize,CENTTR_POSS,r2);
num_zernsm = 36;viz = 1:1:num_zernsm;
[vparm,rmssem,sparm,tparm,pparm]=zern_estim(zz_RESM,mr,ma,viz);zernsm =
(vparm);
fid=fopen('INTFDATASTITCH_1.xls','at');fprintf(fid,'format',zernsm);fclose(fid);

```

```

ZRESMM=POSITION_N_PAD(NNEWX,NNEWY,CENTERYY,CENTERXX,
z_RESM,padnum);
writeopd(['INTFDATASTITCH_',num2str(i),'.opd'],ZRESMM,633,1,0.001103);
newzd=ZRESD; % Best fit from Data
[z_heightsd] = mask_circle(newzd,CENTTR_POSS,r2);
[x_vectD,y_vectD]=get_xy(newzd,1);
zz_RESD=RMTERMSISO((1.103)*x_vectD,(1.103)*y_vectD,z_heightsd,[0 1 1 1 1
1 1 1 1 1 1 1 1 1 1 1 1 1 1 1 1 1 1 1 1 1 1 1 1 1 1 1 1],36);
[z_RESD] = mask_circle(zz_RESD,CENTTR_POSS,r2);
vsize= size(zz_RESD);
[mr,ma] = zern_radius_angle(vsize,CENTTR_POSS,r2);
num_zernsd = 36; viz = 1:1:num_zernsd;
[vpard,rmsed,spard,tpard,ppard] = zern_estim(zz_RESD,mr,ma,viz); zernsd = (vpard);
fid=fopen('BESTFITFDATASTITCH_1.xls','at');fprintf(fid,'format',zernsd);
fclose(fid);
ZRESDD=POSITION_N_PAD(NNEWX,NNEWY,CENTERYY,CENTERXX,z_RE
SD,padnum);
writeopd(['BESTFITFDATASTITCH_',num2str(i),'.opd'],ZRESDD,633,1,0.001103);
break; else nan; end end end

```



```

x2=x.*x; y2=y.*y; xy=x.*y; x3=x2.*x; y3=y2.*y; xy2=x.*y2; x2y=x2.*y; r2=x2+y2;
x4=x2.*x2; y4=y2.*y2; x5=x3.*x2; y5=y3.*y2;
x6=x4.*x2; y6=y4.*y2; x7=x5.*x2; y7=y5.*y2; x8=x4.*x4; y8=y4.*y4; x9=x7.*x2;
y9=y7.*y2; x10=x8.*x2; y10=y8.*y2; p4=r2.*r2; p6=p4.*r2;
% write Zernike polynomials for the bias
ABB1=ABB(1)*ones(512,512)+ABB(2)*x+ABB(3)*y+ABB(4)*(2*x2+2*y2-
1)+ABB(5)*(x2-y2)+ABB(6)*(2*xy)+ABB(7)*(3*x3+3*xy2-
2*x)+ABB(8)*(3*x2y+3*y3-2*y)+ABB(9)*(6*r2.*r2-6*r2+1)+ABB(10)*(x3-3*xy2);
ABB2=ABB(11)*(3*x2y-y3)+ABB(12)*(4*x2.*x2-3*x2+3*y2-
4*y2.*y2)+ABB(13)*(8*x3.*y+8*x.*y3-
6*xy)+ABB(14)*(10*x3.*x2+20*x3.*y2+10*xy.*y3-12*x3-
12*xy2+3*x)+ABB(15)*(10*x2y.*x2+20*x2y.*y2+10*y3.*y2-12*x2y-12*y3+3*y);
ABB3=ABB(16)*(20*p6-30*p4+12*r2-1)+ABB(17)*(x2.*x2-
6*x2.*y2+y2.*y2)+ABB(18)*(4*x3.*y-4*x.*y3)+ABB(19)*(5*x3.*x2-10*x3.*y2-4*x3-
15*xy2.*y2+12*xy2)+ABB(20)*(-5*y3.*y2+10*x2.*y3+4*y3+15*x2y.*x2-
12*x2y)+ABB(21)*(15*x3.*x3+15*x2y.*x2y-15*x2y.*y3-20*x2.*x2+6*x2-
15*y3.*y3+20*y3.*y-6*y2);
ABB4=ABB(22)*(30*x3.*x2y+60*x2y.*xy2+30*xy2.*y3-40*x3.*y-40*xy2.*y
+12*xy)+ABB(23)*(35*x4.*x3+105*x4.*xy2+105*x3.*y4+35*xy2.*y4-60*x.*x4-
120*x2.*xy2-60*x.*y4+30*x3+30*xy2-
4*x)+ABB(24)*(35*x4.*x2y+105*x4.*y3+105*x2y.*y4+35*y4.*y3-60*x4.*y-
120*x2y.*y2-60*y4.*y+30*x2y+30*y3-4*y)+ABB(25)*(-(70*y8+280*y6.*x2
+420*y4.*x4 + 280*y2.*x6 + 70*x8 -140*y6 -420*y4.*x2 -420*y2.*x4 -140*x6 +90*y4
+180*y2.*x2 + 90*x4 -20*y2 -20*x2 +1));
ABB5=ABB(26)*(x3.*x2-10*x3.*y2+5*xy2.*y2)+ABB(27)*(5*x2y.*x2-
10*x2.*y3+y3.*y2)+ABB(28)*(6*x3.*x3-30*x2y.*x2y-30*x2y.*y3+6*y3.*y3-
5*x2.*x2+30*x2.*y2-5*y2.*y2)+ABB(29)*(24*x3.*x2y-20*x2y.*x-
24*xy2.*y3+20*xy2.*y)+ABB(30)*(21*x4.*x3-21*x4.*xy2-105*x3.*y4-
30*x4.*x+60*x3.*y2+10*x3-63*xy2.*y4+90*x.*y4-
30*xy2)+ABB(31)*(63*x4.*x2y+105*x4.*y3+21*x2y.*y4-90*x4.*y-
60*x2.*y3+30*x2y-21*y3.*y4+30*y4.*y-10*y3);
ABB6=ABB(32)*(-(-56*y8 -112*y6.*x2 -112*y2.*x6 +56*x8 +105*y6 +105*y4.*x2 -
105*y2.*x4 -105*x6 -60*y4 +60*x4 +10*y2 -10*x2));
ABB7=ABB(33)*(-((112*y7.*x +336*y5.*x3 +336*y3.*x5 +112*y.*x7 -210*y5.*x -
420*y3.*x3 -210*y.*x5 +120*y3.*x +120*y.*x3 -20*y.*x));
ABB8=ABB(34)*(-((126*y8.*x +504.*y6.*x3 +756*y4.*x5 +504*y2.*x7 +126*x8.*x -
280*y6.*x -840*y4.*x3 -840*y2.*x5 -280*x7 +210*y4.*x +420*y2.*x3 +210*x5 -
60*y2.*x -60*x3 +5*x));
ABB9=ABB(35)*(-((126*y9 +504.*y7.*x2 +756*y5.*x4 +504*y3.*x6 +126*y.*x8 -
280*y7 -840*y5.*x2 -840*y3.*x4 -280*y.*x6 +210*y5 +420*y3.*x2 +210*y.*x4 -
60*y3 -60*y.*x2 +5*y));
ABB10=ABB(36)*(-((252*y10 +1260.*y8.*x2 +2520*y6.*x4 +2520*y4.*x6 +
1260*y2.*x8 +252*x10 -630*y8 -2520*y6.*x2 -3780*y4.*x4 -2520*y2.*x6 -630*x8 +
560*y6 +1680*y4.*x2 +1680*y2.*x4 +560*x6 -210*y4 -420*y2.*x2-210*x4 +30*y2
+30*x2 -1));
ABBPLOT=ABB1+...+ABB10;

```

```

ABPLO=mask_circle(ABBPLOT,cent_pos,ar);
ABBPLOTFF=POSITION_N_PAD(newm,newn,centt,centt,ABPLO,padnum);
ABBPPLL=RMTERMSISO(muu*(1170/512)*x_vectz,muu*(1170/512)*y_vectz,ABBP
LOTFF,[0 1 1 1 1 1 1 1 1 1 1 1 1 1 1 1 1 1 1 1 1 1 1 1 1 1 1 1 1 1 1 1],36);
ABPLOO=mask_circle(ABBPPLL,cent_pos,ar);

vsize= size(ABPLOO);
[mr,ma] = zern_radius_angle(vsize,cent_pos,ar);num_zernsSA = 36;
viz = 1:1:num_zernsSA;
[vparSA,rmseSA,sparSA,tparSA,pparSA] = zern_estim(ABPLOO,mr,ma,viz);
zernsINTBIAS = vparSA
ABBPLOTFF=POSITION_N_PAD(newm,newn,centt,centt,ABPLOO,padnum);
writeopd(['INTBIASASPH_',num2str(1),'.opd'],ABBPLOTFF,633,1,0.001103);
fid=fopen('INTBIASASPH.xls','at');fprintf(fid,'format',zernsINTBIAS);fclose(fid);

%%%%%%%%%%
% subtract interferometric bias from each OPD measurement
PP=15;
zernsF=zeros(36,PP);
for gg=1:PP
%   bb=ceil(PP*rand);   bb=gg;
    filenamestr = ['022405ASPH_' num2str(bb) '.txt']; % measured OPD data
[xN, yN, wN] = read_fisba(filenamestr);
xmaxN = max(xN);   xminN = min(xN);   x_vectN = xminN: 1: xmaxN;
yminN = min(yN);   ymaxN = max(yN);   y_vectN = yminN: 1: ymaxN;
lenxN = length(x_vectN);   centerxN = floor((max(xN)-min(xN))/2);
lenyN = length(y_vectN);   centeryN = floor((max(yN)-min(yN))/2);
    centerN=[centerxN centeryN];
for qN=1:lenyN
    for rN=1:lenxN
        nancheck = isnan(wN(qN,rN));
        if nancheck == 0
            zsumN(qN,rN) = zsumN(qN,rN) + wN(qN,rN);
            indexN(qN,rN) = indexN(qN,rN) + 1;
        end end end
zavgN=zsumN./(index+eps);[iiN jjN]=find(~isnan(zavgN));
iminN=min(iiN); jminN=min(jjN);imaxN=max(iiN); jmaxN=max(jjN);
zavgN=zavgN(iminN:imaxN,jminN:jmaxN);[x_vectN,y_vectN]=get_xy(zavgN,1);
ZZNEW=mask_circle(wN,centerN,ar);
ZZNEWW=10^-4*POSITION_N_PAD(newm,newn,centt,centt,ZZNEW,padnum);
ZZNEWA=RMTERMSISO(muu*(1170/512)*x_vectN,muu*(1170/512)*y_vectN,ZZNE
WW,[0 0 0 0 1 1 1 1 1 1 1 1 1 1 1 1 1 1 1 1 1 1 1 1 1 1 1 1 1 1 1 1],36);
ZDATA=POSITION_N_PAD(newm,newn,centt,centt,ZZNEWA,padnum);
ZDATAA=mask_circle(ZDATA,cent_pos,ar);
ZDATAAA=POSITION_N_PAD(newm,newn,centt,centt,ZDATAA,padnum);
vsize= size(ZDATAA);

```

```

[mr,ma] = zern_radius_angle(vsize,cent_pos,ar);num_zernsN = 36;
viz = 1:1:num_zernsN;
[vparN,rmseN,sparN,tparN,pparN] = zern_estim(ZDATAA,mr,ma,viz);zernsN = vparN
ZZ=(ZDATAAA-ABBPLOTFF); % Interferometric bias is subtracted from the raw data
ZZFF=mask_circle(ZZ,cent_pos,ar);
ZFF=RMTERMSISO(muu*(1170/512)*x_vectz,uu*(1170/512)*y_vectz,ZZFF,[0 0 0 0
1 1 1 1 1 1 1 1 1 1 1 1 1 1 1 1 1 1 1 1 1 1 1 1 1 1 1 1 1 1 1 1 1 1],36);
ZZF=mask_circle(ZFF,cent_pos,ar);
%%%%%%%%%%%%%%%%%%%%%%%%%%%%%%%%%%%%%%%%%%%%%%%%%%%%%%%%%%%%%%%%%%%%%%
vsize= size(ZZF); %ZZF
[mr,ma] = zern_radius_angle(vsize,cent_pos,ar);
num_zernsF = 36;viz = 1:1:num_zernsF;
[vparF,rmseF,sparF,tparF,pparF] = zern_estim(ZZF,mr,ma,viz); zernsF(:,gg) = vparF;
ZZFINAL=POSITION_N_PAD(newm,newn,centt,centt,ZZF,padnum);
writeopd(['BIASCORDATA_',num2str(bb),'_opd'],ZZFINAL,633,1,0.001103); end
fid=fopen('FISBA_BIASCORDATA.xls','at');fprintf(fid,'format',zernsF);fclose(fid);
%%%%%%%%%%%%%%%%%%%%%%%%%%%%%%%%%%%%%%%%%%%%%%%%%%%%%%%%%%%%%%%%%%%%%%
% Zernikes from bias corrected OPD measurement data
ZDC=zernsF(:,1:PP);
A00=ZDC(1,1:PP); A11=ZDC(2,1:PP); A1m1=ZDC(3,1:PP); A20=ZDC(4,1:PP);
A22=ZDC(5,1:PP); A2m2=ZDC(6,1:PP); A31=ZDC(7,1:PP); A3m1=ZDC(8,1:PP);
A40=ZDC(9,1:PP); A33=ZDC(10,1:PP); A3m3=ZDC(11,1:PP); A42=ZDC(12,1:PP);
A4m2=ZDC(13,1:PP); A51=ZDC(14,1:PP); A5m1=ZDC(15,1:PP);
A60=ZDC(16,1:PP); A44=ZDC(17,1:PP); A4m4=ZDC(18,1:PP); A53=ZDC(19,1:PP);
A5m3=ZDC(20,1:PP); A62=ZDC(21,1:PP); A6m2=ZDC(22,1:PP);
A71=ZDC(23,1:PP); A7m1=ZDC(24,1:PP); A80=ZDC(25,1:PP); A55=ZDC(26,1:PP);
A5m5=ZDC(27,1:PP); A64=ZDC(28,1:PP); A6m4=ZDC(29,1:PP);
A73=ZDC(30,1:PP); A7m3=ZDC(31,1:PP); A82=ZDC(32,1:PP); A8m2=ZDC(33,1:PP);
A91=ZDC(34,1:PP); A9m1=ZDC(35,1:PP); A100=ZDC(36,1:PP);
% regenerate the OPD data from 36 Zernike coefficients
for jj=1:PP
getM=ceil(PP*rand); % getM=jj;
X=uu*(1170/512)*x_vectz; Y=uu*(1170/512)*y_vectz;

X2=X.*X; Y2=Y.*Y; XY=X.*Y; X3=X2.*X; Y3=Y2.*Y; XY2=X.*Y2; X2Y=X2.*Y;
r12=X2+Y2; X4=X2.*X2; Y4=Y2.*Y2; X5=X3.*X2; Y5=Y3.*Y2;
X6=X4.*X2; Y6=Y4.*Y2; X7=X5.*X2; Y7=Y5.*Y2; X8=X4.*X4; Y8=Y4.*Y4;
X9=X7.*X2; Y9=Y7.*Y2; X10=X8.*X2; Y10=Y8.*Y2; p14=r12.*r12; p16=p14.*r12;

AA1=A00(getM)*ones(512,512)+A11(getM)*X+A1m1(getM)*Y+A20(getM)*(2*X2+2
*Y2-1)+A22(getM)*(X2-Y2)+A2m2(getM)*(2*XY)+A31(getM)*(3*X3+3*XY2-
2*X)+A3m1(getM)*(3*X2Y+3*Y3-2*Y)+A40(getM)*(6*r12.*r12-
6*r12+1)+A33(getM)*(X3-3*XY2);
AA2=A3m3(getM)*(3*X2Y-Y3)+A42(getM)*(4*X2.*X2-3*X2+3*Y2-
4*Y2.*Y2)+A4m2(getM)*(8*X3.*Y+8*X.*Y3-
6*XY)+A51(getM)*(10*X3.*X2+20*X3.*Y2+10*XY.*Y3-12*X3-

```



```

A22xy=mean(A11.*A22)-mean(A11)*mean(A22);
A22xx=mean(A11.^2)-(mean(A11)).^2;
alpha221=A22xy/A22xx;%slope
alpha222=mean(A22)-alpha221*mean(A11);
N22=length(A22); U221= sqrt(dA22.^2/(N22*A22xx));
dA22=std(A22); U222= sqrt((dA22.^2*mean(A11.^2))/(N22*A22xx));

A31xy=mean(A11.*A31)-mean(A11)*mean(A31);
A31xx=mean(A11.^2)-(mean(A11)).^2;
alpha311=A31xy/A31xx; alpha312=mean(A31)-alpha311*mean(A11);
N31=length(A31); U311= sqrt(dA31.^2/(N31*A31xx));
dA31=std(A31); U312=sqrt((dA31.^2*mean(A11.^2))/(N31*A31xx));

A33xy=mean(A11.*A33)-mean(A11)*mean(A33);
A33xx=mean(A11.^2)-(mean(A11)).^2;
alpha331=A33xy/A33xx; alpha332=mean(A33)-alpha331*mean(A11);
N33=length(A33); U331= sqrt(dA33.^2/(N33*A33xx));
dA33=std(A33); U332= sqrt((dA33.^2*mean(A11.^2))/(N33*A33xx));

A42xy=mean(A11.*A42)-mean(A11)*mean(A42);
A42xx=mean(A11.^2)-(mean(A11)).^2;
alpha421=A42xy/A42xx; alpha422=mean(A42)-alpha421*mean(A11);
N42=length(A42); U421= sqrt(dA42.^2/(N42*A42xx));
dA42=std(A42); U422= sqrt((dA42.^2*mean(A11.^2))/(N42*A42xx));

A51xy=mean(A11.*A51)-mean(A11)*mean(A51);
A51xx=mean(A11.^2)-(mean(A11)).^2;
alpha511=A51xy/A51xx; alpha512=mean(A51)-alpha511*mean(A11);
N51=length(A51); U511= sqrt(dA51.^2/(N51*A51xx));
dA51=std(A51); U512= sqrt((dA51.^2*mean(A11.^2))/(N51*A51xx));

A2m2mxy=mean(A1m1.*A2m2)-mean(A1m1)*mean(A2m2);
A2m2mxx=mean(A1m1.^2)-(mean(A1m1)).^2;
alpha2m21m=A2m2mxy/A2m2mxx;
alpha2m22m=mean(A2m2)-alpha2m21m*mean(A1m1);
N2m2m=length(A2m2);U2m21m=sqrt(dA2m2m.^2/(N2m2m*A2m2mxx));
dA2m2m=std(A2m2);
U2m22m= sqrt((dA2m2m.^2*mean(A1m1.^2))/(N2m2m*A2m2mxx));

A3m1mxy=mean(A1m1.*A3m1)-mean(A1m1)*mean(A3m1);
A3m1mxx=mean(A1m1.^2)-(mean(A1m1)).^2;alpha3m11m=A3m1mxy/A3m1mxx;
alpha3m12m=mean(A3m1)-alpha3m11m*mean(A1m1);
N3m1m=length(A3m1); U3m11m=sqrt(dA3m1m.^2/(N3m1m*A3m1mxx));
dA3m1m=std(A3m1);
U3m12m=sqrt((dA3m1m.^2*mean(A1m1.^2))/(N3m1m*A3m1mxx));

A3m3mxy=mean(A1m1.*A3m3)-mean(A1m1)*mean(A3m3);

```

```

A3m3mxx=mean(A1m1.^2)-(mean(A1m1)).^2;
alpha3m31m=A3m3mxy/A3m3mxx;
alpha3m32m=mean(A3m3)-alpha3m31m*mean(A1m1);
N3m3m=length(A3m3); U3m31m= sqrt(dA3m3m.^2/(N3m3m*A3m3mxx));
dA3m3m=std(A3m3);
U3m32m= sqrt((dA3m3m.^2*mean(A1m1.^2))/(N3m3m*A3m3mxx));

A4m2mxy=mean(A1m1.*A4m2)-mean(A1m1)*mean(A4m2);
A4m2mxx=mean(A1m1.^2)-(mean(A1m1)).^2;
alpha4m21m=A4m2mxy/A4m2mxx;
alpha4m22m=mean(A4m2)-alpha4m21m*mean(A1m1);
N4m2m=length(A4m2); U4m21m= sqrt(dA4m2m.^2/(N4m2m*A4m2mxx));
dA4m2m=std(A4m2);
U4m22m= sqrt((dA4m2m.^2*mean(A1m1.^2))/(N4m2m*A4m2mxx));

A5m1mxy=mean(A1m1.*A5m1)-mean(A1m1)*mean(A5m1);
A5m1mxx=mean(A1m1.^2)-(mean(A1m1)).^2;
alpha5m11m=A5m1mxy/A5m1mxx;
alpha5m12m=mean(A5m1)-alpha5m11m*mean(A1m1);
N5m1m=length(A5m1); U5m11m= sqrt(dA5m1m.^2/(N5m1m*A5m1mxx));
dA5m1m=std(A5m1);
U5m12m= sqrt((dA5m1m.^2*mean(A1m1.^2))/(N5m1m*A5m1mxx));

A40xy=mean(A20.*A40)-mean(A20)*mean(A40);
A40xx=mean(A20.^2)-(mean(A20)).^2;
alpha401=A40xy/A40xx;
alpha402=mean(A40)-alpha401*mean(A20);
N40=length(A40); U401= sqrt(dA40.^2/(N40*A40xx)); % uncertainty in the slope
dA40=std(A40); U402= sqrt((dA40.^2*mean(A20.^2))/(N40*A40xx));

A60xy=mean(A20.*A60)-mean(A20)*mean(A60);
A60xx=mean(A20.^2)-(mean(A20)).^2;
alpha601=A60xy/A60xx;
alpha602=mean(A60)-alpha601*mean(A20);
N60=length(A60); U601= sqrt(dA60.^2/(N60*A60xx));
dA60=std(A60); U602= sqrt((dA60.^2*mean(A20.^2))/(N60*A60xx));

%%%%%%%%%%
for LL=1:ITER % number of iteration to get a distribution say 100
getRN=randn;
Newalph221=alpha221+U221*getRN;Newalph2m21m=alpha2m21m + U2m21m*getRN;
Newalph222=alpha222+U222*getRN;Newalph2m22m=alpha2m22m + U2m22m*getRN;
Newalph311=alpha311+U311*getRN;Newalph3m11m=alpha3m11m + U3m11m*getRN;
Newalph312=alpha312+U312*getRN;Newalph3m12m=alpha3m12m + U3m12m*getRN;
Newalph331=alpha331+U331*getRN;Newalph3m31m=alpha3m31m + U3m31m*getRN;
Newalph332=alpha332+U332*getRN;Newalph3m32m=alpha3m32m + U3m32m*getRN;

```

```

Newalph421=alpha421+U421*getRN;Newalph4m21m=alpha4m21m +
U4m21m*getRN;
Newalph422=alpha422+U422*getRN;Newalph4m22m=alpha4m22m + U4m22m*getRN;
Newalph511=alpha511+U511*getRN;Newalph5m11m=alpha5m11m + U5m11m*getRN;
Newalph512=alpha512+U512*getRN;Newalph5m12m=alpha5m12m + U5m12m*getRN;
Newalph401=alpha401+U401*getRN;Newalph601=alpha601+U601*getRN;
Newalph402=alpha402 + U402*getRN;Newalph602=alpha602 + U602*getRN;
NewA221=Newalph221*A11 + Newalph222; NewA2m21m=Newalph2m21m*A1m1 +
Newalph2m22m;
NewA311=Newalph311*A11 + Newalph312;NewA3m11m=Newalph3m11m*A1m1 +
Newalph3m12m;
NewA331=Newalph331*A11 + Newalph332;NewA3m31m=Newalph3m31m*A1m1 +
Newalph3m32m;
NewA421=Newalph421*A11 + Newalph422;NewA4m21m=Newalph4m21m*A1m1 +
Newalph4m22m;
NewA511=Newalph511*A11 + Newalph512;NewA5m11m=Newalph5m11m*A1m1 +
Newalph5m12m;
NewA401=Newalph401*A20+Newalph402;NewA601=Newalph601*A20+Newalph602;
getR=ceil(PP*rand);
    NewA221A=NewA221(:,getR); NewA2m21Am=NewA2m21m(:,getR);
    NewA311A=NewA311(:,getR); NewA3m11Am=NewA3m11m(:,getR);
    NewA331A=NewA331(:,getR); NewA3m31Am=NewA3m31m(:,getR);
    NewA421A=NewA421(:,getR); NewA4m21Am=NewA4m21m(:,getR);
    NewA511A=NewA511(:,getR); NewA5m11Am=NewA5m11m(:,getR);
    NewA401A=NewA401(:,getR); NewA601A=NewA601(:,getR);

x=muu*(1170/512)*x_vectz; y=muu*(1170/512)*y_vectz;
x2=x.*x; y2=y.*y; xy=x.*y; x3=x2.*x; y3=y2.*y; xy2=x.*y2; x2y=x2.*y; r2=x2+y2;
x4=x2.*x2; y4=y2.*y2; x5=x3.*x2; y5=y3.*y2;
x6=x4.*x2; y6=y4.*y2; x7=x5.*x2; y7=y5.*y2; x8=x4.*x4; y8=y4.*y4; x9=x7.*x2;
y9=y7.*y2; x10=x8.*x2; y10=y8.*y2; p4=r2.*r2; p6=p4.*r2;

ANEW1A=(NewA221A)*(x2-
y2)+(NewA2m21Am)*(2*xy)+(NewA311A)*(3*x3+3*xy2-
2*x)+(NewA3m11Am)*(3*x2y+3*y3-2*y)+NewA401A*(6*r2.*r2-
6*r2+1)+(NewA331A)*(x3-3*xy2);
ANEW1B=(NewA3m11Am)*(3*x2y-y3)+(NewA421A)*(4*x2.*x2-3*x2+3*y2-
4*y2.*y2)+(NewA4m21Am)*(8*x3.*y+8*x.*y3-
6*xy)+(NewA511A)*(10*x3.*x2+20*x3.*y2+10*xy.*y3-12*x3-
12*xy2+3*x)+(NewA5m11Am)*(10*x2y.*x2+20*x2y.*y2+10*y3.*y2-12*x2y-
12*y3+3*y)+ NewA601A*(20*p6-30*p4+12*r2-1);
    MIS_map=ANEW1A + ANEW1B;
    MIS_mapp=mask_circle(MIS_map,cent_pos,ar); % aberration map
    MIS_mapc=POSITION_N_PAD(newm,newn,centt,centt,MIS_mapp,padnum);

```


APPENDIX F: SURFACE PROFILE MEASUREMENT SIMULATION

```

% The program does the following
% request different inputs like conic constant, radius, NA, Misalignment, etc
% find the gradient of the part to set a condition for applied NA
% adds noise when necessary
% get the surface data with the conditon set
% this is the simulated measurement data using SWLI approach
% plot the surface and save it as an .opd file
padnum = nan;
k=input('conic constant of the part ='); ks=0;
r1=input('radius of curvature (um)of the part=');
dia=input('diamter (um) of the part=');
NAo=input('NA used in the measurement'); % numerical objective used
(0.3 for 10X objective)
ThetaO=asin(NAo)*180/pi; ThetaM=13.82;do=2*r1*NAo;
Mask=input('mask in % (80,etc) =');
d=(Mask/100);
ThetaX=input('rotation angle of the part about X in CCW (+ve) or inCW (-ve)');
ThetaY=input('rotation angle of the part about Y in CCW (+ve) or inCW (-ve)');
ThetaZ=input('rotation angle of the part about Z in CCW (+ve) or inCW (-ve)');
A=[-640/2:1:640/2]; B=[-480/2:1:480/2];
[x1,y1]=meshgrid(A,B);
lenx1=length(x1(1,:)); leny1=length(y1(:,1));
newm=leny1; newn=lenx1; WPS=0.01*ones(newm,newn);
x_cent=newm/2; y_cent=newn/2;
Rx=[1 0 0; 0 cos(ThetaX*pi/180) sin(ThetaX*pi/180); 0 -sin(ThetaX*pi/180)
cos(ThetaX*pi/180)];
Ry=[cos(ThetaY*pi/180) 0 -sin(ThetaY*pi/180); 0 1 0; sin(ThetaY*pi/180) 0
cos(ThetaY*pi/180)];
Rz=[cos(ThetaZ*pi/180) sin(ThetaZ*pi/180) 0; -sin(ThetaZ*pi/180)
cos(ThetaZ*pi/180) 0; 0 0 1];
R1=Rx*(Ry*Rz); R2=Rx*(Rz*Ry); R3=Ry*(Rx*Rz);
R4=Ry*(Rz*Rx); R5=Rz*(Rx*Ry); R6=Rz*(Ry*Rx);
RR=input('rotation order(RR): (R1=XYZ, R2=XZY, R3=YXZ, R4=YZX, R5=ZXY,
R6=ZYX) =');
c=1/r1; s=sqrt(x1.^2 + y1.^2);
if s < r1
    Zs=-(c*s.^2./(1+sqrt(1-(k+1)*c^2*(s.^2))))+r1; % the part (convex) surface
equation
    [ZX ZY]=GRADIENT(Zs,1,1);
    alphaX=(180/pi)*atan2(ZX,1);alphaY=(180/pi)*atan2(ZY,1);
    alMAX=ceil(max(alphaX(:))); alMIX=ceil(min(alphaX(:)))
    alMAY=ceil(max(alphaY(:))); alMIY=ceil(min(alphaY(:)))
    if max(alphaX(:)) >= ThetaM & max(alphaY(:)) >= ThetaM
    [I J]=find(tan(-ThetaO*pi/180)<= ZX <= tan(ThetaO*pi/180));
    imin=min(I);imax=max(I);jmin=min(J);jmax=max(J);

```

```

[II JJ]=find(tan(-ThetaM*pi/180)<= ZY <= tan(ThetaM*pi/180));
iimin=min(II);imax=max(II);jjmin=min(JJ);jjmax=max(JJ);
ZZSSS=Zs(iimin:imax,jjmin:jjmax); else
[I J]=find(tan(alMIX*pi/180)< ZX < tan(alMAX*pi/180));
imin=min(I);imax=max(I);jmin=min(J);jmax=max(J);
[II JJ]=find(tan(alMIY*pi/180)< ZY < tan(alMAY*pi/180));
iimin=min(II);imax=max(II);jjmin=min(JJ);jjmax=max(JJ);
ZZSSS=Zs(iimin:imax,jjmin:jjmax); end
lenxx1=imax-imin+1; lenyy1=jjmax-jjmin+1;
ZZS=POSITION_N_PAD(lenxx1,lenyy1,ceil(lenxx1/2),ceil(lenyy1/2),ZZSSS,
padnum);
newzsss=ZZS-min(ZZS(:)); newzss=newzsss./max(newzsss(:));
for ii=1:2
    if ii==1 newzs=max(newzsss(:))*newzss; end
    if ii==2
        newzs=max(newzsss(:))*imnoise(newzss,'gaussian',0,0.000002); end
    x_center = lenyy1/2;y_center = lenxx1/2;
    center_pos = [x_center y_center]; rr=220;
    [zzz_heights] = mask_circle(newzs,center_pos,rr);
    ZZZ=WPS;
    centerr_pos = [x_cent y_cent]; rr1 =(y_cent);
    [z_heights1] = mask_circle(ZZZ,centerr_pos,rr1);

z_heightss=POSITION_N_PAD(newm,newn,floor(x_cent),floor(y_cent),zzz_heights,
padnum);
figure(ii) surf(x1,y1,z_heightss); colormap hsv shading interp axis equal axis
off
writeopd(['SWLISIMU_',num2str(ii),'opd'],z_heightss,633,1,0.00103); %
1.014
end else nan; end

```

APPENDIX G: OPD MEASUREMENT SIMULATION

```

% The program does the following
% request different inputs like conic constant, radius, NA, Misalignment, etc
% find the gradient of the part to set a condition for applied NA
% adds noise when necessary
% get the surface data with the conditon set
% calculate OPD along the radius of the reference sphere direction
% plot the OPD and save it as an .opd file
padnum = nan;
k=input('conic constant of the part ='); ks=0;
r1=input('radius of curvature (um)of the part=');
dia=input('diamter (um) of the part=');
NAo=input('NA used in the measurement');
ThetaO=asin(NAo)*180/pi; ThetaM=19.87;
NAL=(dia/2)/r1; do=2*r1*NAo; dop=do/512;
Mask=input('mask in % (80,etc) =');d=(Mask/100);disp('d*dop')
ThetaX=input('rotation angle of the part about X in CCW (+ve) or inCW (-ve)');
ThetaY=input('rotation angle of the part about Y in CCW (+ve) or inCW (-ve)');
ThetaZ=input('rotation angle of the part about Z in CCW (+ve) or inCW (-ve)');
A=[-511/2:1:511/2]; B=[-511/2:1:511/2]; fa=1170/512;
[x1,y1]=meshgrid(fa*A,fa*B);lenx1=length(x1(1,:));leny1=length(y1(:,1))
newm=leny1;
newn=lenx1;WPS=0.01*ones(newm,newn);x_cent=newm/2;y_cent=newn/2;
Lx=input('translation along X or Y=');
Rx=[1 0 0; 0 cos(ThetaX*pi/180) sin(ThetaX*pi/180); 0 -sin(ThetaX*pi/180)
cos(ThetaX*pi/180)];
Ry=[cos(ThetaY*pi/180) 0 -sin(ThetaY*pi/180); 0 1 0; sin(ThetaY*pi/180) 0
cos(ThetaY*pi/180)];
Rz=[cos(ThetaZ*pi/180) sin(ThetaZ*pi/180) 0; -sin(ThetaZ*pi/180)
cos(ThetaZ*pi/180) 0; 0 0 1];
R1=Rx*(Ry*Rz); R2=Rx*(Rz*Ry); R3=Ry*(Rx*Rz);
R4=Ry*(Rz*Rx); R5=Rz*(Rx*Ry); R6=Rz*(Ry*Rx);
RR=input('rotation order(RR): (R1=XYZ, R2=XZY, R3=YXZ, R4=YZX, R5=ZXY,
R6=ZYX) =');
i=6;j=6;
for gg =6:Lx
    q=gg*1;
    c=1/r1; rz=r1+5*((q-1)-5);C=1/rz;La=0.6328;I0=1; s=sqrt(x1.^2 + y1.^2);
    dr=sqrt(r1^2 - 2*r1*5*((q-1)-5))-r1; drz=sqrt(rz^2 - 2*rz*5*((q-1)-5))-rz;
    X=(1+(dr/r1))*x1; Y=(1+(dr/r1))*y1; S=sqrt((X).^2 + (Y).^2);
    Xz=(1+(drz/rz))*x1; Yz=(1+(drz/rz))*y1; Sz=sqrt((Xz).^2 + (Yz).^2);
    if r1 <= rz & s < r1 & S < rz
        xt=X+2*((i-1)-5); yt=Y+2*((j-1)-5);
        Zss=-(c*s.^2./(1+sqrt(1-(k+1)*c^2*(s.^2))))+r1;
        xsp=RR(1,1)*xt + RR(1,2)*yt + RR(1,3)*(Zss);
        ysp=RR(2,1)*xt + RR(2,2)*yt + RR(2,3)*(Zss);
    end
end

```

```

        zsp=RR(3,1)*xt + RR(3,2)*yt + RR(3,3)*(Zss);
        sp=sqrt(xsp.^2 + ysp.^2);
        if sp < r1
Zs=-(c*sp.^2./(1+sqrt(1-(k+1)*c^2*(sp.^2))))+r1; % the part (convex) surface
equation
[ZX ZY]=GRADIENT(Zs,1,1);
alphaX=(180/pi)*atan2(ZX,1);alphaY=(180/pi)*atan2(ZY,1);
alMAX=(max(alphaX(:)));alMIX=(min(alphaX(:)));
alMAY=(max(alphaY(:)));alMIY=(min(alphaY(:)));
if max(alphaX(:)) >= ThetaM & max(alphaY(:)) >= ThetaM
[I J]=find(tan(-ThetaO*pi/180)<= ZX <= tan(ThetaO*pi/180));
imin=min(I);imax=max(I);jmin=min(J);jmax=max(J);
[II JJ]=find(tan(-ThetaM*pi/180)<= ZY <= tan(ThetaM*pi/180));
iimin=min(II);iimax=max(II);jjmin=min(JJ);jjmax=max(JJ);
ZZSSS=Zs(imin:imax,jjmin:jjmax); else
[I J]=find(tan(alMIX*pi/180)< ZX < tan(alMAX*pi/180));
imin=min(I);imax=max(I);jmin=min(J);jmax=max(J);
[II JJ]=find(tan(alMIY*pi/180)< ZY < tan(alMAY*pi/180));
iimin=min(II);iimax=max(II);jjmin=min(JJ);jjmax=max(JJ);
ZZSSS=Zs(imin:imax,jjmin:jjmax); end
lenxx1=imax-imin+1; lenyy1=jjmax-jjmin+1;
ZZS=POSITION_N_PAD(lenxx1,lenyy1,(lenxx1/2),(lenyy1/2),ZZSSS,padnum);
    ZRef=-(c*s.^2./(1+sqrt(1-(ks+1)*c^2*(s.^2))))+rz;
        xsp=RR(1,1)*xt + RR(1,2)*yt + RR(1,3)*(ZZS);
        ysp=RR(2,1)*xt + RR(2,2)*yt + RR(2,3)*(ZZS);
        zsp=RR(3,1)*xt + RR(3,2)*yt + RR(3,3)*(ZZS);
    W= -sqrt(x1.^2 + y1.^2 + ZRef.^2) + sqrt((xsp).^2 + (ysp).^2 + (zsp).^2);
newzsss=W-min(W(:));
newzss=newzsss./max(newzsss(:));
for ii=1:2
    if ii==1 newzs=max(newzsss(:))*newzss; end
    if ii==2
        newzs=max(newzsss(:))*imnoise(newzss,'gaussian',0,0.000002); end
x_center = lenyy1/2;y_center = lenxx1/2;
center_pos = [x_center y_center]; rr=110;
[zzz_heights] = mask_circle(newzs,center_pos,rr); %masking the data to a circle
Zsss=mask_circle(zsp-min(zsp(:)),center_pos,110);
ZSAAG=max(Zsss(:))-min(Zsss(:))
ZZZ=WPS;
centerr_pos = [x_cent y_cent];rr1 =(y_cent);
[z_heights1] = mask_circle(ZZZ,centerr_pos,rr1);
z_heightss=POSITION_N_PAD(newm,newn,(x_cent),(y_cent),zzz_heights,padnum);
figure(ii) surf(x1,y1,z_heightss); colormap hsv shading interp axis equal axis off
    writeopd(['SIMUOPDT_',num2str(ii),'_opd'],z_heightss,633,1,0.001103);
    end else nan; end end end

```

APPENDIX H: ZERNIKES FROM RESIDUAL ERRORS BASED ON SWLI

Zernikes	Residual surface error (Stitched)					
	Data from intended		Data from best fit		Intended from best fit	
	mean	one sigma	mean	one sigma	mean	one sigma
a00	1.75	5.86	1.4	5.75	-0.35	0.47
a11	-51.31	843.38	-52.15	843.47	-0.85	0.95
a-11	-219.06	472.85	-219.91	472.85	-0.85	0.95
a20	-86.77	52.08	-37.04	76.61	49.73	55.35
a22	14.03	100.17	14.03	100.17	0	0
a2-2	-30.26	111.03	-30.27	111.03	0	0
a31	-1.68	54.45	-1.62	54.45	0.06	0.08
a3-1	7.83	42.78	7.89	42.79	0.06	0.08
a40	-147.51	8	-149.17	8.44	-1.66	2.21
a33	2.84	56.2	2.84	56.2	0	0
a3-3	20.58	76.44	20.58	76.44	0	0
a42	-4.29	44.65	-4.29	44.65	0	0
a4-2	4.37	30.11	4.37	30.11	0	0
a51	2.51	31.72	2.51	31.72	0	0
a5-1	-7.41	31.65	-7.41	31.65	0	0
a60	14.63	6.73	14.63	6.73	0.01	0.01
a44	13.88	21.45	13.88	21.45	0	0
a4-4	2.22	31.51	2.22	31.51	0	0
a53	3.62	13.47	3.62	13.47	0	0
a5-3	-3.59	15.02	-3.59	15.02	0	0
a62	-3.61	15.53	-3.61	15.53	0	0
a6-2	-2.34	11.76	-2.34	11.76	0	0
a71	0.06	10.9	0.06	10.9	0	0
a7-1	0.4	11.78	0.4	11.78	0	0
a80	8.07	3.44	8.07	3.44	0	0
a55	7.22	25.67	7.22	25.67	0	0
a5-5	-0.86	24.39	-0.86	24.39	0	0
a64	-6.29	12.32	-6.29	12.32	0	0
a6-4	2.19	15.01	2.19	15.01	0	0
a73	-1.79	6.4	-1.79	6.4	0	0
a7-3	-2.64	7.22	-2.64	7.22	0	0
a82	2.38	9.24	2.38	9.24	0	0
a8-2	1.46	13.12	1.46	13.12	0	0
a91	-1.27	6.31	-1.27	6.31	0	0
a9-1	2.8	7.79	2.8	7.79	0	0
a100	-4.49	3.69	-4.49	3.69	0	0

Note: units are in nm

Zernikes	Residual surface error (Not Stitched)					
	Data from intended		Data from best fit		Intended from best fit	
	mean	one sigma	mean	one sigma	mean	one sigma
a00	0.8	1.66	0.57	1.65	-0.22	0.42
a11	227.42	102.81	226.88	102.56	-0.54	1.02
a-11	-146.52	95.88	-147.06	95.96	-0.54	1.02
a20	-178.25	90.85	-147.28	109.54	30.97	59.95
a22	12.2	59.31	12.2	59.31	0	0
a2-2	-5.43	68.89	-5.43	68.89	0	0
a31	25.39	210.78	25.39	210.79	0	0.09
a3-1	-37.49	178.95	-37.49	178.96	0	0.09
a40	-113.77	13.57	-113.84	13.65	-0.07	2.47
a33	-15.97	43.67	-15.97	43.67	0	0
a3-3	0.66	40.21	0.66	40.21	0	0
a42	4.77	21.81	4.77	21.81	0	0
a4-2	-0.78	19.61	-0.78	19.61	0	0
a51	-19.36	50.66	-19.36	50.66	0	0
a5-1	14.53	39.73	14.53	39.73	0	0
a60	39.56	11.91	39.56	11.91	0	0.01
a44	1.66	6.92	1.66	6.92	0	0
a4-4	0.37	10.21	0.37	10.21	0	0
a53	-1.96	20.56	-1.96	20.56	0	0
a5-3	4.02	19.32	4.02	19.32	0	0
a62	2.95	7.73	2.95	7.73	0	0
a6-2	-5.2	5.4	-5.2	5.4	0	0
a71	-9.82	7.19	-9.82	7.19	0	0
a7-1	4.89	7.62	4.89	7.62	0	0
a80	1.41	8.68	1.41	8.68	0	0
a55	-6.35	29.21	-6.35	29.21	0	0
a5-5	-4.3	26.63	-4.3	26.63	0	0
a64	1.52	3.3	1.52	3.3	0	0
a6-4	-1.12	3.49	-1.12	3.49	0	0
a73	-0.78	10.91	-0.78	10.91	0	0
a7-3	-3.78	11.57	-3.78	11.57	0	0
a82	0.14	9.05	0.14	9.05	0	0
a8-2	0.86	9.81	0.86	9.81	0	0
a91	-7.42	7.85	-7.42	7.85	0	0
a9-1	7.21	8.65	7.21	8.65	0	0
a100	19.04	4.4	19.04	4.4	0	0

APPENDIX I: ZERNIKES FROM RESIDUAL ERRORS BASED ON PSI

Zernikes	Residual surface error					
	Data from Intedded		Data from Best fit		Intended from best fit	
	mean	stdev	mean	stdev	mean	stdev
a00	36.64	7.97	22.13	11.97	-14.50	12.25
a11	6.23	1.96	3.26	2.14	-2.97	2.20
a-11	10.68	1.71	7.71	2.01	-2.97	2.20
a20	-166.13	109.28	-118.91	106.91	48.81	60.33
a22	-0.81	0.19	-0.81	0.19	0.00	0.00
a2-2	-18.71	0.40	-18.71	0.40	0.00	0.01
a31	3.36	1.03	3.34	1.54	-0.02	1.10
a3-1	-16.12	0.49	-16.14	1.23	-0.02	1.10
a40	-111.55	5.30	-111.13	30.42	0.42	30.42
a33	-10.90	0.50	-10.90	0.50	0.00	0.00
a3-3	-14.69	0.45	-14.69	0.45	0.00	0.00
a42	-1.39	0.16	-1.39	0.16	0.00	0.00
a4-2	0.18	0.20	0.18	0.20	0.00	0.00
a51	5.64	0.47	5.64	0.48	-0.01	0.02
a5-1	1.26	0.46	1.25	0.46	-0.01	0.02
a60	0.50	2.89	0.62	2.89	0.13	0.39

Note: units are in nm